TKK Dissertations 247
Espoo 2010

SLOW POSITRONS IN MATERIALS SCIENCE: PULSED POSITRON BEAM AND DEFECT STUDIES IN INDIUM NITRIDE

Doctoral Dissertation

Floris Reurings

Aalto University
School of Science and Technology
Faculty of Information and Natural Sciences
Department of Applied Physics

TKK Dissertations 247
Espoo 2010

SLOW POSITRONS IN MATERIALS SCIENCE: PULSED POSITRON BEAM AND DEFECT STUDIES IN INDIUM NITRIDE

Doctoral Dissertation

Floris Reurings

Doctoral dissertation for the degree of Doctor of Science in Technology to be presented with due permission of the Faculty of Information and Natural Sciences for public examination and debate in Auditorium G at the Aalto University School of Science and Technology (Espoo, Finland) on the 12th of November 2010 at 12 noon.

Aalto University
School of Science and Technology
Faculty of Information and Natural Sciences
Department of Applied Physics

Aalto-yliopisto
Teknillinen korkeakoulu
Informaatio- ja luonnontieteiden tiedekunta
Teknillisen fysiikan laitos

Distribution:
Aalto University
School of Science and Technology
Faculty of Information and Natural Sciences
Department of Applied Physics
P.O. Box 11100 (Otakaari 1 M)
FI - 00076 Aalto
FINLAND
URL: http://tfy.tkk.fi/
Tel. +358-9-470 23101
Fax +358-9-470 23116
E-mail: floris.reurings@tkk.fi

ISBN 978-952-60-3438-6
ISBN 978-952-60-3439-3 (PDF)
ISSN 1795-2239
ISSN 1795-4584 (PDF)
URL: http://lib.tkk.fi/Diss/2010/isbn9789526034393/

TKK-DISS-2828

Aalto-Print
Helsinki 2010

Aalto University

ABSTRACT OF DOCTORAL DISSERTATION	AALTO UNIVERSITY SCHOOL OF SCIENCE AND TECHNOLOGY P.O. BOX 11000, FI-00076 AALTO http://www.aalto.fi

Author Floris Marius Alexander Reurings

Name of the dissertation
Slow positrons in materials science: Pulsed positron beam and defect studies in indium nitride

Manuscript submitted 14.06.2010	Manuscript revised
Date of the defence 12.11.2010	
☐ Monograph	☒ Article dissertation (summary + original articles)

Faculty	Faculty of Information and Natural Sciences
Department	Department of Applied Physics
Field of research	Engineering physics, physics
Opponent(s)	Dr. Pierre Desgardin
Supervisor	Professor Martti Puska
Instructor	Docent Filip Tuomisto

Abstract

A pulsed slow-positron beam, enabling positron lifetime studies in thin semiconductor layers and near-surface regions, is presented. The positron beam is modulated with a radio-frequency beam bunching system into pulses below 200 ps full-width at half-maximum at a repetition rate of 33 MHz. A Na-22 isotope source and W moderator are used as the source for slow positrons. The beam energy is variable within the range of 2–25 keV, corresponding to typical implantation depths in the range 0.01–3 μm. The lifetime is measured digitally with a BaF_2 scintillation detector coupled to a high-speed digitiser. A unique feature is that the specimen is maintained at earth ground to facilitate sample manipulation, i.e., temperature control, biasing, etc., while the source and pulsing system are floated at high voltage.

Also in this work, vacancy defects in molecular beam epitaxy (MBE) -grown indium nitride (InN) are studied with positron annihilation techniques. In addition to effects of growth conditions, those of particle irradiation and thermal annealing are investigated. In In-polar InN grown by plasma-assisted MBE, stoichiometric conditions during growth are concluded to have little effect on indium-vacancy formation. On the other hand, buffer layer optimisation is observed to lead to a lower indium-vacancy concentration, supporting the view that structural factors dictate In-vacancy formation rather than growth thermodynamics and kinetics. In He-irradiated InN films, subsequent rapid thermal annealing is observed to have notable effects on the irradiation-induced defects. The results of slow-positron Doppler-broadening and lifetime experiments indicate that in the heat-treated films, the irradiation-induced In vacancies are restructured near the film–substrate interface, where the crystal quality is poorer due to the lattice mismatch. In the rest of the InN layer, the indium vacancies and negative-ion defects produced in the irradiation are partially removed in the annealing. The observations are possibly connected to the improved electron mobility in the annealed material.

Keywords	Positron annihilation, positron lifetime, pulsed positron beam, vacancy defects, indium nitride		
ISBN (printed)	978-952-60-3438-6	ISSN (printed)	1795-2239
ISBN (pdf)	978-952-60-3439-3	ISSN (pdf)	1795-4584
Language	English	Number of pages	122 p. + app. 36 p.
Publisher	Department of Applied Physics, Aalto University		
Print distribution	Department of Applied Physics, Aalto University		

☒ The dissertation can be read at http://lib.tkk.fi/Diss/2010/isbn9789526034393/

Aalto-yliopisto

VÄITÖSKIRJAN TIIVISTELMÄ	AALTO-YLIOPISTO TEKNILLINEN KORKEAKOULU PL 11000, 00076 AALTO http://www.aalto.fi

Tekijä Floris Marius Alexander Reurings

Väitöskirjan nimi
Hitaat positronit materiaalitieteessä: Pulssitettu positronisuihku ja defektitutkimuksia indiumnitridissä

Käsikirjoituksen päivämäärä 14.06.2010	Korjatun käsikirjoituksen päivämäärä
Väitöstilaisuuden ajankohta 12.11.2010	
☐ Monografia	☒ Yhdistelmäväitöskirja (yhteenveto + erillisartikkelit)

Tiedekunta	Informaatio- ja luonnontieteiden tiedekunta
Laitos	Teknillisen fysiikan laitos
Tutkimusala	Teknillinen fysiikka, fysiikka
Vastaväittäjä(t)	Dr. Pierre Desgardin
Työn valvoja	Professori Martti Puska
Työn ohjaaja	Dosentti Filip Tuomisto

Tiivistelmä

Väitöskirjassa esitellään nk. pulssitettu hitaiden positronien suihku, joka mahdollistaa positronin elinaikatutkimukset ohuissa puolijohdemateriaaleissa ja pintakerroksissa. Laitteen radiotaajuuksinen kimputusjärjestelmä moduloi positronisuihkun aikajakaumaa puoliarvoleveydeltään alle 200 ps:n mittaisiin pulsseihin 30 ns:n toistotiheydellä. Hitaiden positronien lähteenä laitteessa käytetään ^{22}Na-isotooppilähdettä ja siihen liitettyä wolfram-moderaattoria. Suihkun kineettinen energia on säädettävissä välillä 2–25 keV vastaten noin 0.01–3 μm:n implantaatiosyvyyksiä. Elinajan mittaus suoritetaan digitaalisesti käyttäen BaF_2-tuikeilmaisimeen liitettyä nopeaa digitoijaa. Ominaista laitteelle on lisäksi se, että tutkittava näyte on mittausten aikana maapotentiaalissa, mikä helpottaa näytteen käsittelyä, kuten lämpötilan ja bias-jännitteen säätöä. Positronilähdettä ja kimputusjärjestelmää sitä vastoin kellutetaan säädettävässä suurjännitepotentiaalissa.
Väitöskirjassa on myös tutkittu vakanssityyppisiä atomihilavirheitä epitaksiaalisesti (MBE, molecular beam epitaxy) kasvatetussa indiumnitridissä (InN) käyttäen hitaiden positronien suihkuja. Työssä on tarkasteltu erilaisten kasvatusolosuhteiden sekä hiukkassäteilytyksen ja sitä seuraavan lämpökäsittelyn vaikutuksia indium-vakanssien muodostumiseen. Kasvatustekijöillä kuten stoikiometrialla havaitaan olevan vähäinen vaikutus In-vakanssien muodostumiseen plasma-avusteisella MBE-menetelmällä kasvatetussa indiumnitridissä. Sen sijaan kasvatuksessa käytettävän puskurikerroksen optimoinnin huomataan olevan yhteydessä pienempään vakanssikonsentraatioon. Toisin kuin galliumnitridissä (GaN), InN:ssä kiderakenteen laatu vaikuttaa olevan merkittävämpi tekijä indiumvakanssien muodostumisessa kuin materiaalin kasvatustekijät. Helium-säteilytetyissä InN-näytteissä havaitaan lämpötoivutuksen johtavan säteilytyksessä syntyneiden pistevirheiden uudelleenjärjestäytymiseen. Positroniannihilaation Doppler-levenemä- ja elinaikamittausten perusteella indiumvakanssit (Al_2O_3-)kasvatusalustan rajapinnan läheisyydessä, missä kidelaatu on hilavakiopoikkeamasta johtuen huonompi, muodostavat lämpökäsittelyn seurauksena uusia defektikomplekseja. Muualla InN-kerroksessa osan säteilytyksessä syntyneiden indiumvakanssien sekä negatiivisten ionien nähdään sen sijaan poistuvan lämpökäsittelyssä. Ilmiöillä saattaa olla yhteys toivutettujen näytteiden parantuneeseen elektroniliikkuvuuteen.

Asiasanat Positronin annihilaatio, positronin elinaika, pulssitettu positronisuihku, vakanssidefektit, indiumnitridi

ISBN (painettu)	978-952-60-3438-6	ISSN (painettu)	1795-2239
ISBN (pdf)	978-952-60-3439-3	ISSN (pdf)	1795-4584
Kieli	Englanti	Sivumäärä	122 s. + liit. 36 s.

Julkaisija Teknillisen fysiikan laitos, Aalto-yliopisto

Painetun väitöskirjan jakelu Teknillisen fysiikan laitos, Aalto-yliopisto

☒ Luettavissa verkossa osoitteessa http://lib.tkk.fi/Diss/2010/isbn9789526034393/

Preface

The work presented in this thesis was performed at the Department of Applied Physics, Aalto University (formerly Helsinki University of Technology) during the years 2005-2010. The National Graduate School in Materials Physics, the Finnish Academy of Science and Letters, and the Finnish Society of Sciences and Letters are gratefully acknowledged for funding. The expertise generously shared by the developers of the Pulsed Low-Energy Positron System at Institut für Angewandte Physik und Messtechnik, Universität der Bundeswehr München, Germany, is greatly appreciated.

I would like to express my gratitude to Prof. Martti Puska and Prof. Emer. Pekka Hautojärvi for providing me with the opportunity and a pleasant atmosphere to conduct my work. I would also like to thank them for all the helpful discussions. To my instructor, Doc. Filip Tuomisto, I am very grateful for all his help and support.

The construction of the pulsed positron beam has been a unique experience which I have had the honour of sharing with my colleagues D.Sc. Antti Laakso, D.Sc. Antti Pelli, and M.Sc. Esa Korhonen. The success owes invaluably to the efforts and expertise from their part. I thank them also simply for the good times we shared. Over the years, a number of people have contributed to the development of the beam, most notably M.Sc. Kim Fallström, to whom many of the original concepts of the beam owe. Their contribution is sincerely acknowledged. Personally, I would like to acknowledge M.Sc. Janne Antson and Mr. Sami Kivistö for their assistance.

D.Sc. Klaus Rytsölä I would like to thank for his tireless help and for the countless pleasant discussions we had. I also thank both present and former members of the positron and surface science research groups, and the people of the department for all the help and fun.

Finally, sadly three people, all of whom played a crucial role in making my work possible in the first place, passed away during the making. These people are, in no particular order of relevance: The late Prof. Kimmo Saarinen, Laboratory Technician Heikki Vaalte, and my mother. Hoping they have found peace, I express my sincerest honour and appreciation for their help.

Espoo, November 2010

Floris Reurings

Contents

List of Publications

This thesis consists of an overview and of the following publications which are referred to in the text by their Roman numerals.

I F. Reurings, A. Laakso, K. Rytsölä, A. Pelli, and K. Saarinen. Compact positron beam for measurement of transmission moderator efficiencies and positron yields of encapsulated sources. *Applied Surface Science*, 252(9):3154–3158, 2006.

II F. Reurings and A. Laakso. Analysis of the time resolution of a pulsed positron beam. *physica status solidi (c)*, 4(10):3965–3968, 2007.

III F. Reurings, F. Tuomisto, G. Koblmüller, C. S. Gallinat, and J. S. Speck. Vacancy defects probed with positron annihilation spectroscopy in In-polar InN grown by plasma-assisted molecular beam epitaxy: Effects of growth conditions. *physica status solidi (c)*, 6(0):S401–S404, 2009.

IV F. Reurings, F. Tuomisto, C. S. Gallinat, G. Koblmüller, and J. S. Speck. In vacancies in InN grown by plasma-assisted molecular beam epitaxy. arXiv:1010.0571v1 [cond-mat.mtrl-sci], 2010.

V F. Reurings, F. Tuomisto, W. Egger, B. Löwe, L. Ravelli, S. Sojak, Z. Liliental-Weber, R. E. Jones, K. M. Yu, W. Walukiewicz, and W. J. Schaff. Irradiation-induced defects in InN and GaN studied with positron annihilation. *physica status solidi (a)*, 207(5):1087–1090, 2010.

VI F. Reurings, C. Rauch, F. Tuomisto, R. E. Jones, K. M. Yu, W. Walukiewicz, and W. J. Schaff. Defect redistribution in postirradiation rapid-thermal-annealed InN. *Physical Review B*, 82(15):153202–4, 2010.

Author's contribution

The author has had an active role in all the phases of the work reported in this thesis. The author has performed the work involving the positron annihilation experiments and participated in the interpretation of the results reported in Publs. I–VI. He has written Publs. I, II, V, and VI, and co-written Publ. IV.

The author has also been responsible for the design, construction, and development of a pulsed positron beam, reported in this thesis, during the years 2005–2010. The work has been largely collaborative, however, with the author having been actively involved in all stages. These include mechanical, electrical, and vacuum design and construction, radio frequency, high voltage, and control system development, lifetime signal detection and processing, testing, and data analysis.

Part of the beam was complete prior to the author's involvement. A majority of the beam transport and pulsing system were already complete, and part of the mechanical structures and vacuum system had been assembled. Also, some of the electronics and high-voltage system had been developed before the author's involvement. An overview of the status of the beam at the time that the author began the work can be found in Ref. [1].

List of Abbreviations

AC	alternating current
ACAR	angular correlation of annihilation radiation
ADM	amphoteric defect model
AMOC	age–momentum correlation
DC	direct current
ECL	emitter-coupled logic
EMI	electromagnetic interference
FWHM	full width at half maximum
HV	high voltage
LEPD	low-energy positron diffraction
MBE	molecular beam epitaxy
MCP	micro-channel plate
MOCVD	metal-organic chemical vapour deposition
NIM	nuclear instrumentation module
NEPOMUC	Neutron Induced Positron Source Munich
PAES	positron Auger-electron spectroscopy
PAMBE	plasma-assisted molecular beam epitaxy
PC	personal computer
PCI	peripheral component interconnect
PLEPS	Pulsed Low-Energy Positron System
PMT	photomultiplier tube
POM	polyoxymethylene
RF	radio frequency
RTA	rapid thermal annealing
UPS	uninterruptable power supply

List of Symbols

A	second harmonic bunching amplitude
C	normalisation constant
c	speed of light
c_D	defect concentration
D	positron diffusion coefficient
E	electric field strength, energy
$\mathbf{E}$	electric field strength vector
E_F	Fermi energy
E_FS	Fermi stabilisation energy
E_0	unmodulated beam energy
E_γ	gamma photon energy
ΔE	energy spread
ΔE_γ	Doppler broadening of gamma photon energy
e	elementary charge
e^+	positron
e^-	electron
f	frequency
f_d	detector time-response/time-resolution function
f_r	instrument time-resolution function
I	lifetime-component intensity
J	positron flux density
L	positron diffusion length, length
m_e	electron mass
N	total positron number
n_B	free-positron number
n_D	defect-trapped positron number
n_Ps	positronium number
n_S	surface-positron number
n_-	electron density
o-Ps	orthopositronium
Ps	positronium
p	positron implantation profile (density function), bunching efficiency
$\mathbf{p}$	momentum vector
p_z	transversal momentum
p-Ps	parapositronium
$\mathbf{r}$	space vector
r_0	classical electron radius
S	positron source term, Doppler-broadening low-momentum parameter
S_B	bulk Doppler-broadening low-momentum parameter
S_D	defect Doppler-broadening low-momentum parameter
T	particle arrival time
ΔT	beam-bunch time-width

t, t'	time
Δt	initial beam time-width
U	modulation potential
U_0	modulation amplitude
u, u_B	free-positron density
u_D	defect-trapped positron density
V	atomic vacancy, volume
v	speed
v_0	unmodulated beam speed
W	Doppler-broadening high-momentum parameter
W_B	bulk Doppler-broadening high-momentum parameter
W_D	defect Doppler-broadening high-momentum parameter
z_0	mean implantation depth
γ	gamma photon
γ	electron-density enhancement factor
δ	positron detrapping rate
η	weighting factor
κ	positron trapping rate
λ	positron annihilation rate
λ_B	bulk positron-annihilation rate
λ_D	defect positron-annihilation rate
λ_{Ps}	positronium annihilation rate
λ_S	surface-positron annihilation rate
μ	positron mobility
μ_{c}	chopper phase-mismatch
μ_D	positron trapping coefficient
ν	total positron surface-transition rate
ν_{Ps}	surface-positronium transition rate
ν_S	positron surface-trap transition rate
ρ	momentum density, specific mass
σ_{c}	chopper acceptance time spread (standard deviation)
σ_{d}	detector resolution function standard deviation
τ	positron lifetime, lifetime component, time of flight
τ_0	ideally bunched beam arrival time
τ_{ave}	average/mean positron lifetime
τ_{Si}	positron lifetime in silicon lattice
$\Delta\tau_{\mathrm{c}}$	chromatic bunching aberration
$\Delta\tau_{\mathrm{s}}$	spherical bunching aberration
φ	main-buncher phase-mismatch
ϕ	irradiation fluence
χ	bunching parameter
χ_1	prebuncher bunching parameter
χ_2	main-buncher bunching parameter
ψ_+	positron wave-function
ψ_-	electron wave-function
ω	angular frequency

ω_1	prebuncher angular frequency
ω_2	main-buncher angular frequency

List of Figures

List of Tables

1 Introduction

Atomic defects in semiconductors often play an important role in the electrical and optical properties of the material. Intrinsic point defects such as atomic vacancies exist naturally in the lattice, although equilibrium concentrations are low at room temperature. However, defects can be introduced through different mechanisms during the growth and processing of the material. Vacancy defects can be produced, e.g., in particle irradiation or ion implantation. Like other point defects, vacancies and their complexes can affect electrical properties by introducing electronic levels in the forbidden energy gap. They can also limit electrical performance by acting as electrically passivating compensation centres or as electron scattering centres. Regarding optical properties, vacancy-type defects can often have optical emission and absorption states.

Positrons provide a unique tool for non-destructive solid-state materials characterisation, and have been used in a number of different experimental techniques for studying both bulk materials and thin layers and surfaces (see, e.g., Refs. [2–10] for introductions). Positrons implanted in a solid live shortly in thermal equilibrium in the atomic lattice before annihilation with one of the electrons. Information on the annihilation site is then carried by the gamma photons emitted in the reaction. During its lifetime and diffusion through the lattice, the positron can probe up to 10^6 lattice sites. Since especially atomic vacancies and other open-volume defects often act as effective "traps" for positrons, these can be detected and identified with a sensitivity often unmatched by other experimental techniques. The method is furthermore strongly supported by theory, adding to its power in defect studies. By varying sample temperature or illumination, one can also study vacancy charge states, optical transitions, and thermal stability.

Perhaps the most common technique in the family of positron annihilation is lifetime spectroscopy, where one can observe and identify different annihilation states from the positron lifetime distribution, or spectrum. The annihilation rate is characteristic for each positron state in the lattice. Trapped states in vacancies generally have longer lifetimes due to the reduced local electron density. Lifetime spectroscopy hence gives information on the open volume and concentrations of vacancies. Typical positron lifetimes in crystalline solids are in the range of 100–500 ps.

Another common technique in atomic defect studies uses the Doppler broadening of the 511 keV annihilation line due to the momentum of the positron–electron (e^+e^-) pair. The electron momentum states are reflected in the energy line-shape, allowing one to distinguish between the chemical surroundings of different trapping defects, e.g., decorations. Vacancy concentrations can also be estimated to some extent from the Doppler broadening. Especially together the lifetime and Doppler-broadening techniques are a powerful combination in vacancy studies.

High-energy positrons from β^+ decay or other nuclear reactions penetrate deep into the bulk of the sample, and therefore cannot be used as such when studying thin material layers, such as epitaxial films, or surfaces. To overcome this, slow-positron beams are used to produce monoenergetic low-energy positrons [4, 9, 11–15]. Since the positron affinity, or work function, can be negative for many common materials, high-energy positrons can be moderated to a beam within the eV-range by simple means [16]—the fast positrons are implanted in the moderator material, where they can achieve thermal equilibrium with the lattice and then be re-emitted from the surface with a kinetic energy roughly equal to the work function. However, only a small fraction, typically of the order of 10^{-4}, of the initial fast positrons can be converted. Depending on the moderator geometry, most of the positrons are either annihilated inside the moderator or manage to escape the moderator before slowing down. Hence, in slow-positron beams, much stronger β^+ sources are required than in bulk studies using fast positrons.

Regarding lifetime spectroscopy, the drawback of the moderation process and the necessary transport stages in slow-positron beams is that the "birth" time (more strictly, the moment of implantation in the target sample) information is lost. However, several approaches to overcome this have been presented [17–33]. To date, the most prominent method has been established by the radio-frequency (RF) velocity-modulation of an initially direct-current (DC) beam of slow (~0.1–1 keV) positrons. These so-called pulsed beams can achieve characteristic time resolutions down to ca. 250 ps in full-width at half-maximum (FWHM), comparing well with conventional (fast positron) lifetime spectrometers [34–38].

Nevertheless, regarding the application of positron lifetime spectroscopy to metals and semiconductor materials, nearly three decades since the introduction of the first pulsed positron beam, the scientific community is still—in view of existing facilities—somewhat restricted to the study of bulk materials only. The evident complexity and budget of suitable lifetime beams are unfortunately often beyond the capacity of the typical (e.g., university) research unit. Indeed, worldwide there exist today only two slow-positron lifetime beams that can achieve sufficient time resolutions for applications in semiconductor materials research, one in Germany [36] and the other in Japan [38]. In this work, a new laboratory-scale pulsed slow-positron lifetime system, intended especially for studies in thin epitaxial semiconductor layers, is presented (Chap. 3) [1, 39–41]. The technical design is discussed and the performance characteristics of the instrument are demonstrated.

Also in this work, slow-positron Doppler-broadening and lifetime spectroscopy have been applied in the investigation of point defects in indium nitride (InN) layers grown by molecular beam epitaxy (MBE) (Chap. 4). InN is under increasing investigation due to its potential in optoelectronics, telecommunication, high-speed and high-power electronics, and multi-junction solar cells [42–61]. Here, vacancy defects in different InN films are studied. In particular, effects of different growth factors and particle irradiation on the formation of In vacancies are investigated.

Results of this work show that indium vacancy (V_{In}) formation in plasma-assisted MBE-grown wurtzite InN with In surface-polarity is quite insensitive to growth temperature and stoichiometric conditions (Publs. III & IV). On the other hand, GaN buffer layer optimisation appears to lead to smaller V_{In} concentrations in In-polar material, supporting the view that structural properties play a more important role in V_{In} formation than growth kinetics and thermodynamics. In N-polar films, the smallest V_{In} concentrations are recorded in samples grown under stoichiometric conditions.

In He-irradiated MBE-grown InN, rapid thermal annealing is found to have notable effects on the irradiation-induced defects (Publs. V and VI). Near the film–substrate (Al_2O_3) interface, where structural imperfections such as extended defects are present due to the lattice mismatch, In vacancies are reorganised during the heat treatment. Elsewhere in the layer, a partial recovery of the V_{In} and negative-ion type defects is seen. These effects are possibly in connection with the improved electron mobility in the annealed films.

The overview is divided as follows. In Chap. 2, an introduction to the positron annihilation techniques is given. The pulsed positron beam, with emphasis on the author's contribution, is presented in Chap. 3. The studies in InN are discussed in Chap. 4, followed by a short summary of this thesis in Chap. 5.

2 Positron annihilation in atomic vacancy-defect studies

This chapter is based on Refs. [4, 6, 8, 10, 62, 63] and references therein. In this chapter, the two most common defect characterisation techniques within the field of positron annihilation, namely the Doppler broadening technique and positron lifetime spectroscopy, are introduced. Both techniques are based on the localisation of positrons at atomic lattice defects and detecting the resulting e^+e^- annihilation gamma photons. They are briefly illustrated in Figure 1.

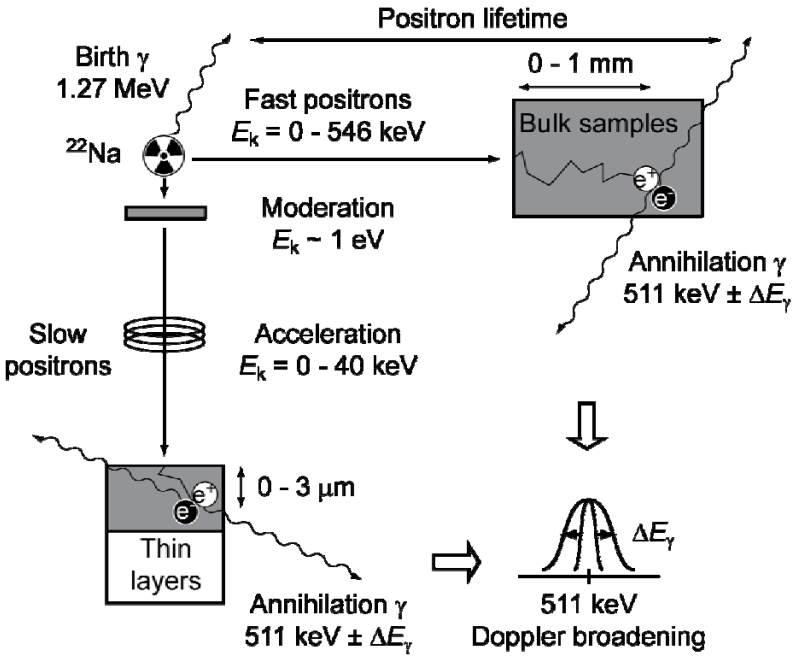

Figure 1. Simple illustration of the positron lifetime and Doppler broadening techniques. Based on Ref. [40].

Positrons implanted in a sample act as probes for open-volume atomic defects, such as atomic vacancies, because of the missing ion core repulsion at the defect site. Such defects are effective at trapping thermal positrons, diffusing through the atomic lattice as free charge carriers, into localised bound states. The vacancy detection range in semiconductor materials is roughly 10^{15}–10^{19} cm^{-3}, which coincides with typical carrier concentration ranges. Under varying temperature and illumination, charge states, thermal stability, and optical activity of vacancies can also be studied.

The techniques are strongly supported by theory, since the positron states in the lattice can be calculated from first principles (see, e.g., Ref. [63]). Positron annihilation is especially powerful in complementing other experimental techniques, such as

photoluminescence, electron paramagnetic resonance, etc. In the following, the theoretical basis is shortly described.

2.1 Positrons in solids

Positrons can be implanted into bulk samples directly from β^+-active isotope sources. The kinetic energy is quickly lost to the host lattice through ionisations and core electron excitations [64]. In the eV range, energy loss occurs mainly via electron–hole excitations and phonon emission, until the positron reaches thermal energy [64]. For positrons in the MeV range, the thermalisation time after impact on the surface is only a few ps [65, 66]. It then behaves as a free charge carrier in a delocalised state. In the following, it is assumed that only a single positron is present in the lattice, thereby omitting positron–positron interactions and excited states.

The thermal positrons behave as free charge carriers and can be described by diffusion theory, presented below [63]. The positron diffusion length is

$$L = \left(6D\tau\right)^{1/2}, \tag{1}$$

where D denotes the positron diffusion constant and τ the lifetime in the lattice. Typical diffusion lengths are of the order of 100 nm, which corresponds to a few hundred atomic layers [67–70]. Trapping centres such as neutral or negatively charged vacancy defects have deep bound positronic states, and hence act as efficient "drains" for the diffusive positron, decreasing the diffusion length and affecting the lifetime [63, 71]. Eventually, annihilation takes place with one of the electrons. The annihilation rate, or inverse positron lifetime, is related to the e^+ and e^- densities by [63, 72–75]

$$\lambda = \tau^{-1} = \pi r_0^2 c \int \left|\psi_+(\mathbf{r})\right|^2 n_-(\mathbf{r}) \gamma\left[n_-(\mathbf{r})\right] \mathrm{d}\,\mathbf{r}, \tag{2}$$

where r_0 is the classical electron radius, c the speed of light, and γ, a functional of the electron density, is an enhancement factor of the electron density at the positron. The positron lifetime is thus a direct measure of open volume. The typical lifetime in the free lattice state is in the range of 100–200 ps.

Annihilation takes place mostly through the 2γ branch, resulting in the emission of two $m_e c^2$ = 511 keV photons in (nearly) opposite directions [76]. Due to momentum conservation, the momentum of the e^+e^- pair is carried by the annihilation photons, causing a deviation in the emission angles of the photons and the broadening of the 511 keV line. This is used in the Doppler broadening technique to investigate essentially the

electron momentum states at the annihilation site, which can be used in, for example, identifying the sublattice and chemical surroundings of vacancy defects. The momentum distribution depends on the total e^+e^- overlap in the form [63]

$$\rho(\mathbf{p}) = \frac{\pi r_0 c}{V} \sum_i \left| \int_V \mathrm{d}\mathbf{r} \exp(-i\mathbf{p}\cdot\mathbf{r}) \psi_+(\mathbf{r}) \psi_{-,i}(\mathbf{r}) \sqrt{\gamma_i(\mathbf{r})} \right|^2 . \tag{3}$$

2.1.1 Diffusion, trapping, and kinetics

The thermal free positron density $u_B(\mathbf{r},t)$ in the lattice can be statistically modelled with diffusion theory [63, 77]. In the presence of an electric field $\mathbf{E}(\mathbf{r})$, the positron diffusion equation, or diffusion–annihilation equation, reads

$$\frac{\partial}{\partial t} u_B(\mathbf{r},t) = \nabla \cdot \left(D(\mathbf{r}) \nabla u_B(\mathbf{r},t) - \mu(\mathbf{r}) \mathbf{E}(\mathbf{r}) u_B(\mathbf{r},t) \right) - \lambda u_B(\mathbf{r},t) + S(\mathbf{r},t). \tag{4}$$

Here, μ is the positron mobility, λ the annihilation rate, and S the positron source term. In the presence of trapping defects, the decay rate λ is

$$\lambda = \lambda_B + \sum_{i=1}^{N} \kappa_i , \tag{5}$$

where λ_B is the annihilation rate in the delocalised (free) state, and κ_i are the transition, i.e., trapping rates to defects $i = 1, \ldots, N$. In the conventional trapping model [78, 79], the trapping rates depend on the defect concentrations c_D as $\kappa = \mu_D c_D$, and the coefficient μ_D is called the trapping coefficient (discussed below). The source term contains the contribution from the thermal escape from defects, termed detrapping, and depends on the trapped positron densities as [80, 81]

$$S(\mathbf{r},t) = \sum_{i=1}^{N} \delta_i u_{D_i}(\mathbf{r},t). \tag{6}$$

Here, δ_i is the detrapping/escape rate from defect i. It should be noted that the source term does not describe the external positron source; instead, the implantation of the positrons in the sample is taken into account in the initial conditions of Eq. (4), as will be clarified below.

Equation (4) is of the Fokker–Planck type, to which analytical solutions are known only in some special cases. In *bulk* studies, one usually assumes spatial homogeneousness and considers the lattice infinite. If no electric field is present, the drift term vanishes and Eq. (4) can be integrated over space. Denoting the free and trapped positron state populations respectively as

$$\begin{aligned} n_B(t) &= \int u_B(\mathbf{r},t)\,\mathrm{d}\,\mathbf{r}, \\ n_i(t) &= \int u_i(\mathbf{r},t)\,\mathrm{d}\,\mathbf{r}, \end{aligned} \tag{7}$$

one arrives at the conventional kinetic equations (see, e.g., Ref. [62])

$$\begin{aligned} \frac{\mathrm{d}\,n_B}{\mathrm{d}\,t} &= -\left(\lambda_B + \sum_{i=1}^{N}\kappa_i\right)n_B + \sum_{i=1}^{N}\delta_i n_i, \\ \frac{\mathrm{d}\,n_i}{\mathrm{d}\,t} &= \kappa_i n_B - \left(\lambda_{D_i} + \delta_i\right)n_i, \quad i = 1,\ldots,N \end{aligned} \tag{8}$$

with initial conditions $n_B(0) = 1$ and $n_i(0) = 0$. Solving Eq. (8) yields for the total positron number the form [62]

$$N(t) \equiv n_B(t) + \sum_{i=1}^{N} n_i(t) = \sum_{j=1}^{N+1} I_j \exp\left(-\lambda_j t\right). \tag{9}$$

Hence, the positron lifetime spectrum, $-\frac{\mathrm{d}}{\mathrm{d}t}N(t) = \sum I_j\lambda_j \exp\left(-\lambda_j t\right)$, is a superposition of exponential decay rates. One speaks of lifetime components $\tau_j = \lambda_j^{-1}$, and the weights I_j are called lifetime-component intensities. For instance in the simplest case, in the presence of a single trapping defect with no detrapping, Eqs. (8) & (9) give the following relations (τ_{ave} denotes the average/mean positron lifetime, corresponding to the centre-of-mass of the lifetime spectrum) [62]:

$$
\begin{aligned}
&\lambda_B = I_1\lambda_1 + I_2\lambda_2,\\
&\tau_{\text{ave}} \equiv I_1\tau_1 + I_2\tau_2 = \frac{1+\kappa\tau_D}{1+\kappa\tau_B}\tau_B,\\
&\tau_1 = \frac{\tau_D - \tau_{\text{ave}}}{\tau_D - \tau_B}\tau_B, \quad \lambda_1 = \frac{\lambda_B - I_2\lambda_D}{I_1},\\
&I_2 = \frac{\tau_{\text{ave}} - \tau_1}{\tau_2 - \tau_1},\\
&\kappa = \frac{I_2}{I_1}\left(\lambda_B - \lambda_D\right) = I_2\left(\lambda_1 - \lambda_D\right) = \frac{1}{\tau_B}\frac{\tau_{\text{ave}} - \tau_B}{\tau_D - \tau_{\text{ave}}}.
\end{aligned}
\tag{10}
$$

The trapping coefficient μ_D depends on the type of defect and its charge state, and the temperature (see Ref. [71]). In semiconductors, neutral and negative vacancies usually have room-temperature trapping coefficients in the range 10^{14}–10^{16} s^{-1}at., and can thus be detected at concentrations above 10^{15}–10^{16} cm^{-3}. The dominant energy release mechanisms in trapping are electronic excitations and phonon emission. For positively charged vacancies, the trapping coefficient is much lower (~10^{10} s^{-1}at.) due to the Coulomb repulsion, and they therefore cannot be observed at room temperature. For neutral vacancies, the square-well-potential model leads to a temperature-independent trapping coefficient. The charge of the vacancy, however, modelled with an additional long-range Coulomb potential superimposed on the square-well potential, induces a temperature-dependence in the trapping coefficient. The attractive Coulomb potential of the negatively charged vacancy introduces shallow positron Rydberg states that provide a fast two-stage trapping mechanism in addition to direct trapping to the ground state. For negative vacancies, the coefficient increases with decreasing temperature due to the increased Coulomb-wave amplitude of the positron at the vacancy. At room-temperature, the trapping coefficient is about an order of magnitude larger than for the neutral vacancy. The positron ground state in vacancies is deep, ~1 eV, so that thermal detrapping from vacancies rarely occurs at room temperature. Other point defects, such as negatively charged interstitials, can also have Rydberg states, and are termed negative ions. These have smaller binding energies of 10–100 meV, and are therefore also referred to as shallow traps. Detrapping from shallow traps occurs already at room temperature, but they can compete with vacancies at positron trapping at low temperatures, ca. below 100 K. [8, 10, 62, 71]

2.1.2 Surface processes

As in the case of electrons, positron backscattering can occur at impact with a surface, especially for high-energy positrons [82–84]. The elastic scattering cross sections from nuclei are generally smaller for the positron than for the electron. Also, the backscattering angle distribution is narrower. The backscattering probability increases

with atomic number, and can reach tens of % in the 10 keV range. Secondary electron emission is also generated in the impact [85].

Low-energy incident positrons can get directly trapped at the surface in their own image potential [63]. Some materials, on the other hand, possess a negative positronic work function, in which case a positron can be spontaneously emitted from the surface [16]. This can of course also occur to positrons returning to the surface from inside the lattice after implantation, which is utilised extensively in fast-to-slow positron moderation [86], as discussed in Sec. 2.4.1. Another surface phenomenon to be mentioned is positron diffraction, which is used, analogously with electrons, in low-energy positron diffraction (LEPD) [85].

At the surface, the positron can also bind with an electron into the e^+–e^- bound state, positronium (Ps, ionisation energy 6.8 eV), and the Ps atom can then escape from the surface [11, 87]. Ps has two ground states, the singlet state with antiparallel spins (parapositronium, *p*-Ps) and the triplet state with parallel spins (orthopositronium, *o*-Ps), with lifetimes in vacuum of 125 ps and 142 ns, respectively. Ps can form also inside insulating or porous materials, but has not been observed to occur in the lattice in metals or semiconductors. Conservation laws dictate that the intrinsic annihilation of *p*-Ps results in 2γ emission, while *o*-Ps decays through the 3γ branch. Due to the long lifetime of *o*-Ps, an important related surface process is so-called pickoff annihilation, where the positron in the *o*-Ps atom is instead annihilated (through 2γ emission) with another nearby electron with opposing spin. [8]

2.2 Positron lifetime spectroscopy

The conventional experimental setup for determining the positron lifetime in bulk samples consists of a small amount (~1 MBq/30 μCi) of ^{22}NaCl pressed between two pieces of the sample material, and surrounded by two fast scintillation detectors with associated signal processing units (see, e.g., Refs. [88, 89]). Along with other benefits, ^{22}Na is a convenient β^+ emitter because it provides a birth signal for the positron through the 1.275 keV de-excitation of the daughter ^{22}Ne nucleus, by photon emission practically simultaneously (3.7 ps decay time) with the positron. The positron lifetime in the sample can therefore be determined from the detection time delay between the birth and annihilation photons. The scintillation detectors are coupled to either a chain of analogue nuclear timing electronics followed by a multichannel board, or, more recently, to a high-speed digitiser commanded via a personal computer (PC) workstation [90–94].

In practice, usually a total of a few million events need to be collected per spectrum for sufficient statistics. According to Eq. (9), the spectrum is a weighted superposition of exponential decay rates, with a fixed offset from the cable delays and electronics. The

typical time response, or resolution function, of the experimental setup is around 200–250 ps FWHM, depending heavily on the size of the scintillators [89]. Since this is comparable to typical positron lifetimes, the resolution function needs to be taken into account in the decomposition of the experimental histogram. To facilitate the data analysis, the setup is fine tuned so that the resolution function resembles a Gaussian function as closely as possible. The experimental histogram is then a convolution of the positron lifetime distribution and a Gaussian distribution, and the lifetime components are extracted from the data by seeking the best fit to the data [8]. Figure 2 shows an example of an experimental lifetime spectrum. Despite the limited resolution, lifetimes of the order of 100 ps and longer can be determined. Within practical data collection times, the statistics allow for reliably extracting usually at most three lifetime components from the histogram [10, 62]. A so-called source correction is needed to filter out the contribution from annihilations that take place in the source packet instead of in the sample. Even in cases where the decomposition cannot be performed, the average lifetime, $\tau_{\text{ave}} = \sum_j I_j \tau_j$, is a statistically relatively reliable measure of open volume, and can be determined with an accuracy of less than 1 ps. The positron lifetime is most sensitive to the open volume for vacancies of up to a few missing atoms.

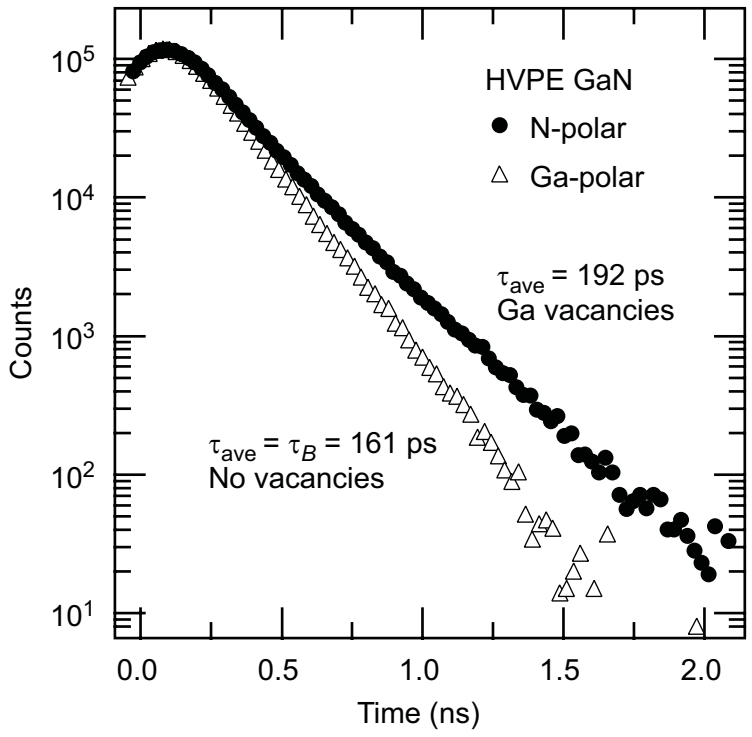

Figure 2. Example of experimental positron lifetime spectra in GaN grown by hydride vapour-phase epitaxy. No vacancy-trapping is observed in the Ga-polar material, while in the N-polar layer, the average lifetime is longer due to the presence of Ga vacancies. The finite resolution of the experimental setup can be seen in the rising edge of the spectrum. Based on Ref. [95].

2.3 Doppler broadening technique

In the laboratory frame, the transversal momentum p_z of the e^+e^- pair causes a Doppler shift in the energy of the annihilation photons. The positron momentum is small in the ground state, so the major contribution is from the electron. The shift is given by

$$\Delta E_\gamma \approx \frac{1}{2} p_z c. \tag{11}$$

The transversal electron momentum distribution at the annihilation site can therefore be measured with energy-sensitive detectors. The high-momentum region is dominated by the core electrons of the surrounding atoms, which enables the identification of the chemical surroundings of atomic vacancies. [10]

Electronically stabilised high-purity Ge detectors, with typical energy resolutions around 1.5 keV FWHM (at 511 keV), are used [8]. Since the resolution is comparable to the typical linewidth of 2–3 keV, the lineshape is often parameterised by ascribing energy windows corresponding to the low- and high-momentum regions, termed *S* and *W* parameters, respectively (see Figure 3 for an illustration) [10]. Typical windows are $|p_z| \leq 0.4$ a.u. ($|E_\gamma - 511\text{ keV}| \leq 0.75$ keV) for *S*, and $1.6\text{ a.u.} \leq |p_z| \leq 2.4$ a.u. ($2.9\text{ keV} \leq |E_\gamma - 511\text{ keV}| \leq 4.4$ keV) for *W*.

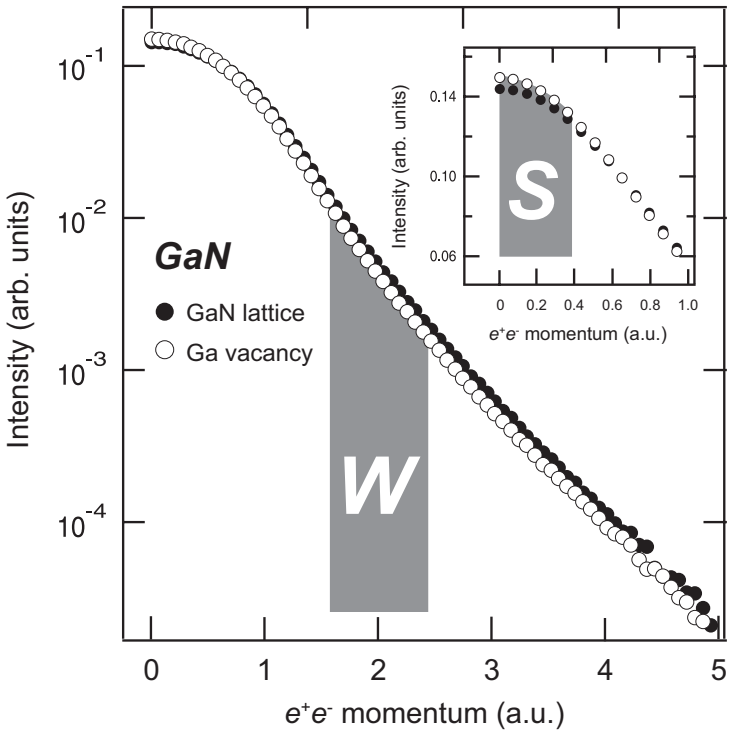

Figure 3. Doppler-broadening lineshape parameters S and W. a.u. stands for atomic units. Based on Ref. [40].

Again following from the trapping model, the lineshape is a superposition of different annihilation states i, weighted by their intensities [10]:

$$S = \sum_i \eta_i S_i, \quad W = \sum_i \eta_i W_i, \quad \sum_i \eta_i = 1. \tag{12}$$

The electrons surrounding vacancies generally have lower momentum states, which can be seen directly as an increase (decrease) in the S (W) parameter. Absolute values from different experimental setups are obviously not comparable due to experimental variations and the freedom in parameter definition, but relative values S/S_B and W/W_B, where B refers to the bulk state, are less sensitive to such factors. [10]

It is also common to use S vs. W plots, where the (S,W) values are parameterised by a measurement variable such as implantation depth, temperature, etc. Each annihilation state, including trapped states and the free state, has its characteristic point on the (S,W) plane. For instance, in the presence of a single type of trapping defect D, the parameterised points will fall on the line between the points corresponding to the bulk and defect state, (S_B,W_B) and (S_D,W_D), respectively, since

$$S = \eta S_D + (1-\eta) S_B, \quad W = \eta W_D + (1-\eta) W_B. \tag{13}$$

The position on the line is determined by the intensity of the defect signal, which in turn depends on the defect concentration. [10]

Also lineshape ratio curves are used in data analysis [8]. Different variants and combinations of momentum and lifetime techniques also exist, such as coincidence variants with multiple detectors, angular correlation of annihilation radiation (ACAR), age–momentum correlation (AMOC), etc. [8, 88] The simplest enhancement is the coincidence setup, in which both annihilation photons are detected using two detectors on opposite sides of the sample. This improves the signal-to-noise ratio in the lineshape histogram significantly—although at some cost in collection efficiency—thereby improving the resolution especially for examining the high-momentum regions of the lineshape.

2.4 Slow-positron beams

For studying surface layers, fast positrons from nuclear reactions are unsuitable as such. Radioisotope sources have β^+ ranges of the order of 0.1–1 mm in solids. In order to examine well-defined near-surface regions, the fast positrons need to be moderated to the eV range. These monoenergetic slow positrons can then be accelerated to the desired implantation energy using an electromagnetic transport system and high-vacuum conditions to convey the particles to the target sample. Typically, acceleration energies between, e.g., 0.1–40 keV are used, although even lower kinetic energies are used in other surface studies and techniques, such as positronium studies, LEPD or positron Auger-electron spectroscopy (PAES) [4]. At higher energies, the depth resolution becomes smeared by the broadening of the implantation depth distribution $p(z)$. The implantation profile for monoenergetic e^+ is given by the semi-empirical form [8, 96]

$$p(z) = -\frac{\mathrm{d}}{\mathrm{d}z}\exp\left(-\left(\frac{z}{z_0}\right)^2\right) = 2\frac{z}{z_0^2}\exp\left(-\left(\frac{z}{z_0}\right)^2\right), \tag{14}$$

known as the Makhov profile, which relates to energy through the mean implantation depth by $\bar{z} = \sqrt{\pi} z_0 / 2 = AE^n$ keV. A usual value for n is 1.6, and A is given by

$$A = \frac{4}{\rho}\mu\mathrm{gcm}^{-2}, \tag{15}$$

where ρ is the specific mass of the host lattice. Figure 4 shows the implantation profile in silicon for different energies.

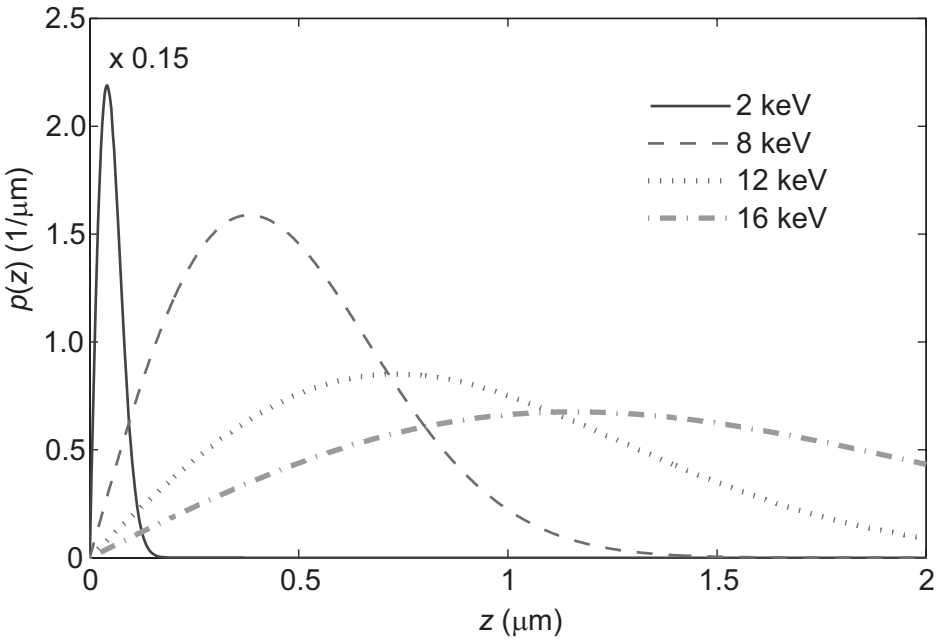

Figure 4. Positron implantation profile for different energies in silicon. The 2 keV curve has been scaled for illustrative purposes. Based on Ref. [81].

2.4.1 Positron moderation and slow-positron beams

Fast-positron moderation is simple to accomplish with a fast-to-slow positron converter composing of a suitable material that has a negative work-function for positrons (see, e.g., Ref. [86]). The fast positrons are targeted at the converter where they are allowed to thermalise. By diffusion, some of the thermal positrons reappear at the surface of the converter and are spontaneously emitted, ideally with a kinetic energy equal to the work-function (~1 eV) of the converter material.

Appropriate materials include several elemental metals, of which thermally annealed W has become the de facto choice owing to its high moderation, i.e., fast-to-slow positron conversion efficiency [13, 97–108]. A heat treatment is applied to the converter, on one hand, to remove lattice imperfections and impurity atoms that shorten the diffusion length, and on the other hand, to remove surface contaminants, such as carbon. However, it is clear that due to the short diffusion length, inevitably a large number of the positrons are lost via annihilation in the converter.

In the usual laboratory geometry, a thin (~1 μm) converter foil is placed on top of the β^+ source, and the slow positrons are extracted from the outer face of the foil. The β^+ endpoint energy for ^{22}Na is 546 keV, so most of the fast positrons penetrate the foil at high energies [109]. Hence, the fast-to-slow conversion efficiency is low, typically only 10^{-5}–10^{-4}. A stronger source (~1 GBq/30 mCi or more) is therefore needed in order to keep data collection times reasonable. The slow positrons are filtered from the fast ones just after the moderation stage with a velocity selector. The moderation efficiency can be slightly improved by using creative geometries that increase the converter's surface coverage [86, 110]. In the simplest case, the use of tungsten mesh instead of foil has been observed to improve the efficiency slightly, although this introduces some energy spread to the beam because of the larger emission angles [111, 112]. In any case, the sample and detectors need to be placed far (~meters) from the source/moderator due to the high background from the primary source and from the fast (unmoderated) positrons that are annihilated at the velocity selector. Therefore, an electromagnetic transport system and high-vacuum conditions are needed to convey the slow positrons to the target sample [113–115]. These instruments are hence termed (slow) positron beams [4, 116].

The energy width of the spontaneously emitted slow positrons is narrow, nearly equal to the thermal spread [98, 107]. Other converters such as solid rare-gas moderators [117–125] and modified Penning traps [118, 126, 127] offer sources for cold positrons at high conversion efficiencies. In a Penning trap, large numbers (up to 10^7) of positrons are accumulated and cooled in a magnetic bottle containing a low-pressure cold buffer gas, from which they can be released in short (~10 μs), dense bursts by applying a gate potential. Storage times can be up to the order of 10^3 s, and presently the plasma density can reach 10^5 cm^{-3}, and can be released in bunches containing 10^5 particles. The positrons are very cold, reaching widths of 18 meV. These traps are commercially available and have gained popularity in other applications such as fundamental physics and antimatter research (see, e.g., Refs. [128–130]).

2.4.2 Beam timing

Monoenergetic DC beams suitable for Doppler broadening studies are relatively simple to construct. Regarding timing, however, the positron "birth" information is lost, firstly due to the huge rate of false START gamma signals, and secondly due to the time variations in the moderation process. To perform lifetime spectroscopy, the particles need to be time-stamped by appropriate means. The most common way is by modulating the velocity of the DC beam using electric fields to compress the beam into short bunches [34–38]. The beam is periodically accelerated and decelerated, causing it to compress in time at a specific focal distance. The arrival time of the bunch at the target is then provided by the bunching electronics, short of some fixed delay. The beam bunching techniques have been adopted from ion and electron beam bunching [131–133], and these beams are commonly referred to as pulsed positron beams. The best

existing setups can achieve time resolutions comparable to ordinary fast-positron spectrometers used routinely in bulk studies [36, 38].

Also secondary electrons emitted in the impact of the positron with the sample have been used to obtain a timing signal [25, 32]. While this is a simpler method from the technical point of view, it suffers from somewhat poor time-resolution. Also, several effects related to the secondary electron emission process complicate the data-analysis, because they produce undesirable artefacts in the experimental data.

2.4.3 Lifetime depth-profiling

A fundamental difference in slow-positron lifetime spectroscopy is that, due to the contribution of surface states and material interfaces, the lifetime distributions are not generally of the sum-of-exponentials form as in bulk studies (Sec. 2.1 & Eq. (9)) [80, 134–137]. This approximation can, however, be used in homogeneous layers at a sufficient distance from the surface or other interfaces. In near-surface layer and depth-profiling studies, the diffusion equation (Eq. (4)) needs to be solved in one dimension (depth from the surface) to fit the experimental spectra in a physically meaningful way.

In the case of a single, semi-infinite material layer ($z > 0$), the diffusion–annihilation equation becomes [81]

$$\frac{\partial}{\partial t}u(z,t) = \frac{\partial}{\partial z}\underbrace{\left(D(z)\frac{\partial}{\partial z}u(z,t) - \mu(z)E(z)u(z,t) \right)}_{\equiv -J(z,t)} - \lambda u(z,t) + S(z,t) \tag{16}$$

with the initial and boundary conditions

$$\begin{aligned} & u(z,0) = p(z), \\ & J(0,t) \equiv D(0)\frac{\partial}{\partial z}u(z,t)\Big|_{z=0} - \mu(0)E(0)u(0,t) = \nu u(0,t), \\ & \lim_{z\to\infty} u(z,t) = 0, \end{aligned} \tag{17}$$

where ν is the transition rate to surface states, and $J(z,t)$ denotes the positron flux towards the positive z axis. The surface transition rate can further be divided into the transition rates to the trapped surface state S and surface Ps, $\nu = \nu_S + \nu_{\mathrm{Ps}}$.

In addition, the kinetic equations for the total transition rates between different states are [81]

$$\begin{aligned}
\frac{\mathrm{d}}{\mathrm{d}t} n_B(t) &= -(\lambda_B + \kappa) n_B(t) + \delta n_D(t) + J(0,t), \\
\frac{\mathrm{d}}{\mathrm{d}t} n_D(t) &= \kappa n_B(t) - (\lambda_D + \delta) n_D(t), \\
\frac{\mathrm{d}}{\mathrm{d}t} n_S(t) &= -\lambda_S n_S(t) - \frac{\nu_S}{\nu} J(0,t), \\
\frac{\mathrm{d}}{\mathrm{d}t} n_{\mathrm{Ps}}(t) &= -\lambda_{\mathrm{Ps}} n_{\mathrm{Ps}}(t) - \frac{\nu_{\mathrm{Ps}}}{\nu} J(0,t).
\end{aligned} \tag{18}$$

Note that, for simplicity, different trapping defects are represented here by a single defect, denoted with the subscript D. Furthermore, the *p*-Ps and *o*-Ps states are also represented by a single state. The kinetic equations hold also for the densities $u(z,t)$. The measured quantity, the lifetime spectrum, is the total annihilation rate

$$-\frac{\mathrm{d}}{\mathrm{d}t} N(t) = -\frac{\mathrm{d}}{\mathrm{d}t} \left(n_B(t) + n_D(t) + n_S(t) + n_{\mathrm{Ps}}(t) \right). \tag{19}$$

The problem reduces to seeking the free-positron density $u_B(z,t)$, because the occupation density/numbers of the defect, surface, and Ps states, and, by Eq. (6), also the source term, can be expressed with u_B as following [81]:

$$\begin{aligned}
u_D(z,t) &= \kappa \int_0^t \exp\left((\lambda_D + \delta)(t' - t) \right) u_B(z,t') \, \mathrm{d}t', \\
n_{S,\mathrm{Ps}}(t) &= \exp\left(-\lambda_{S,\mathrm{Ps}} t \right) \int_0^t -\frac{\nu_{S,\mathrm{Ps}}}{\nu} \exp\left(\lambda_{S,\mathrm{Ps}} t' \right) J(0,t') \, \mathrm{d}t', \\
S(z,t) &= \delta u_D(z,t).
\end{aligned} \tag{20}$$

Thus, the task is to seek the solution to the nonlinear problem

$$
\begin{aligned}
&\frac{\partial}{\partial t}u(z,t) = \alpha(z)\frac{\partial^2}{\partial z^2}u(z,t) - \beta(z)\frac{\partial}{\partial z}u(z,t) - \gamma(z)u(z,t) \\
&+ \int_0^t g(t,t')u(z,t')\,\mathrm{d}\,t' \quad \text{in } (0,\infty)\times(0,\infty), \\
&u(z,0) = p(z), \quad z \geq 0, \\
&\alpha\left.\frac{\partial u}{\partial z}\right|_{z=0} = (\beta(0)+\nu)u(0,t), \quad t \geq 0, \\
&\lim_{z\to\infty} u(z,t) = 0, \quad t \geq 0,
\end{aligned}
\tag{21}
$$

where $\alpha(z) = D(z), \quad \beta(z) = \mu(z)E(z) - \frac{\mathrm{d}}{\mathrm{d}z}D(z), \quad \gamma(z) = \mu(z)\frac{\mathrm{d}}{\mathrm{d}z}E(z) + E(z)\frac{\mathrm{d}}{\mathrm{d}z}\mu(z) + \lambda,$ and $g(t,t') = \kappa\delta\exp((\lambda_D + \delta)(t'-t))$. An example of the time evolution described by Eq. (21) using typical material characteristics and implantation energies is shown in Figure 5. It can be seen that for high energies, the evolution is dominated by annihilation, while with lower energies, diffusion has a strong effect.

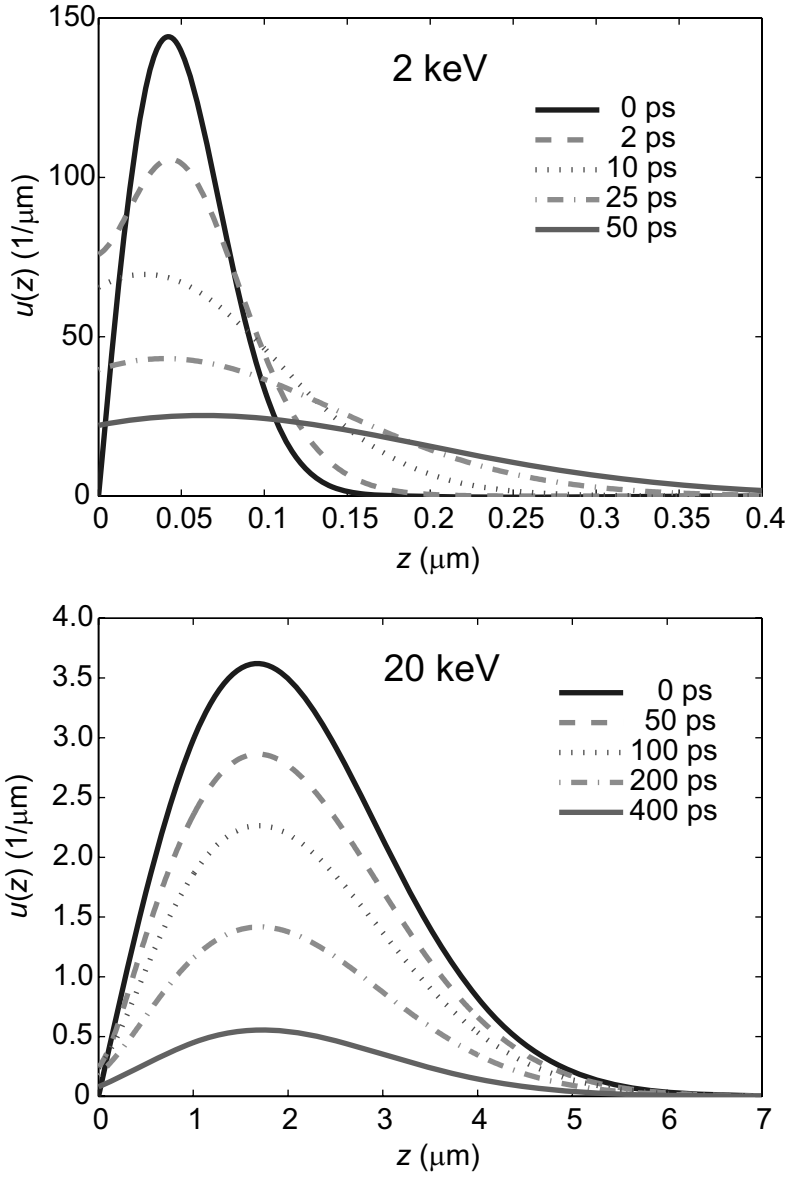

Figure 5. Time-evolution of the positron density described by the diffusion equation, plotted for two different (low and high) implantation energies. Based on Ref. [81].

Generally, Eq. (21) needs to be solved numerically, which makes the data analysis computationally more tedious. Also, because the values of the additional material parameters D, μ, E, ν_S, ν_{Ps}, and λ_S are often also unknown, the number of free parameters in experimental data fitting can become unreasonably large with respect to the statistical accuracy of the data. The situation is somewhat improved if one can make some sophisticated assumptions on the material properties. Therefore, it is useful to complement lifetime data with slow-positron Doppler-broadening, since lineshape data is simpler to analyse, as one needs to solve only the steady-state diffusion equation, which can be used to gain information on the material-specific parameters [13, 138,

139]. However, in multilayered structures, the implantation profile presents further difficulties, and we thereby restrict ourselves here to single layers [140].

3 Pulsed slow-positron beam

In this chapter, a new laboratory-scale pulsed positron beam, constructed at the Department of Applied Physics, Aalto University, Finland, is presented and discussed, with emphasis on the author's contribution.

3.1 Overview

An operational diagram and a drawing of the pulsed positron beam are shown in Figure 6 and Figure 7, respectively, and Figure 8 shows photographs of the instrument. The system achieves a characteristic overall time resolution of roughly FWHM = 270 ps, with an energy range selectable from 2 to 25 keV. A conventional ~20–50 mCi encapsulated ^{22}Na laboratory source, coupled to a heat-treated W-foil moderator, is used as the source for the slow-positron (~1 eV) beam [141]. The beam is magnetically transported to a three-stage radio-frequency (RF) beam-bunching system (termed 'pulsing system'), which time-compresses the beam into bunches shorter than 200 ps FWHM in 30 ns repetition periods. The pulsing system consists of a prebuncher, a beam chopper, and a main buncher, including their accompanying (pre)acceleration stages. After the bunching stages, the beam is electrostatically accelerated to the selected implantation energy. The typical data collection time for a single lifetime spectrum is in the range between 1 to 10 hours, and a full depth-scan can be performed in 1–10 days, depending on the source activity.

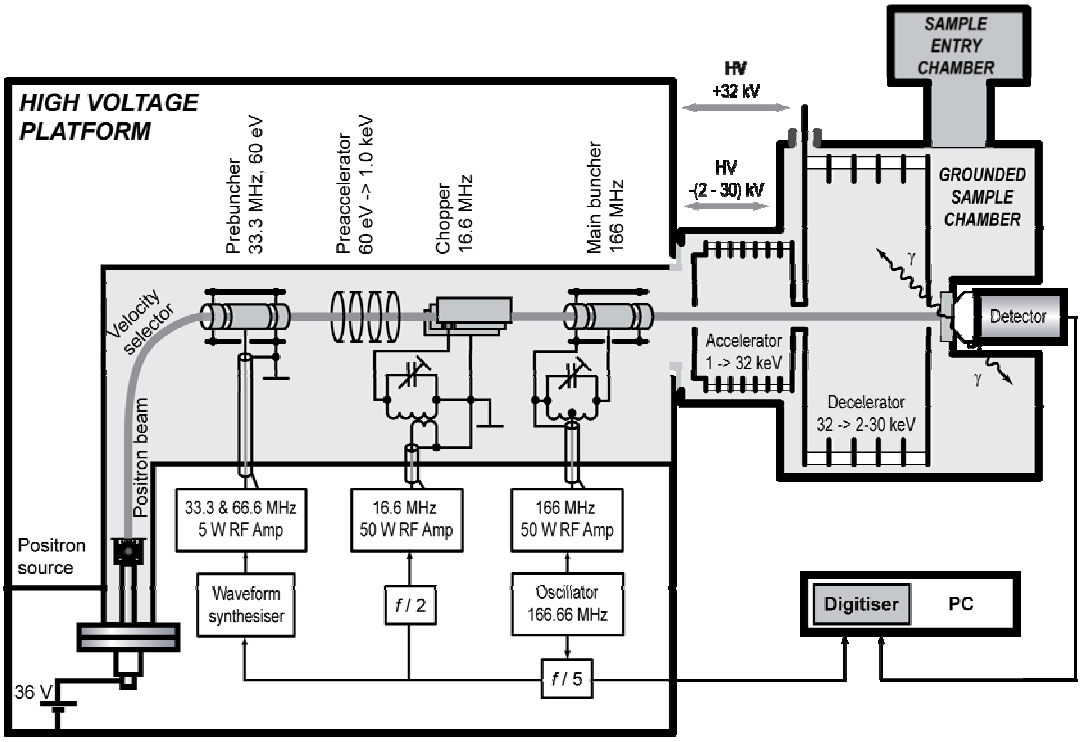

Figure 6. Diagram illustrating the operational principle of the pulsed positron beam. For illustrative purposes, the radio-frequency electronics have been simplified. At present, the two-stage final acceleration in the accelerator-decelerator is not used—in the present configuration, the decelerator electrodes are grounded. Based on Refs. [1, 39, 142].

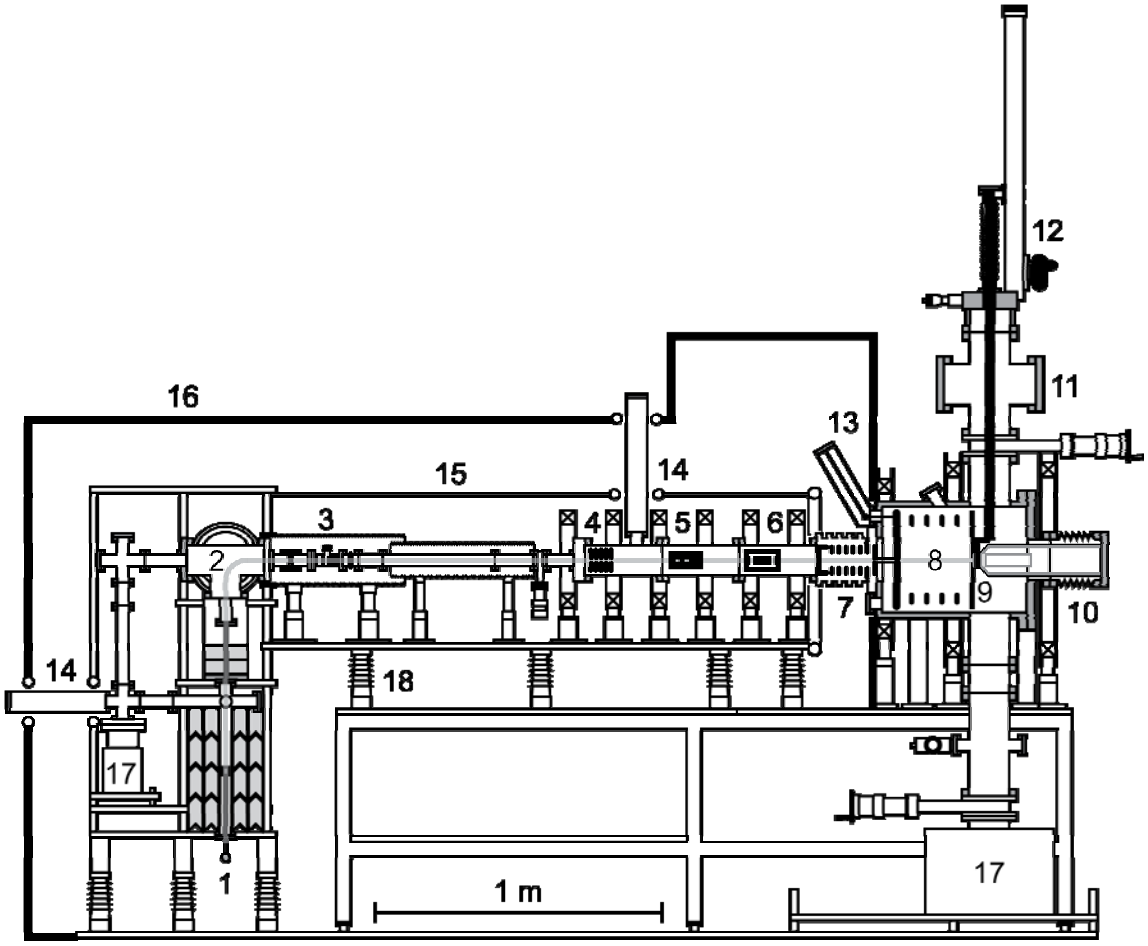

Figure 7. Scale drawing of the beam. 1. Positron source and moderator. 2. Velocity selector. 3. Prebuncher. 4. 1.0 keV preaccelerator. 5. Chopper. 6. Main buncher. 7. Main accelerator. 8. Decelerator. 9. Room-temperature sample holder. 10. Scintillation detector. 11. Load-lock sample entry chamber. 12. Room-temperature sample transfer stage. 13. Polyoxymethylene (POM) high-voltage (HV) feedthrough. 14. POM vacuum-pump feedthroughs. 15. HV platform Faraday cage. 16. Earth Faraday cage. 17. Ion pumps. 18. Standoff insulators. From Ref. [142].

Figure 8. Photographs of the pulsed positron beam.

A novel feature of the instrument is that the lifetime measurement is performed entirely digitally, using a high-speed digitiser accompanied by in-house signal processing software [90–94]. The digital setup enables versatility in data processing far beyond the reach of conventional analogue electronics. The lifetime START and STOP signals are obtained from the anode output of the fast scintillation detector and the crystal oscillator of the RF pulsing system. A fast micro-channel plate (MCP) detector can be used in calibration and beam diagnosis in place of the scintillation detector [143].

Another unique feature is that the specimen is maintained at ground potential during measurements to facilitate sample manipulation, i.e., moving, heating, cooling, biasing, etc. [142, 144, 145]. This is accomplished by floating the source and pulsing system instead. As a drawback, this realisation naturally places heavier requirements to ensure device and personnel safety, which, in this case, have been fulfilled by robust mechanical and electrical design, real-time status monitoring, and automatic shutdown procedures in fault situations, along with sufficient safety precautions.

The final beam diameter, determining the minimum sample size, is ∅3–4 mm. There are two separate sample holders—one for measurements at room temperature, with a magazine accommodating up to six samples, and another one for variable sample-temperature (~20–600+ K). There are open ports in the specimen chamber to accommodate for additional sample manipulation. It would in principle be straightforward to include a Ge detector for momentum studies, but this is not being planned at the moment. For example, sample illumination could be synchronised with the pulsing system, enabling the observation of transient effects in photoexcitation.

Ideally, a positron lifetime beam enables the study of positron diffusion and other time-dependent phenomena [80, 135]. In practice, however, the positron pulse width is comparable to typical lifetimes, and the beam bunching process itself introduces a number of parameters that affect the overall instrument time-response/resolution. This makes data analysis more complicated and error-prone than in the case of fast-positron spectrometers, since the resolution function is of a more complex nature. In addition, the diffusion equation inevitably requires numerical solving techniques, which brings a further source of error [81]. These issues are discussed in Sec. 3.5.

3.2 High-voltage design

In order to hold the sample at earth ground, a large proportion of the instrument needs to be floated at the implantation voltage. The high-voltage (HV) platform, comprising most of the beam line itself and the accompanying electrical cabinets, is surrounded by an earth-potential Faraday cage, realised with stainless-steel expanded-metal fencing, to protect personnel from electric shock and the system from breakdowns and electromagnetic interference [146, 147]. The portion of the beam line situated in the

platform is also entirely enclosed in a similar Faraday cage, supported by standoff insulators. Polyoxymethylene plastic is applied to great extent as a high-vacuum compatible insulator material in vacuum feedthroughs, accelerator structures, etc., further owing to its good machining properties. To ensure the HV withstand of the platform and to prevent breakdown-related phenomena, special attention has been payed in mechanical and geometrical design to avoid excessive local field strengths. The surfaces of the HV platform are cleared of sharp edges that otherwise might induce corona. Also, the HV resistors are air-insulated, which eliminates the risk of partial-discharge effects.

Figure 9 shows the HV circuit. In the event of a breakdown, the load resistors R_2 and R_3 in the outputs of the HV power supplies limit the peak current to the sub-mA range. The bypass resistors R_1 and R_4 are needed because of the sourcing-only nature of the power supplies. More information on the HV design can be found in Ref. [142].

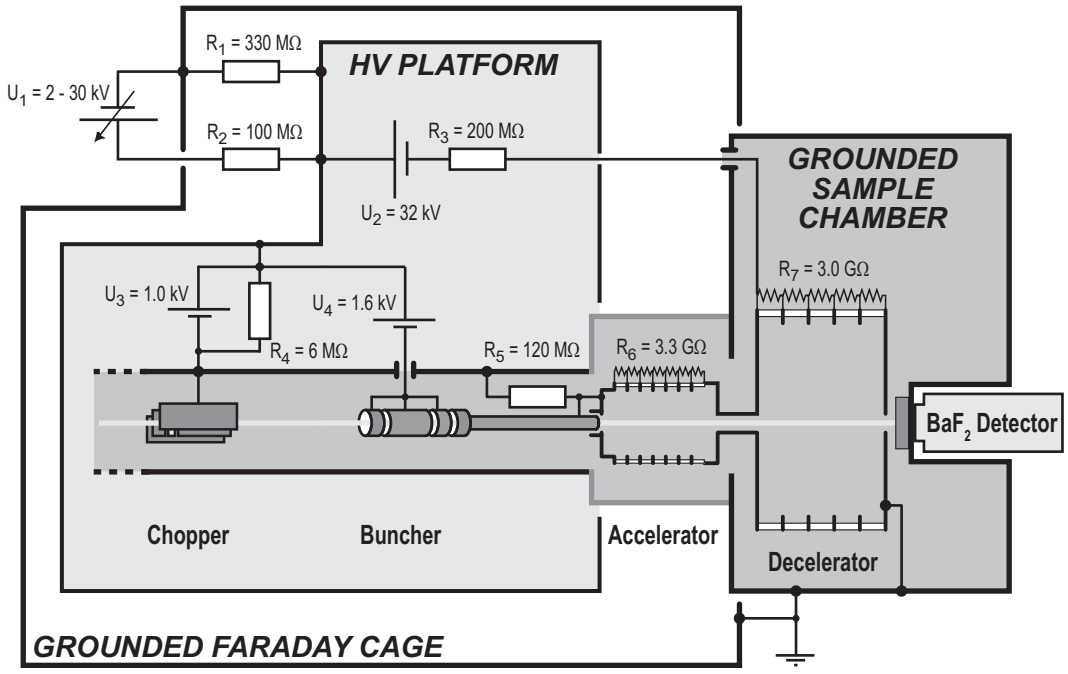

Figure 9. HV floatation circuit. The HV platform is floated at the positron implantation potential U_1 by a Glassman EH series HV power supply. Resistors R_1–R_3 are air-insulated series resistor chains in acrylic tubing. The in-vacuum resistors R_5–R_7 are non-magnetic, vacuum compatible precision HV resistors (Ohmite MOX-1125-22 and MOX-750-23). Based on Ref. [142].

3.2.1 Overvoltage protection

A considerable amount of the electronics equipment is situated in the HV platform. The mains power is fed via a 100 kV/5 kVA AC (alternating current) insulation transformer (Hipotronics Ruby series IT100-5E). The capacitive energy stored in the platform can be up to about 1 J—the capacitance between the HV platform and earth is about 1 nF. Regarding signal transit times, the physical dimensions of the platform are relatively large. An electrical breakdown could hence induce transient overvoltages between electronics ground and input/output. Therefore, several precautions have been taken to protect the electronics from breakdown-induced damage. These include multi-stage transient-surge suppressors both in mains and DC and RF lines, along with thorough electromagnetic interference (EMI) shielding of electrical enclosures and transmission lines. The output lines from the cabinet are individually coaxially screened by stainless-steel mesh, and the cabinet enclosure (Figure 8) itself is also EMI shielded, with shielded feedthroughs and heavy ground connections. The DC lines are each separately protected at their outputs with triple-stage transient protection devices, consisting of an LC suppressor, a gas-discharge tube, and a Zener diode. Furthermore, transient absorbers are placed near the inputs of the coil magnets. The inputs of the preaccelerators are equipped with HV gas discharge tubes. The RF high-power amplifiers in turn are protected by commercial transient absorbers (Fischer Custom Communications Spikeguard Suppressor FCC-550-20 and FCC-250B-230).

3.2.2 Safety interlock

The platform is equipped with an electromechanical safety interlock, which shuts down the HV power supplies and grounds the platform upon attempt-of-entry to prevent injury to personnel (Figure 10). The interlock is realised with a combination of relays, gravity-operated solenoid-latch switches, and industrial micro-switches that instantaneously ground the platform and disconnect the mains of the relevant power supplies when the entrance door to the platform is opened. The solenoid latches fall upon the roof of the electrical cabinet, one forming contact to ground and another disconnecting power to the HV power supplies U_2–U_4 in Figure 9 by hitting a micro-switch placed on the roof. The mains of U_1 is behind a common switch with the solenoid DC supply, so that it is also switched off when the door is opened.

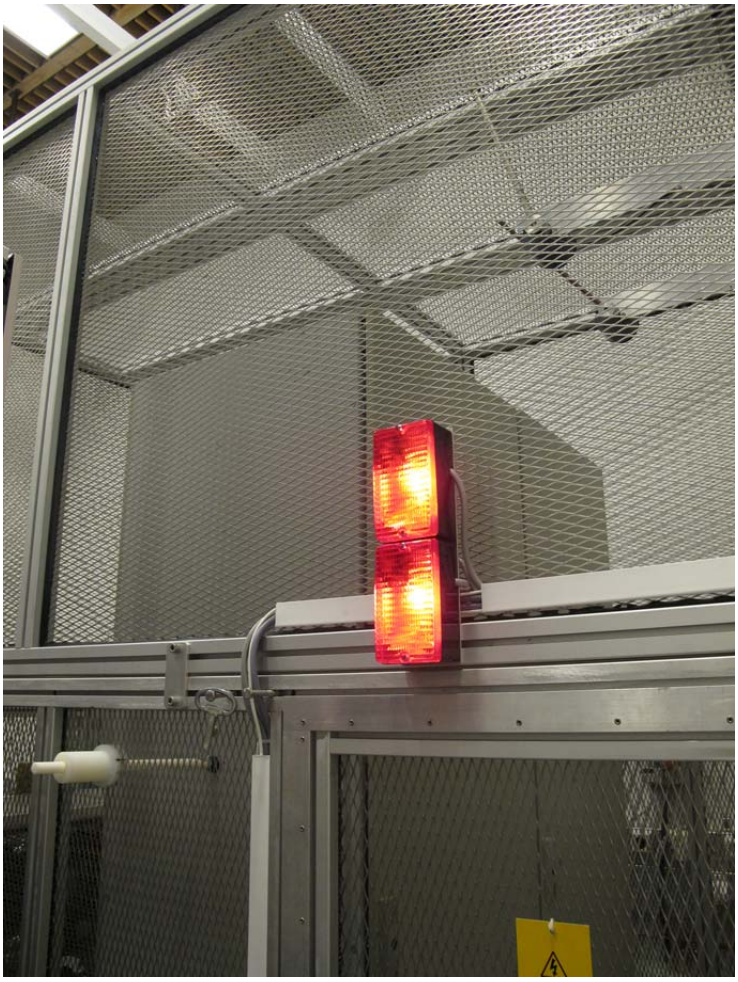

Figure 10. Photograph showing some of the HV safety features. The warning lights indicate that the platform is energised. On the top-right of the picture, above the electrical cabinets, are the interlock solenoid latches (see text). The insulator rod on the bottom-left is for switching off the decelerator power supply (U_2 in Figure 9) from outside of the platform in case of emergency.

3.2.3 Control system

The pulsing system and acceleration stages are controlled from a PC workstation using the National Instruments LabVIEW platform. The software, described in Ref. [148] and illustrated in Figure 11, commands two banks of National Instruments FieldPoint I/O modules—one situated in the HV platform, and one in ground potential, communicating via optical-fibre and twisted-pair Ethernet—which in turn remote-control and monitor the relevant DC power supplies and RF electronics. Vacuum levels are also monitored, since the accelerator-decelerator and bunching elements are not designed for operation at elevated pressures. To safeguard the components, the program reacts to abnormal

readings from the HV circuit and to failure in mains power or vacuum by shutting down the acceleration and bunching voltages in a controlled fashion. The mains supply to the relevant electrical equipment, including vacuum pumps, is battery-backed by a 3 kVA UPS (uninterruptable power supply) in case of power failure. The automatic shutdown procedures could be initiated by communication with the UPS, but at the moment they are triggered via a relay output from one of the non-power-backed vacuum gauge controllers.

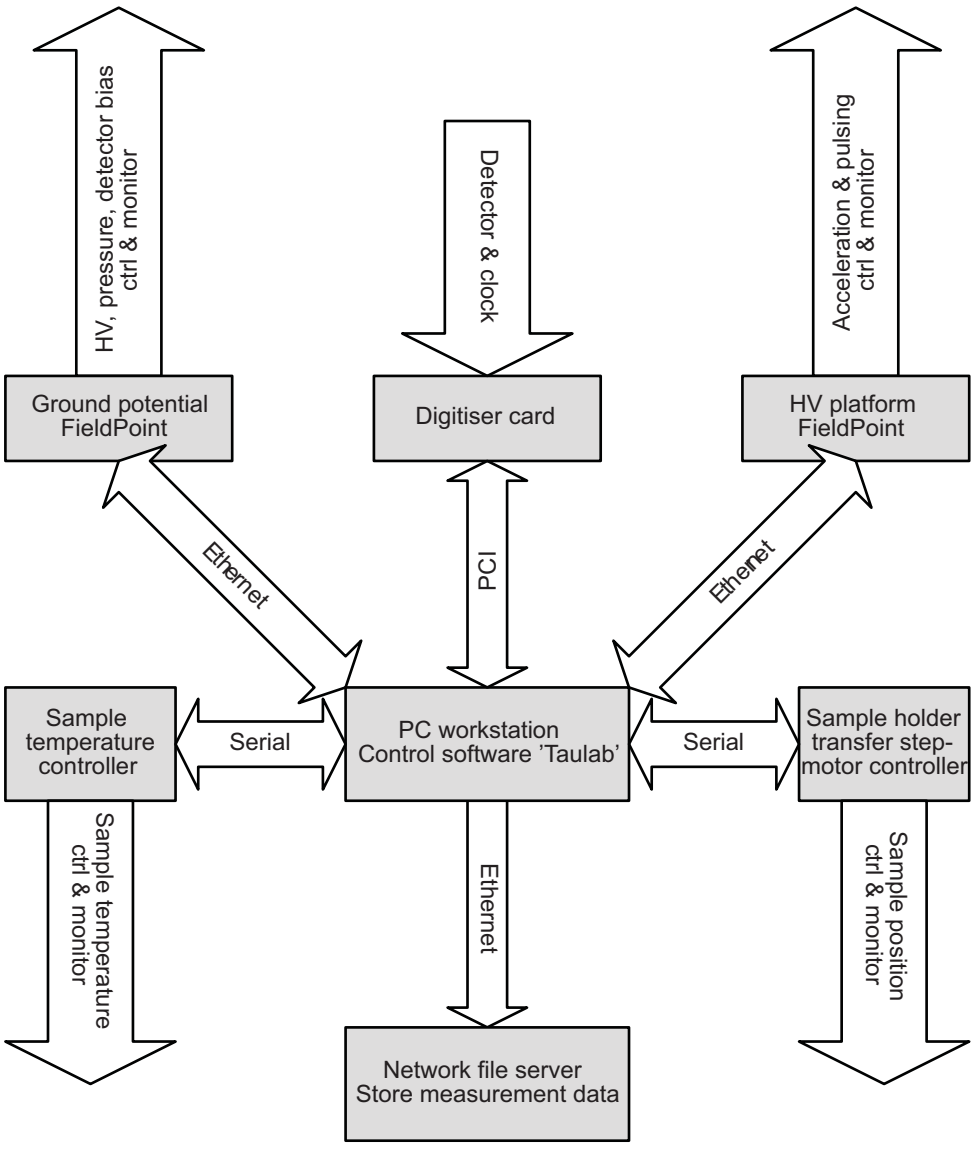

Figure 11. Block diagram of the control system. The sample temperature is controlled by a Lakeshore 331 temperature controller coupled to a closed-cycle He cryocooler (Advanced Research Systems DE-202). The temperature of the coldhead is measured with a silicon diode sensor and a thermocouple. The HV platform FieldPoint bank also monitors the cabinet temperature by a set of thermocouples.

Also, four K-type thermocouples monitor temperatures inside the electrical cabinets. To minimise the risk of overheating, the cabinets are air-cooled with a redundant set of long-life (200,000 h) 120 mm case fans. Additionally, to prevent vacuum-related problems from damaging the MCP detector, the software also responds in fault situations by automatically shutting down the detector bias.

3.3 Beam pulsing and transport

3.3.1 Source and transport

The W-foil moderator is used in transmission geometry, i.e., the slow positrons are extracted from the opposing face of the film. The foil has a thickness of 1 μm and is mounted on top of the source capsule right above the active window. The source/moderator has an active area of ∅4 mm. The foil is thermally annealed prior to use by electron bombardment at above 2000°C to increase the conversion efficiency.

The slow positrons emitted from the foil have a kinetic energy corresponding to the ~3 eV positron work function of W, ideally with thermal energy width [98, 101]. However, due to surface roughness and other effects, the initial energy spread of the beam can be up to some hundreds of meV. The positrons are extracted from the foil with a low-ripple 36 V bias voltage applied to the source–moderator assembly. The particles are then magnetically guided by a collection of current-solenoids, Helmholtz coils, and steering coils. The coils generate a magnetic field of 5–10 mT coaxially with the vacuum tubing, which confines the particles into parallel with the beam line. The field forces the slow positrons on helical trajectories along the magnetic flux lines, with Larmor radii in the sub-millimetre range. A bend in the beam line (see Figure 6) near the source acts as a magnetic velocity selector, removing the remaining high-energy positrons that penetrate the moderator foil through impact with the vacuum tubing [149].

A high vacuum around 10^{-6} mbar is required for a sufficient mean free path from the source to the sample. This is produced by two turbomolecular pump stations and two ion pumps (75 l/s and 300 l/s nominal capacities). The Helmholtz coil magnets from the end of the drift tube onwards are separately cooled with long-life fans.

The initial fast-positron flux is determined by the nominal activity of the source and the positron yield of the source capsule. The capsule is described in detail in Ref. [141]. The β^+-decay branching ratio of ^{22}Na is 90%, but the finite escape probability from the capsule also needs to be taken into account. Positron yields of typical sources were therefore determined in Publ. I. The first method was a coincidence gamma-detection setup, where a collimator was placed in front of the source, and the positron flux through the collimator aperture was determined by detecting the annihilation radiation

at a target located behind the collimator. The method suffers from imprecision, since it is sensitive to many geometrical factors such as the solid angles spanned by the detectors and the angular distribution of the positron flux from the source. Therefore, a more precise and also simpler method was also used, in which the electrical current to the source induced by the positron emission was measured. Based on the results of both methods, a typical fast-positron yield of around 30% was concluded.

Also the moderation efficiency of the W foil was measured with a similar coincidence setup. Despite several heat-treatments, only an efficiency in the lower 10^{-5} range (for the encapsulated ^{22}Na) could be achieved. Depending on the source activity, the initial beam flux is thus in the range 10^3–10^4 s^{-1}. It should be mentioned that in the literature, the efficiency is often defined simply as the ratio of the slow-positron flux and the nominal activity of the source. This is somewhat ill-defined, since as shown in Publ. I, the source yield can vary individually due to factors in the manufacturing process. Here, the yield is taken into account in the definition. Since the yield is typically much less than 100%, moderation efficiency values reported in the literature are not necessarily comparable.

3.3.2 Beam bunching

This section is based on Refs. [1, 40, 143]. Figure 12 depicts the pulsing system and the time structure of the beam at the different stages. The fundamental frequency of the pulsing system is 33.3 MHz. The repetition period needs to be sufficient to allow for the positrons to annihilate completely (within statistical accuracy) before the following cycle. The 33.3 MHz repetition rate corresponds to a period of 30 ns, which is more than sufficient for lifetimes in solids.

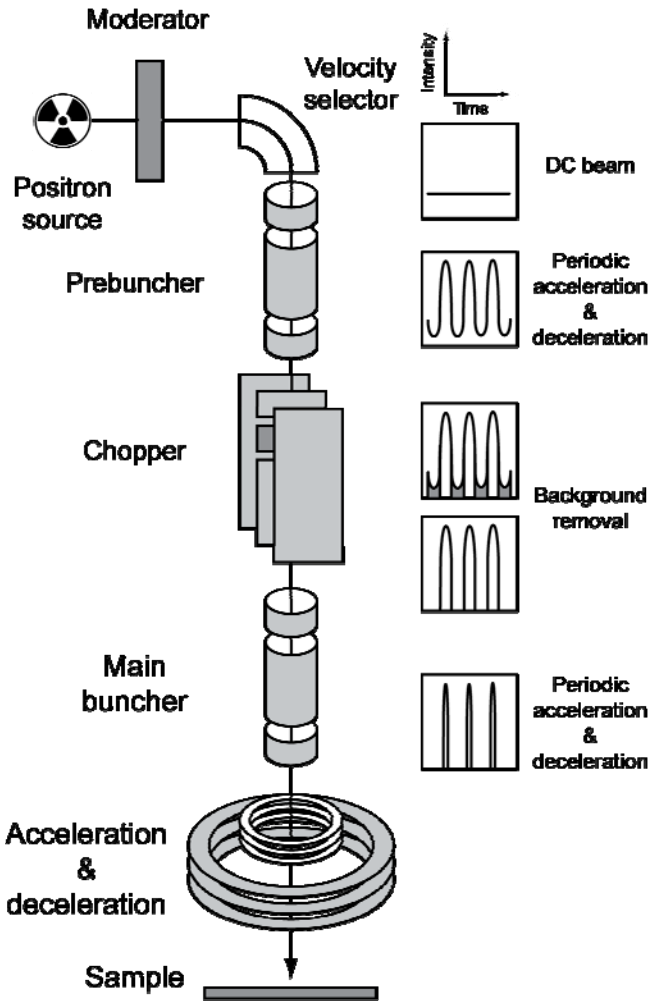

Figure 12. Simplified illustration of the pulsing system and the time structure of the beam at different stages. Based on Ref. [40].

The first stage is an impedance-unmatched double-gap prebuncher, where the beam undergoes energy modulation by a 33.3 MHz sine wave and its first harmonic, representing the first two Fourier terms of the ideal bunching waveform, presented below [150]. The prebunching stage is illustrated in Figure 13. The positrons receive a longitudinal acceleration/deceleration over the gaps, depending on their arrival time with respect to the modulation phase. The particles that arrive at the prebuncher early in the repetition period are slowed down, while those arriving later are accelerated. During their flight in the (electric-field-free) drift region behind the prebuncher, the particles thus begin to "catch up" with each other (see Figure 13). This periodically time-compresses the beam into narrow bunches at a specific focal distance behind the prebuncher [151–154]. In this case, the time focus is set at the subsequent beam chopper and the phase is set to match the acceptance time of the chopper. This way, the overall bunching efficiency, i.e., the portion of the DC beam that is utilised for time-compression, is increased [155–157], since a smaller portion of the beam is then suppressed in the chopping. The improvement is around a factor of 5.

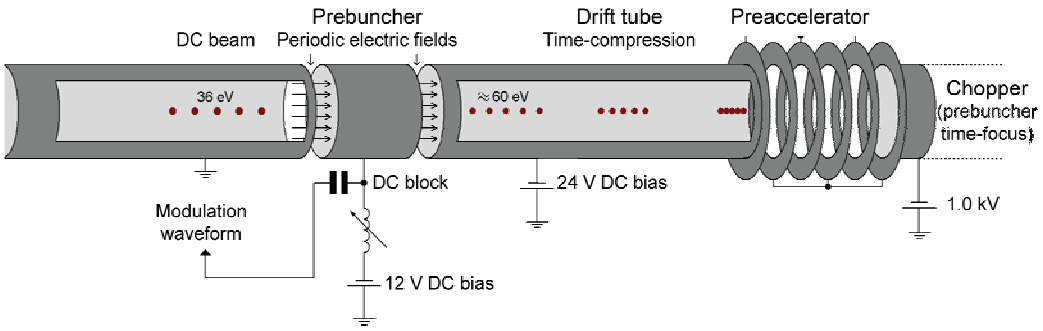

Figure 13. The prebunching stage. The prebuncher time-compresses the incoming DC beam into short (a couple of ns FWHM) bunches before the second stage, the chopper. This improves the overall bunching efficiency. Based on Ref. [158].

The arrival time of a particle at a distance L beyond the prebuncher is given in the classical regime by

$$T(t) = t + \tau(t) = t + \frac{L}{v(t)} = t + L\sqrt{\frac{m_e}{2(E_0 + eU(t))}}, \tag{22}$$

where t is the arrival time at the prebuncher, τ is the flight time over the distance L, v is the modulated velocity, E_0 is the initial kinetic energy, and $U(t)$ is the modulation potential. It is approximated in Eq. (22) that the modulation occurs instantaneously over the gaps. This yields for the ideal modulation waveform [151], i.e., $T(t) = \tau_0$ (constant),

$$U(t) = \frac{E_0}{e}\left[\frac{1}{(1 - t/\tau_0)^2} - 1\right]. \tag{23}$$

Realising such a waveform at a frequency in the range 10^7–10^8 Hz is difficult. On the other hand, deviations from the ideal form induce background between the pulses, which must then be eliminated with a beam chopper. Ordinarily, the ideal waveform (Eq. (23)) is approximated with either a single or a few first Fourier terms. The first-order approximation gives

$$U(t) = U_0 \sin(\omega t) \approx U_0 \omega t = \frac{2E_0}{\tau_0 e} t \approx \frac{E_0}{e}\left[\frac{1}{(1 - t/\tau_0)^2} - 1\right], \tag{24}$$

where ω is the angular frequency. The required amplitude is then given by

$$U_0 = \frac{2E_0}{\tau_0 e\omega} = \frac{2}{e\omega L}\sqrt{\frac{2E_0^3}{m_e}}, \tag{25}$$

and the arrival time (Eq. (22)) becomes

$$T(t) \approx t + \tau_0 - \frac{\chi}{\omega}\sin(\omega t), \quad \chi = \frac{\omega L}{v_0}\frac{eU_0}{2E_0} = \frac{\omega L e U_0}{2}\sqrt{\frac{m_e}{2E_0^3}}. \tag{26}$$

Above, χ is called the (dimensionless) bunching parameter, which is essentially a normalised distance to the time focus, $\chi = 1$. Around the zero crossing of the modulation waveform, $T(t) \approx \tau_0$. In the case $\chi < 1$ ($\chi > 1$), the beam is said to be underbunched (overbunched). Increasing the bunching parameter is analogous to moving along the direction of the beam, i.e., increasing L, or, equivalently, increasing the bunching amplitude and/or frequency. The time evolution of the beam after bunching is illustrated in Figure 14. Before reaching the time focus, i.e., when $\chi < 1$, the ”late” particles have not gained on the “early” ones sufficiently, so the bunch is rather broad. When the beam is overbunched, i.e. when $\chi > 1$, on the other hand, the late particles begin to pass the early particles, resulting in the appearance of two separating peaks in the arrival-time distribution.

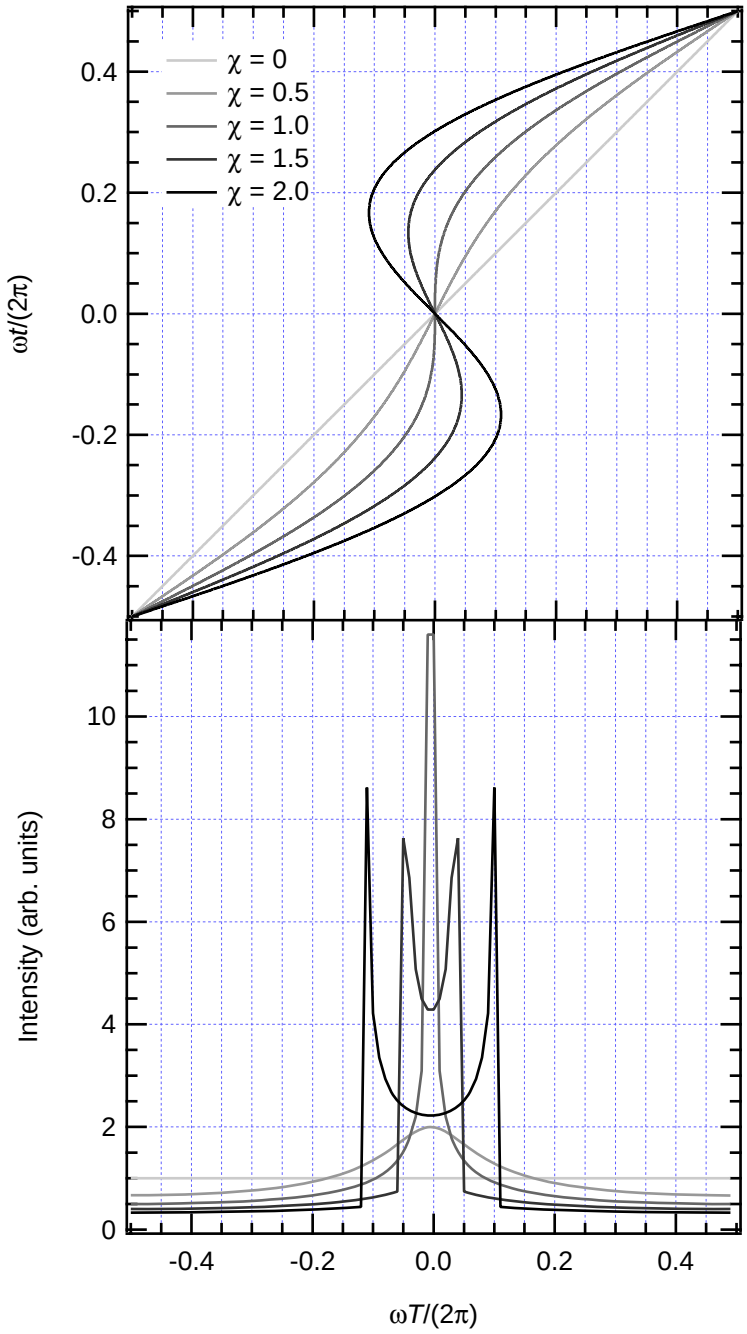

Figure 14. The time evolution of the positron beam in sinusoidal bunching. The upper figure shows the particle arrival time T at a distance L from the buncher (bottom axis) as a function of the arrival time t at the buncher (left axis) for different values of the bunching parameter χ. The lower figure shows the arrival-time (T) distribution, i.e., the bunch shape.

Physically, the prebuncher consists of three subsequent parallel tubular electrodes mounted inside the vacuum tubing. The modulation waveform is applied to the central

tube, and hence the incoming particle is either accelerated or decelerated over the electrode gaps, depending on which stage of the cycle it arrives at. Commonly, a transit-time factor is included in the bunching parameter χ that takes into account the flight time through the buncher [151]. The length of the central electrode corresponds to a change of sign in the waveform during the unmodulated time-of-flight, so that the acceleration (deceleration) occurs over both gaps. Since the beam energy needs to be kept sufficiently narrow for the final pulsing stage, i.e., the main buncher, the prebuncher is driven at low amplitude, in this case a few eV. The beam is also simultaneously statically accelerated over the gaps to 60 eV by applying additional low-ripple DC voltages to the electrodes.

The prebuncher is followed by a drift tube of roughly $L = 1$ m to allow for the beam to compress (cf. Eq. (26)). At the end of the drift tube, the beam is further accelerated to 1 keV just before the chopper. It is worth noting at this point that the 33.3 MHz repetition rate of the pulsing system is much higher than the average beam flux. Therefore, the terms ‘bunch’ and ‘pulse’ can be misleading, since, in fact, the majority of the cycles are empty, while the populated cycles in practice contain only a single particle. It is rather that the beam is compressed in the time domain instead of in space. Hence, space charge effects need not be taken into account.

The chopper (Figure 15) is a “sandwich” structure consisting of two parallel-plate electrodes, and a thin centre electrode between them. The incoming beam is split into two by the centre plate. A sinewave is fed to the central electrode, so that the beam can pass through the electrodes only during a short interval around the zero-crossing of the wave. Otherwise, the beam is deflected by the electric field and collides with the chopper structures. [1, 39]

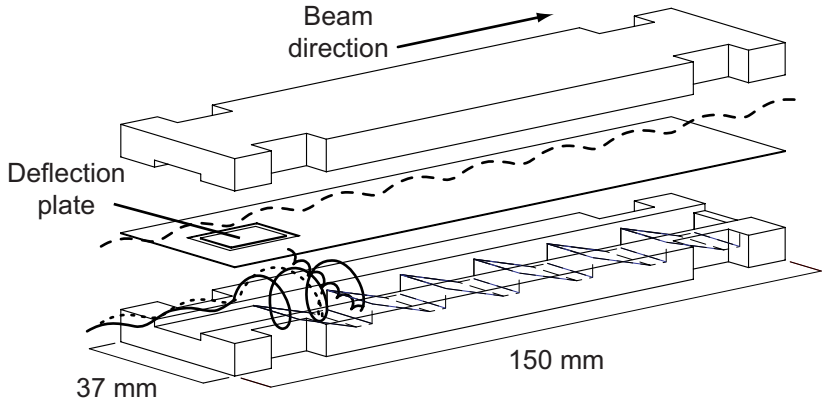

Figure 15. Exploded view of the chopper with examples of particle trajectories. A sinewave is applied to the deflection plate, allowing the beam to pass (dashed-line) only around the zero-crossing of the waveform. During the rest of the cycle, the beam is deflected to the chopper walls (solid and dotted lines). The saw-tooth patterns suppress scattering effects that increase the leakage outside the choppers acceptance time window. Based on Refs. [1, 159].

The outer electrodes of the chopper are machined from copper bricks. The sawtooth patterns are designed to prevent backscattered particles from leaking through the chopper [159]. The centre electrode is made from thin copper-clad plate. The chopper requires a signal amplitude of the order of 100 V, which is generated with an LC tank circuit connected in parallel with the chopper. A low loaded Q-value improves the temperature stability. The practical time window of the chopper is around 1.5–2.5 ns FWHM. [1]

In the ideal case, the chopper allows the beam to pass undisturbed during a selected interval $\left[\tau_0 - \Delta T/2\,,\, \tau_0 + \Delta T/2\right]$, and fully suppresses it during the rest of the cycle. The chopper determines the overall bunching efficiency, defined as

$$p = \frac{\omega \Delta t}{2\pi}, \tag{27}$$

where Δt is the initial time width that satisfies $T\left(\left[-\Delta t/2\,,\,+\Delta t/2\right]\right) = \left[\tau_0 - \Delta T/2\,,\, \tau_0 + \Delta T/2\right]$. Approaching time focus $\chi = 1$ from below, Eq. (26) gives by series expansion

$$\Delta T \approx (1-\chi)\Delta t + \underbrace{\frac{1}{24}\chi\omega^2 \Delta t^3}_{\Delta\tau_s}. \tag{28}$$

The nonvanishing term $\Delta\tau_s$ is due to the deviation from the ideal waveform, and can be categorised as spherical aberration. In terms of efficiency, it reads as

$$\Delta\tau_s = \chi\frac{\pi^3}{3}\frac{p^3}{\omega} \approx 10.3\chi\frac{p^3}{\omega}. \tag{29}$$

Thus, the aberration increases quickly with efficiency, but on the other hand decreases inversely with bunching frequency. The bunching efficiency can be increased by adding higher harmonics [151, 152, 160, 161]. The addition of the second Fourier term in the waveform improves the efficiency by [1]

$$\Delta\tau_s = \chi\frac{\pi^3}{3}\frac{p^3}{\omega}(1+8A) - 4A\chi\pi\frac{p}{\omega}, \tag{30}$$

where A is the relative amplitude of the second harmonic.

Another way of improving the efficiency is by overbunching the beam. In this case, the spherical aberration becomes [132]

$$\Delta\tau_s \approx \chi\frac{2\pi^3}{9\sqrt{3}}\frac{p^3}{\omega} \approx 4\chi\frac{p^3}{\omega}. \tag{31}$$

However, from the viewpoint of data analysis, overbunching can be undesirable, since it complicates the expression for the pulse shape (see Publ. II). This is essentially because in the overbunched case, the expression in Eq. (26) for $T(t)$ becomes only piecewise invertible, with the additional problem of the singularities being transcendental, making the time distribution inconvenient regarding data analysis (see Sec. 3.5).

Another source of time spread are chromatic aberrations [151]. If the initial beam has an energy spread ΔE, then the chromatic aberration of the beam is defined as

$$\Delta\tau_c = \frac{1}{2}\frac{\Delta E}{E_0}\tau_0. \tag{32}$$

Sources of chromatic aberrations include the moderator, gradients in the magnetic field, and geometrical factors in the bunching and acceleration stages. The chopper for instance induces an estimated residual transverse modulation of roughly 10 eV [39]. It is seen in Eq. (32) that the chromatic aberrations can be reduced by increasing the beam

energy. Considering the bunching parameter (Eq. (26)), either the bunching frequency, drift length, or amplitude then have to be increased accordingly.

The final pulsing stage is the main buncher [1], which is a double-gap sinewave buncher similar to the prebuncher but operating at five-fold frequency. It compresses the beam further into pulses around 175–200 ps FWHM. The bunching element is likewise coupled to a low-Q-value (~50) LC resonator to produce a sufficient amplitude. Because the (pre)acceleration stages are DC-floated, the RF lines to the chopper and the main buncher are DC-isolated by series-capacitance coaxial HV “double-DC blocks” [1, 142].

After the pulsing stages, the beam is de-elevated to ground potential by an electrostatic accelerator-decelerator [162]. The two-stage design has two purposes, firstly to extract particles that are backscattered from the sample, away from the sample and detector, and secondly to reduce the variation in time-of-flight over the implantation energy range. The latter can, however, be compensated by adjusting the lifetime signal time delay, which is especially effortless with the digital signal processing chain. The specimen is situated behind a ∅10 mm aperture in the last decelerator electrode. The sample chamber is deliberately oversized to suppress unwanted signals from backscattered particles.

Currently, however, the original acceleration–deceleration concept is not in use. Instead, at the time of writing, the decelerator is shunted to ground. This modification was made after a long-term instability was observed in the accelerator structures in the original configuration. The in-vacuum voltage divider circuit began to show abnormal behaviour after the first months in operation. The electrical resistance began to collapse occasionally depending on the voltage and magnetic field strength. A visual inspection revealed metallic sputtering marks and traces of breakthrough on the accelerator structures, i.e., the POM insulators and stainless steel electrodes, shown in Figure 16.

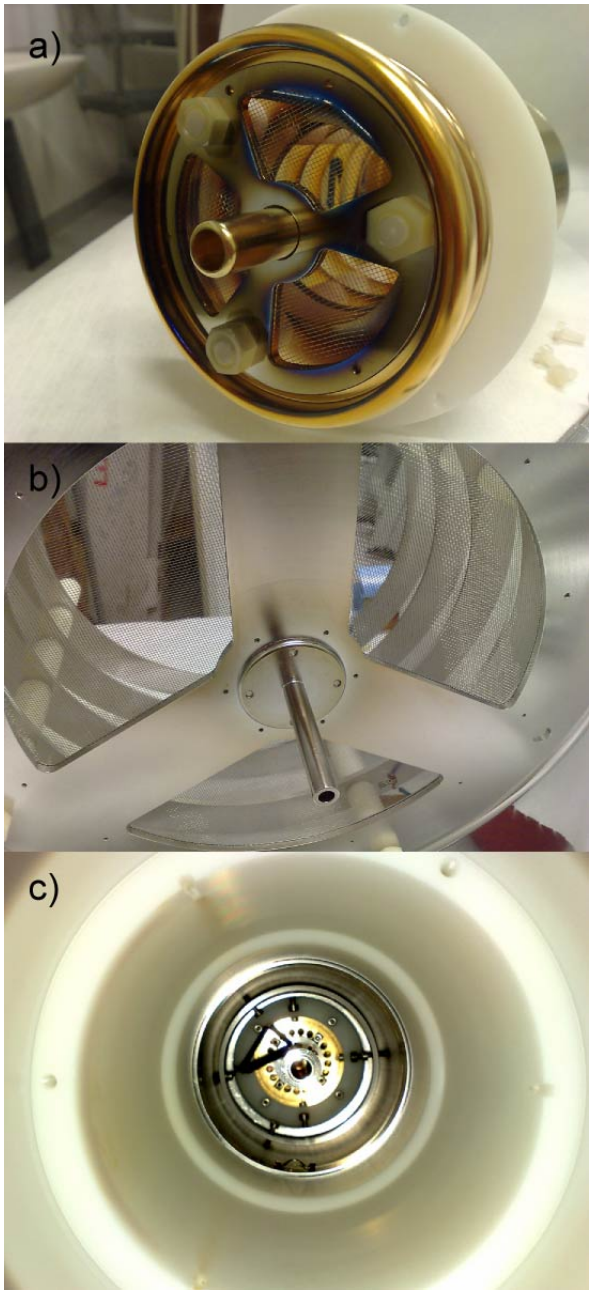

Figure 16. Traces of breakdown found on the main accelerator after long-term use. a) Accelerator (blue discolouration), b) decelerator (darkening around centre), and c) POM vacuum feedthrough housing the accelerator (brown burn marks on inner surface, top and bottom of picture). The marks suggest metal ion sputtering and resulting electrical breakdown due to conductive channels forming on the POM surface.

It was interpreted that the high electric-field strength between the final accelerator electrode/first accelerator electrode and the chamber wall generated field-emission electrons and ions that sputtered the insulator surface, thereby forming conducting surface channels. These two electrodes are both at the lowest (most negative) potential

with respect to ground, and also physically closest to the wall of the grounded target chamber. It was concluded that the HV withstand tests performed on the accelerator prior to its installation had been incomplete, since the effect of the magnetic field was underestimated. The field alters the trajectories of the field-emission particles, and it was also observed by adjusting the coil currents that the breakdown strength depended on the magnetic field strength.

The problem currently awaits further work. It was thus circumvented by grounding the entire decelerator, which in turn grounds the final accelerator electrode. In the present configuration, the decelerator, roughly 0.5 m in length, is electric-field-free, so backscattering effects are still small.

The pulsing system is driven with a common 166.7 MHz crystal oscillator. The signals are tuned with adjustable 180° phase shifters and biphase variable attenuators [158, 163–165], and then amplified by high-power RF amps (Mini-Circuits ZHL-5W-1 and LZY-1) (see Figure 17 for the RF circuit). The inputs of the pulsing elements are matched to 50 Ω using stub elements and attenuators. A fibre-optic link consisting of two 125 Mbaud transmitter/receivers (Hewlett-Packard HFBR-15X7 and HFBR-25X6) is used to transfer the clock signal from the HV platform to earth. The RF electronics (excluding the power amps) are cased in standard NIM rack modules (Figure 18). Autocalibration of the pulsing system, i.e., seeking the optimum phases and amplitudes for each pulsing element, was considered too formidable a task, so the calibration is performed manually. In practice, it suffices to use, for example, 1 keV energy steps.

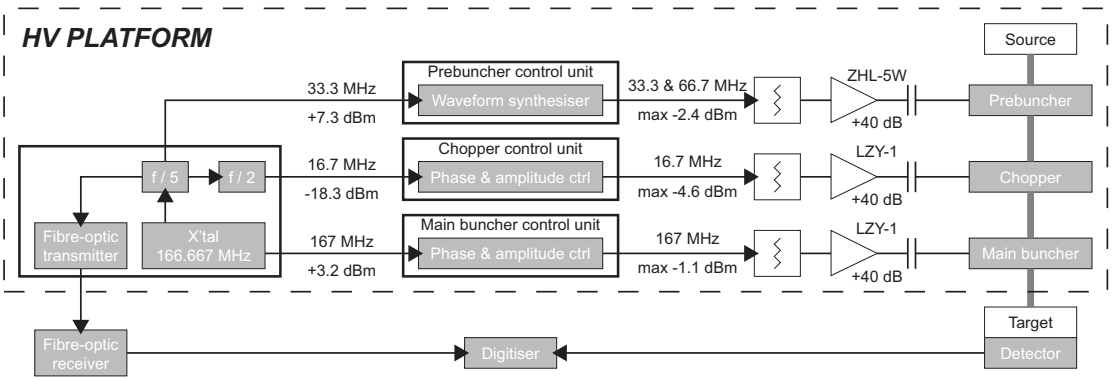

Figure 17. Simplified block diagram of the pulsing system RF circuit. Based on Ref. [158].

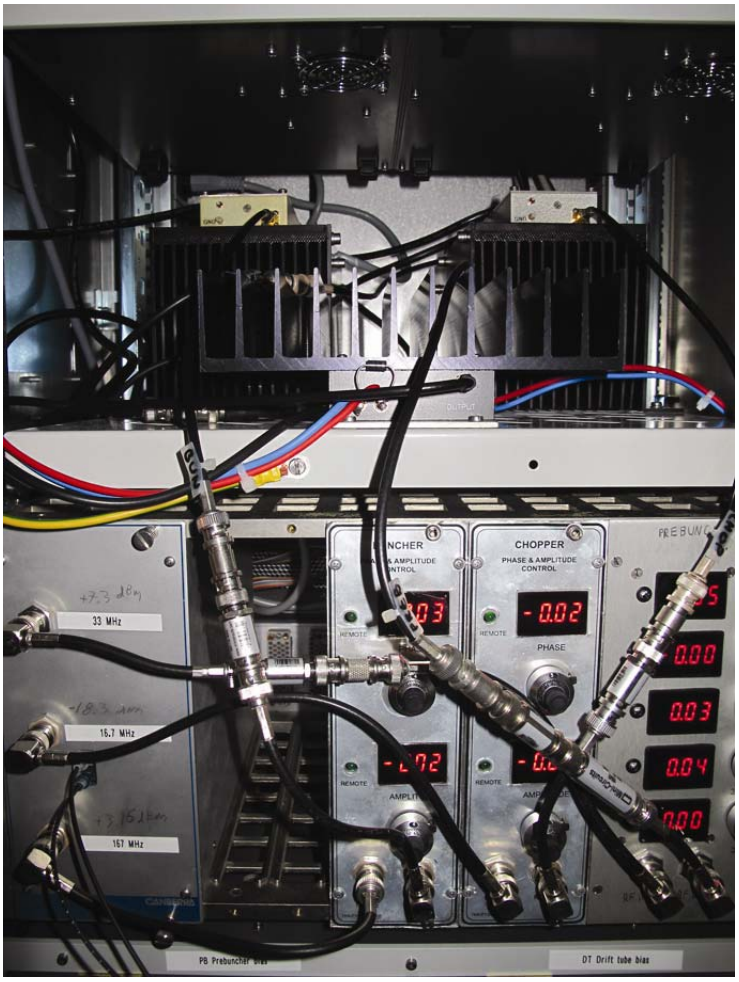

Figure 18. Pulsing system RF electronics in NIM casings (bottom). Also visible are the RF power amplifiers (top).

3.3.3 Performance

A Hamamatsu F4655-12 fast MCP, coupled to a linear transfer stage, is mounted on the target chamber [41]. Because of its good timing properties and insensitivity to gamma radiation, the MCP detector is well suitable for calibration and beam diagnosis. Also, the positron source can be replaced with a thermionic emitter by simple polarity reversal. An electron gun with a BaO disc cathode (Kimball Physics ES-015) is used for this purpose. The choice of cathode is based on its narrow emission energy and small area (∅0.84 mm). Both qualities guarantee a low initial phase-space volume by minimising chromatic aberrations in the electron beam. [143]

The throughput of the beam line in DC mode was measured to be about 90% for the electron beam. This was determined by a simultaneous measurement of the electron

emission and target absorption currents. A phosphor screen was also used in aligning to observe the beam spot visually. The pulsing causes a loss between 65–85%, depending on the tuning.

Figure 19 shows the time distribution of the beam after each of the pulsing stages separately, as measured with the MCP. The performance of the prebuncher is considerably worse compared to the main buncher, as can be clearly seen in Figure 19, and cannot be attributed to the lower fundamental frequency alone. A possible reason is the larger relative energy width of the beam (cf. Eq. (32)). While this limits the bunching efficiency, it has not been observed to deteriorate the overall time resolution significantly, which would be a more severe drawback.

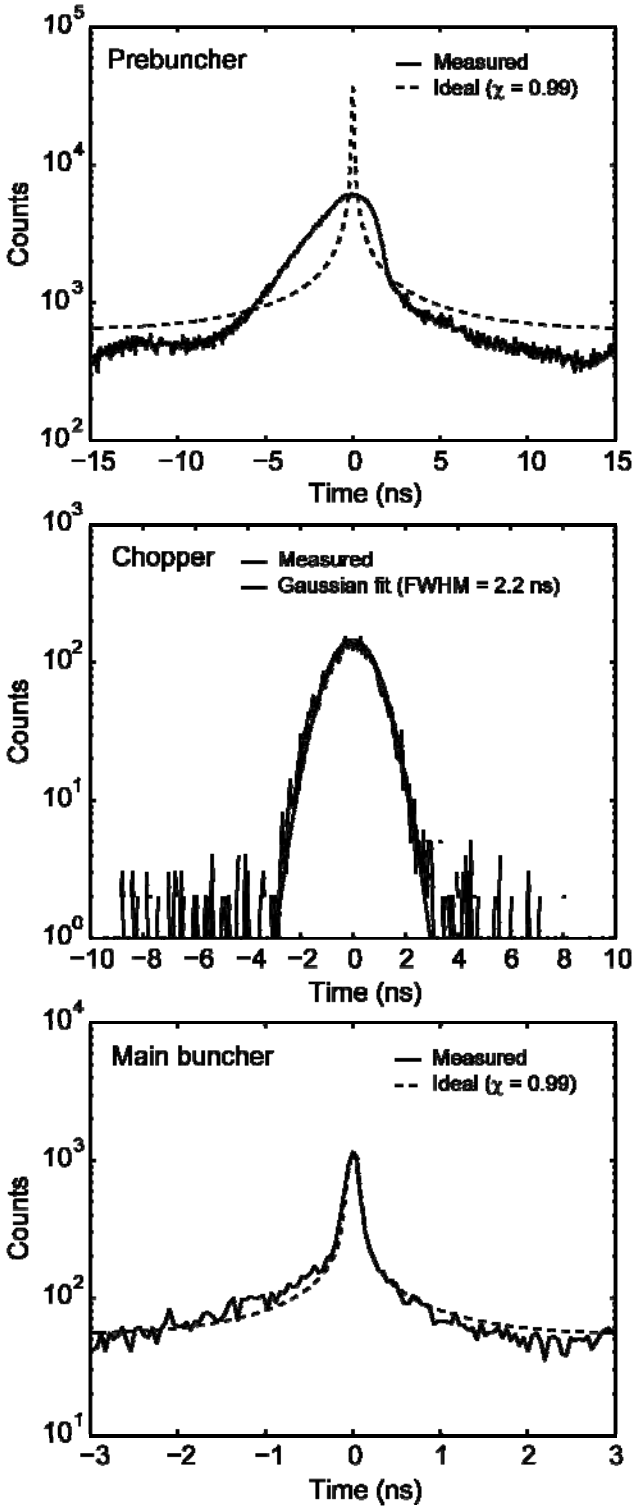

Figure 19. The time structure of the beam induced by each pulsing stage separately. Note the different time scales. The theoretical time-distributions are shown in the almost-critically bunched case, since the critical case ($\chi = 1$) results in a singularity at $t = 0$.

An example of the final pulse shape is shown in Figure 20. Its form is discussed in more detail in Sec. 3.5. A slightly narrower (by ~10 ps FWHM) pulse was obtained with the electron beam, evidently due to the narrower phase-space volume of the electron source. The signal-to-noise ratio is more than 1000:1. The asymmetry of the pulse is partly due to imprecise calibration—the chopper phase is slightly mismatched to the main buncher. While the FWHM varies between 175–200 ps depending on energy, the pulse has rather broad "wings", and is accompanied by small satellite pulses 6 ns away on both sides. These are in magnitude about 1:1000 of the main pulse, and result from leakage through the chopper into the preceding and succeeding cycles of the five-fold frequency main buncher (cf. Figure 19). Due to the finite time-of-flight from the main buncher to the target, the "time zero" shifts with energy, being most sensitive at low energies due to the $\sqrt{E}$ -dependence of the flight time.

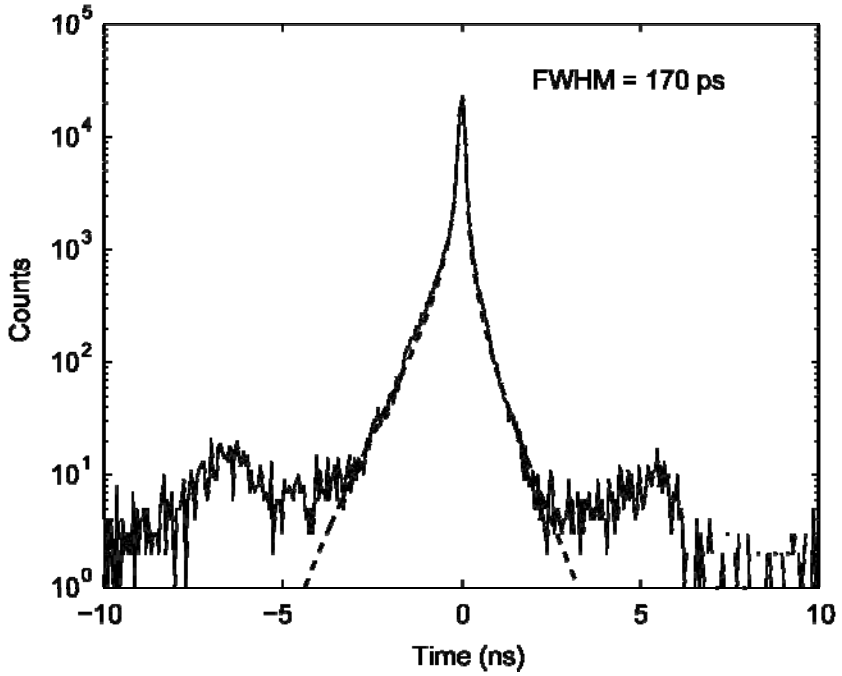

Figure 20. The time structure of the positron pulse, measured at 2 keV with the MCP. The dashed line is a (non-optimal) fit based on the ideal time structure (see 3.5.1). The satellite bunches are due to leakage from the chopper—ideally, the beam would be fully suppressed during the remaining four cycles of the five-fold frequency main buncher. The asymmetry is due to improper phase-matching of the chopper; the chopper acceptance time window is slightly misaligned with the main buncher pulse. Based on Publ. II.

The broadness of the wings is proportional to the chopper time-window, which in turn, however, is proportional to the bunching efficiency, and hence also to the event rate. Thus, there is a trade off between time resolution and collection time, and in fact, also signal-to-noise ratio. Specifically, the laboratory background radiation causes a constant background level in the lifetime spectra, so decrease in event rate also results in

worsened statistics. This follows from the non-coincidence nature of the measurement principle; for each START signal that passes the energy discrimination, whether it originates from an annihilation event or a background radiation photon, a STOP signal from the clock is registered within 30 ns, and the event is included in the spectrum. Hence, the signal-to-noise ratio is directly proportional to the ratio of annihilation event rate and background photon rate. This is different compared to (coincidence) fast-positron spectrometers, where the signal-to-noise ratio is, in the zeroth-order approximation, independent of the background radiation level [166].

The total transversal energy spread introduced by the pulsing stages is estimated to be at most around 0.5 keV, although this remains to be confirmed by experiment. For this purpose, a residual potential analyser can be used. If confirmed, the effect of the spread on depth resolution is marginal, since the positron implantation profile (Eq. (14)) would dominate the resolution already at very low (a few keV) energies.

The time structure was observed to drift with temperature, with the peak drifting 25–30 ps/˚C (in the range ~23–27˚C), in good agreement with estimates from stability tests performed on the RF electronics [163]. The fibre-optic link has a notable drift of 20–30 ps/˚C. The laboratory air-cooling oscillates at roughly 1˚C per day. So far, the long-term drift has been observed to be roughly 100 ps per month.

3.4 Lifetime detection and signal processing

3.4.1 Scintillation detector

A truncated-pyramid (40×40 mm^2 bottom, 25 mm height, 25×25 mm^2 top) barium fluoride (BaF_2) scintillator [167–170], coupled to a Philips/Photonis XP2020Q photomultiplier tube (PMT) (type B' base as per Philips photomultiplier data handbook [171]), is used in detecting the annihilation photons, and is situated in a retractable vacuum well just behind the sample. The overall detection efficiency for annihilation events was determined to be in the range 20–35%. However, some inevitable signal discrimination is required, as discussed in more detail in Sec. 3.4.2, reducing the overall count rate in lifetime measurement to the order of 10^2–10^3 s^{-1}. The detector was evaluated to have a Gaussian response of around 200 ps FWHM.

The PMT requires rather heavy magnetic shielding to suppress the field strength from around 5 mT to an acceptable level of 0.1 mT or less. The shield, placed inside the vacuum well, is made of magnetic alloys (Ad-Vance Magnetics AD-MU-00 & AD-MU-80), with an overall thickness of 7 mm, surrounding the PMT. It composes of two separate layers of cylindrical shielding housings. The outer layer is made of a medium-permeability alloy to coarse-attenuate the field, in order to protect the inner layer from

saturation. The inner layer, in turn, is made of conventional high-permeability material, commonly referred to as mu-metal. The cylinders are open-ended to allow, at the scintillator end, for minimum gamma ray attenuation, and at the other end for the electrical feedthroughs. The shield design was based on finite element simulations [172, 173]. The drop in PMT gain due to the small residual field inside the shield is roughly 8% in signal amplitude at the applied bias (−1.8 kV). It was estimated that the effect in the total FWHM was at most 25 ps.

The Curie points of the shielding alloys have not been confirmed, but are estimated to be around 600°C or higher. This ultimately presents an upper limit to the sample heating temperature, since, as the shield is situated close to the sample holder, some amount of radiant heat is absorbed by the shield. The limit is nevertheless sufficiently high for usual temperature ranges. [174]

3.4.2 Signal processing

To measure the positron lifetime, the timing signals are taken from the detector anode and the 33.3 MHz clock. Due to the high repetition rate, the detector output is used as the triggering START. The signals are fed to a 1-GHz, 8-bit digitiser (Agilent U1071ATM1), sampling both channels at 1 GS/s. The time delay between the signals is determined by applying digital (differential) constant-fraction timing [90]. With the MCP, the hardware configuration is equivalent. The conventional constant-fraction is determined from a smoothing-spline fit to the data samples. Because the signal rise-times are short (PMT: ~2 ns, MCP: ~0.4 ns, clock ECL (emitter-coupled logic): less than 1 ns), in-built 20 MHz low-pass filters are used in the input channels. The filtered signals provide a sufficient number of samples (at least 4) to be taken from the leading edge for fitting without observable loss in timing accuracy [90]. Figure 21 illustrates the effect of the filtering.

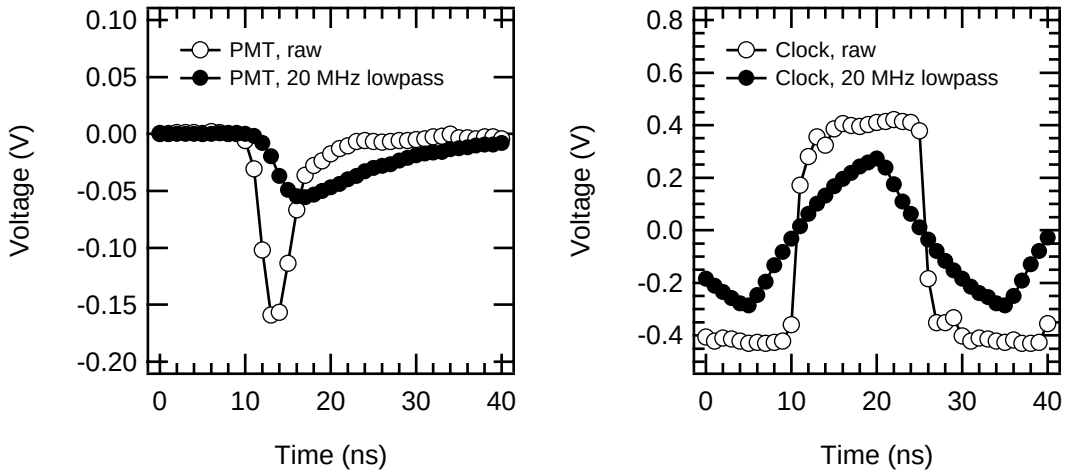

Figure 21. The sampled PMT and clock ECL signals, both raw and 20 MHz low-pass filtered. The filtering increases the signal rise time, so that enough samples can be taken from the leading edges for optimum timing.

BaF_2 has two scintillation decay channels, both in the near-ultraviolet range. The fast component (0.6 ns decay constant), suitable for timing, is only around 10% in branching ratio. The slower channel (600 ns) introduces a long tail to the anode signal, which can cause pileup distortions at high detection rates (see Figure 22). At the present event-rates, however, it is not necessary to pay special attention to pileup effects. Instead, the slow component affects signal-height discrimination, in such that the signal peak value becomes a statistically notably worse measure of energy than the time integral, i.e., the charge. Because the laboratory background radiation increases the false-event rate linearly, it is necessary, due the 1/*f*-nature of the background, to choose the acceptance energy window only around the 511 keV line (photopeak), since this maximises the events-per-background ratio. Figure 23 illustrates the situation. For this purpose, optimum energy resolution is beneficiary. The γ energy is thus in this case determined from the time integral (sample sum) over the signal, in principle as in analogue charge-sensitive preamplifiers. In practice, it suffices to take only, for example, 200 ns (200 samples) to the right of the leading edge, so that the computation time does not become a limiting factor. Compared to taking the signal peak-value as energy measure, the improvement in signal-to-noise (events per background) ratio in lifetime spectra is around a factor of 4/3 in, e.g., silicon.

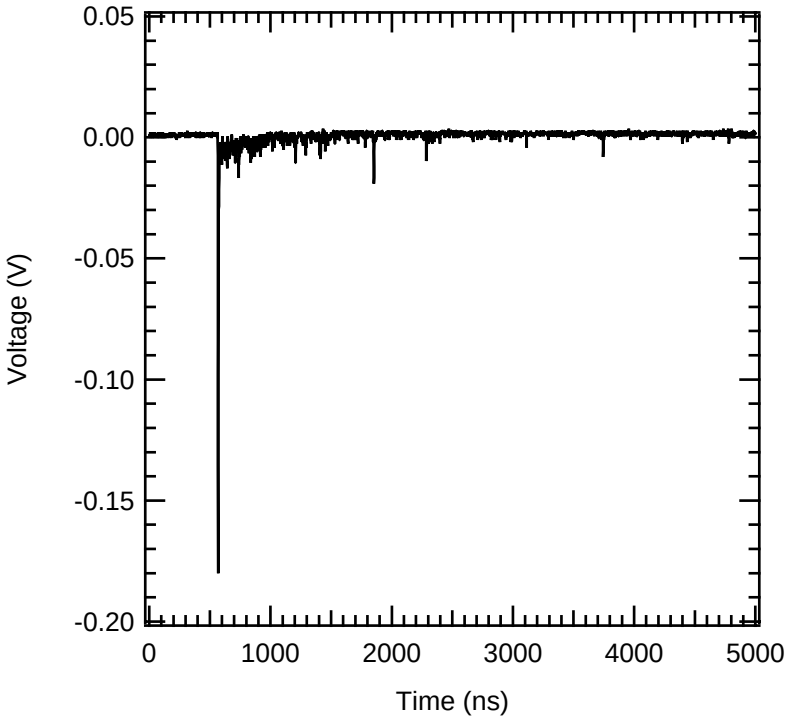

Figure 22. The sampled PMT anode signal. The trail is due to the long (600 ns) decay channel of BaF_2.

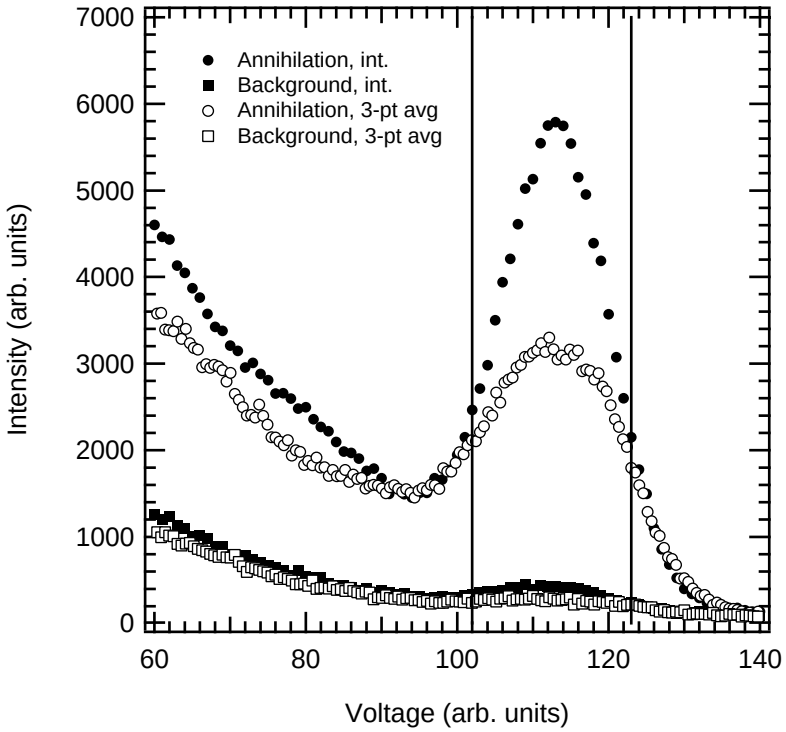

Figure 23. Radiation energy histograms of annihilation events including laboratory background, and plain background, determined from the BaF_2 scintillation detector signals by signal-peak three-point average, and by summation (time integral) 200 samples (200 ns) over the peak. The peak in the energy histogram is the 511 keV annihilation photopeak, and to its left is the Compton continuum. Due to the high-intensity slow scintillation channel in BaF_2, the signal peak value is a worse measure of photon energy; the photopeak is enhanced when integrating the PMT anode signals. The solid lines indicate the energy discrimination lower and upper levels that more or less maximise the signal-to-noise ratio in lifetime spectra.

In place of the digital setup, analogue NIM electronics could easily also be used. In that case, the timing signals would be fed to a conventional set of constant fraction timing discriminators, time-to-amplitude converter, and multichannel board. A fast-slow configuration using a charge-sensitive preamplifier would be preferable over fast-fast due to the energy discrimination described above.

3.5 Data analysis

3.5.1 Instrument function

As discussed in Sec. 2.4.3, lifetime data analysis is more difficult and error prone with slow positrons due to the inclusion of surface and interface effects. If the material layer in question is inhomogeneous, for example, in trapping-defect distribution, the situation is worsened still. Unfortunately, the beam bunching itself introduces another set of parameters that affect the pulse shape and thereby also the instrument resolution function. In bulk studies, the variations in scintillation photon and PMT electron transit-time together with the electronic resolution are represented by a single Gaussian to model the detector response. In this case, however, the non-trivial positron pulse shape also needs to be accounted for. In Ref. [1] and Publ. II, the shape of the positron pulse is analysed. An expression for the final pulse shape is derived. However, even excluding the effect of bunch aberrations, the closed-form expression of the overall instrument function, described below, is not known, so it must be computed numerically. Some common fitting programs offer the possibility to use a set of weighted Gaussians to describe the instrument function, yet experiences in this approach indicate that it generally does not reduce the required number of fitting parameters.

Considering a single-frequency beam buncher, the particle arrival-time distribution at the time focus is, by Eq. (26), denoting $g(t) \equiv T(t)$ and setting without loss of generality $\tau_0 = 0$, given by

$$(f_T \circ g)(t) \equiv f_T(g(t)) = \frac{\omega}{2\pi} \frac{1}{1 - \chi \cos(\omega t)}, \quad t \in [-\pi/\omega, \pi/\omega). \tag{33}$$

Neglecting for simplicity the second harmonic of the prebuncher, Eq. (33) applies to both the prebuncher and the main buncher. We shall denote the prebuncher and main buncher angular frequencies with ω_1 and ω_2, respectively, and similarly, their bunching parameters with χ_1 and χ_2. Apart from the scattering artefacts, the chopper acceptance-time window is very close to Gaussian. Let its standard deviation, determined by the chopping waveform amplitude, be σ_c, and its phase/time offset with respect to the prebuncher pulse, determined by the chopper waveform phase, μ_c. Using the fact that the flight time from the chopper to the main buncher is short, and therefore the time structure of the prebunched and chopped beam does not change significantly before reaching the main buncher, and modelling the response of the detector chain with a Gaussian, it can be shown that the instrument function is, short of a normalisation factor,

$$f_{\mathrm{r}}(t)=\frac{\omega_1}{2\pi}\int_{-\pi/\omega_1}^{\pi/\omega_1}\exp\left(-\frac{\left(g_1(t')-\mu_{\mathrm{c}}\right)^2}{2\sigma_{\mathrm{c}}^2}\right)f_{\mathrm{d}}\left(t-g_2\left(g_1(t')\right)\right)\mathrm{d}t', \tag{34}$$

where f_{d} is the detector response and the functions g_1 and g_2 are defined as in Eq. (33) with the addition of the main-buncher phase-mismatch φ with respect to the prebunched pulse,

$$\begin{aligned} g_1(t)&=t-\frac{\chi_1}{\omega_1}\sin(\omega_1 t),\\ g_2(t)&=t-\frac{\chi_2}{\omega_2}\sin(\omega_2 t+\varphi), \quad t\in\left[-\pi/\omega_1,\pi/\omega_1\right). \end{aligned} \tag{35}$$

Using a Gaussian for the detector response, Eq. (34) reproduces the actual instrument function fairly well, less the aforementioned aberrations (see Figure 20 and Publ. II). Hence, with the inclusion of the standard deviation of the detector response, the instrument function depends on a total of six variable parameters ($\chi_1, \chi_2, \varphi, \mu_{\mathrm{c}}, \sigma_{\mathrm{c}}, \sigma_{\mathrm{d}}$), as opposed to just the detector parameter σ_{d}. Since only the flight time from the main buncher onwards depends on the implantation energy, only one parameter, the main buncher parameter χ_2, is varied with energy. An additional variable, also present in bulk studies, is the lifetime spectrum time-offset, determined by the delay between the START and STOP signals.

Fortunately, the values of the parameters can be roughly determined a priori by examining the time structures produced by the pulsing stages individually. In addition, with the fast MCP, the pulse shape can be determined within the limits of the MCP time jitter. The time response of the MCP is not known precisely, but is estimated to be around 100 ps FWHM or less.

3.5.2 Data fitting

The natural approach in data fitting is to first determine the resolution function using some well-known calibration sample. This needs to be performed separately for each energy step. Due to drift, it is advisable to include the calibration sample in each measurement run. At present, however, such samples are scarce, since as discussed in Sec. 1, slow-positron lifetime has remained an uncommon technique to date. Also, the spectrum artefacts, namely in this case the satellite peaks and the non-constant background, disturb the data analysis. The simplest solution is to neglect in the fitting procedure the regions of the experimental spectrum where these artefacts appear.

A Matlab-based program for fitting the lifetime data is currently under development [81]. The program solves the diffusion equation (Eq. (21)) numerically using a 'backward in time, centred in space' finite difference method. It then computes the instrument response (Eq. (34)) using a Gaussian as the detector response f_d, and convolves this with the computed lifetime spectrum (Eq. (19)). The routine uses a trust-region fitting algorithm. This has the benefit of allowing limiting the search regions of the parameters. The free parameters are selectable. For analysing depth scans, the program needs to be capable of fitting multiple spectra, i.e., the entire implantation energy range, simultaneously. As mentioned in Sec. 2.4.3, deep in the material layer, i.e., for high implantation energies, one can approximate the lifetime distribution with the conventional sum-of-exponentials form of Eq. (9). This can be used as a complementary method in the analysis, since many commonly used fitting programs are based on this approach. Since the software was still under development during the time of writing of this thesis, the following data fitting has been done this way using the PALSfit program.

p-type silicon is used as an example. For comparison, the sample was also characterised with the Pulsed Low-Energy Positron System (PLEPS) at NEPOMUC at Forschungs-Neutronenquelle Heinz Maier-Leibnitz (FRM II), Technische Universität München, Germany, which is a similar instrument. The PLEPS lifetime spectra were decomposed using two-component exponential fits. The data decomposition was done with in-house software (POSWIN 2.x) of Institut für Angewandte Physik und Messtechnik, Universität der Bundeswehr München, Germany [175]. The second lifetime was kept constant at τ_2 = 387 ps, which is a typical value for the positron surface-state [134, 176]. The resulted decompositions are illustrated in Figure 24. For increasing implantation depths, the first lifetime component τ_1 approaches the well-established bulk lifetime in Si of 220 ps with increasing intensity I_1. The slow convergence of the intensity is due to the long diffusion length in crystalline Si [87, 135, 177].

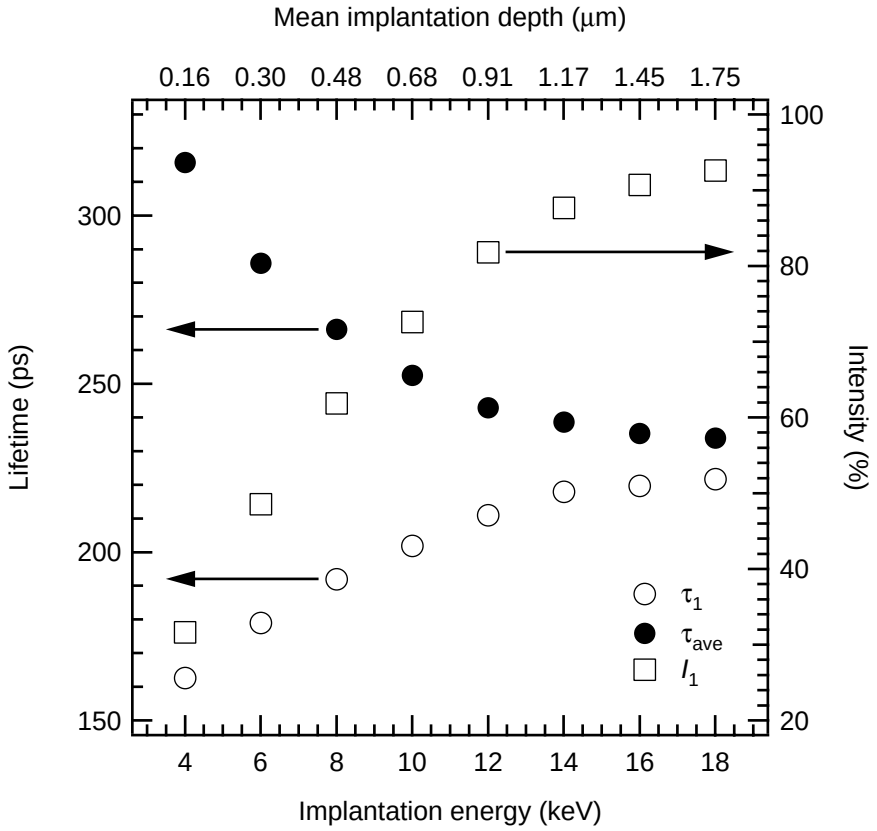

Figure 24. Results from lifetime spectra in p-type Si measured with PLEPS. The spectra were decomposed with two-component exponential fits keeping the second lifetime component fixed at 387 ps representing the positron surface state.

Figure 25 shows as an example lifetime spectra measured with the Aalto University pulsed beam with low (4 keV) and high (18 keV) implantation energies. The constant laboratory background has been subtracted in order to reveal the shape of the resolution function and the background structure caused by the pulsing system. By comparing the two spectra, it can immediately be seen that the average positron lifetime is longer with 4 keV, i.e., closer to the surface of the sample, as expected due to surface states.

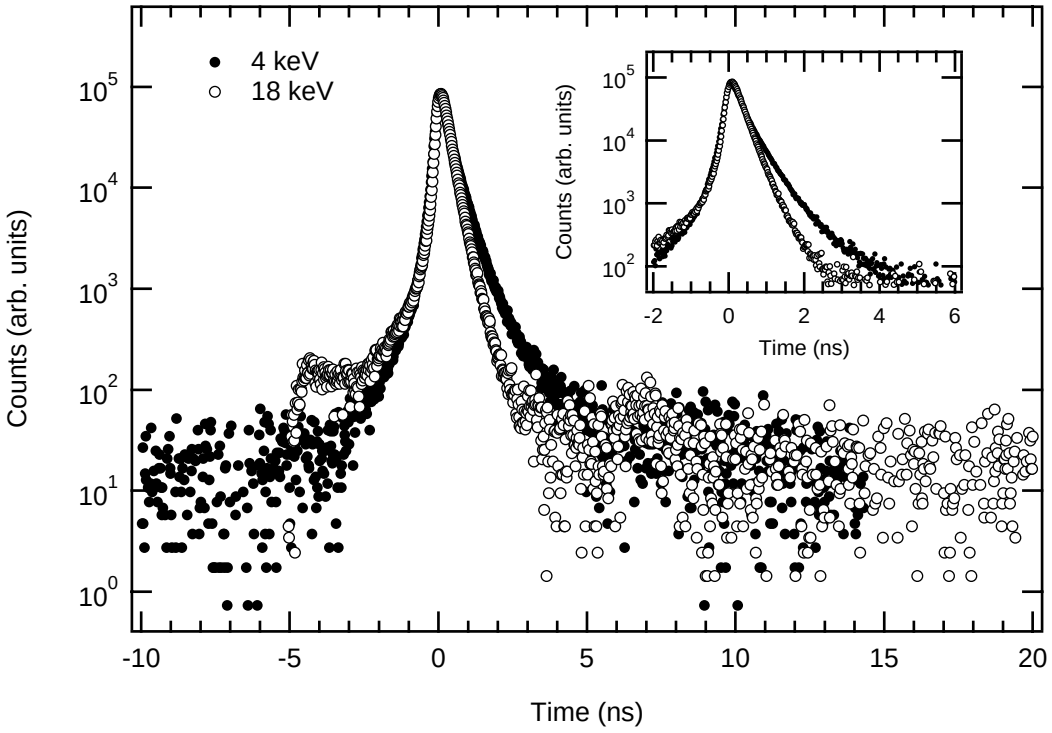

Figure 25. Examples of lifetime spectra in silicon measured with the pulsed beam.

Fixing the lifetimes and intensities obtained with PLEPS, we first attempt to model the resolution function with a conventional sum-of-Gaussians. Figure 26 shows the reduced-χ^2 statistics of the fits, and Figure 27 shows as an example one of the fits. The weights of the Gaussians were kept constant at 2:1:1 and 1:1:1:1 in the three- and four-Gaussian fits, respectively. For comparison, those of the PLEPS data fits are included. We find that statistically, a sum of three Gaussian distributions is adequate to model the resolution. However, it should be noted that the decompositions of the spectra from PLEPS are somewhat poor to begin with. This is likely due to the improper calibration of the PLEPS pulsing system.

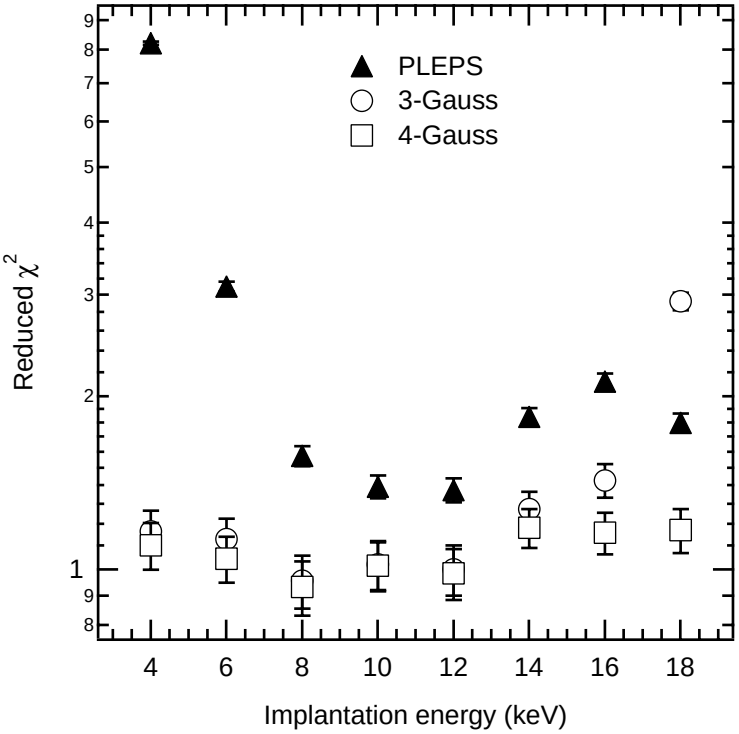

Figure 26. Reduced-χ^2 values of fits to lifetime spectra obtained from the silicon sample.

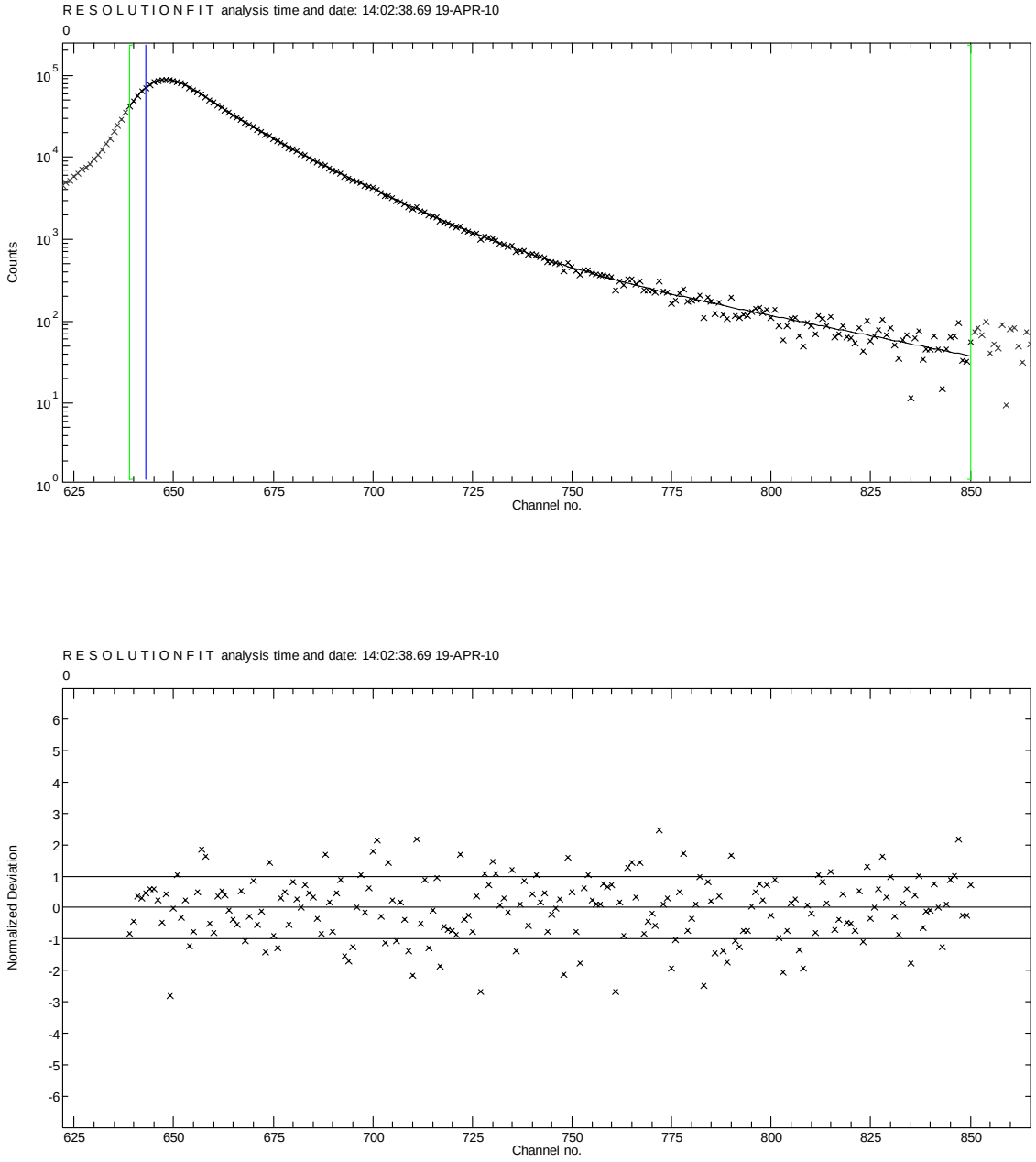

Figure 27. Example of fit to lifetime spectrum using three Gaussians in modelling the instrument resolution. The implantation energy was 10 keV. The residual plot (below) shows no patterns, indicating that the model is appropriate.

However, if even the two lifetime components are left free in the fits, thus simultaneously fitting the resolution function and the lifetime spectrum, we arrive at a different result (Figure 28). The number of free parameters is now very large, but the

resulting lifetimes are nevertheless credible. The first component τ_1 converges towards around 235 ps with increasing intensity towards higher implantation energies. However, the intensity scale of I_1 is quite different than in the previous. Also, the second component is much longer, around 900 ps. The average lifetime, τ_{ave}, is about 20 ps longer than with PLEPS at nearly all energies.

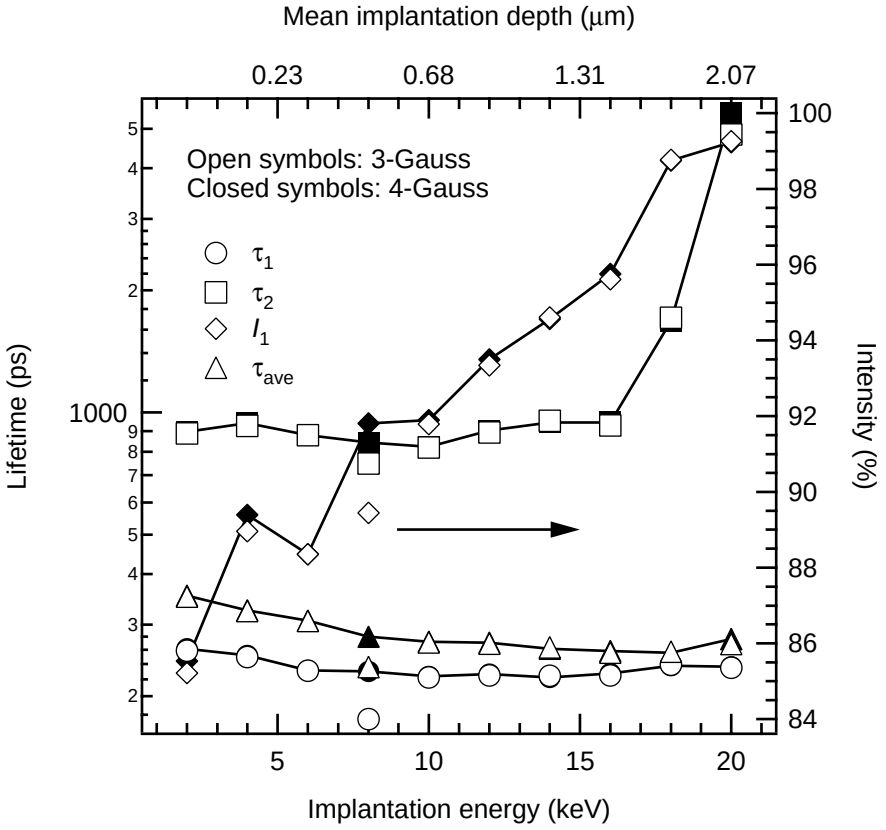

Figure 28. Results of the free two-component decomposition. The divergence of the second lifetime component τ_2 at the highest implantation energies is likely a fitting artefact due to the vanishing intensity I_2.

Since both lifetimes were longer than expected, also a three-component fit was performed. However, the second lifetime was fixed at $\tau_2 = 380$ ps to represent the surface state, since otherwise the number of free parameters became too large. The resolution function was fitted with three Gaussians in this case. The results are shown in Figure 29. Now τ_1 approaches $\tau_{Si} = 220$ ps, while its intensity I_1 increases from 25% at 2 keV to 80% at 20 keV. There is a diminishing third lifetime of roughly 1.1 ns, which begins to diverge heavily at high energies when its intensity drops to less than a couple of %. This may be an instrument artefact at least at the highest energies, but its otherwise more or less constant value and decrease in intensity with increasing implantation energy suggests that it could be associated to surface Ps [87, 177].

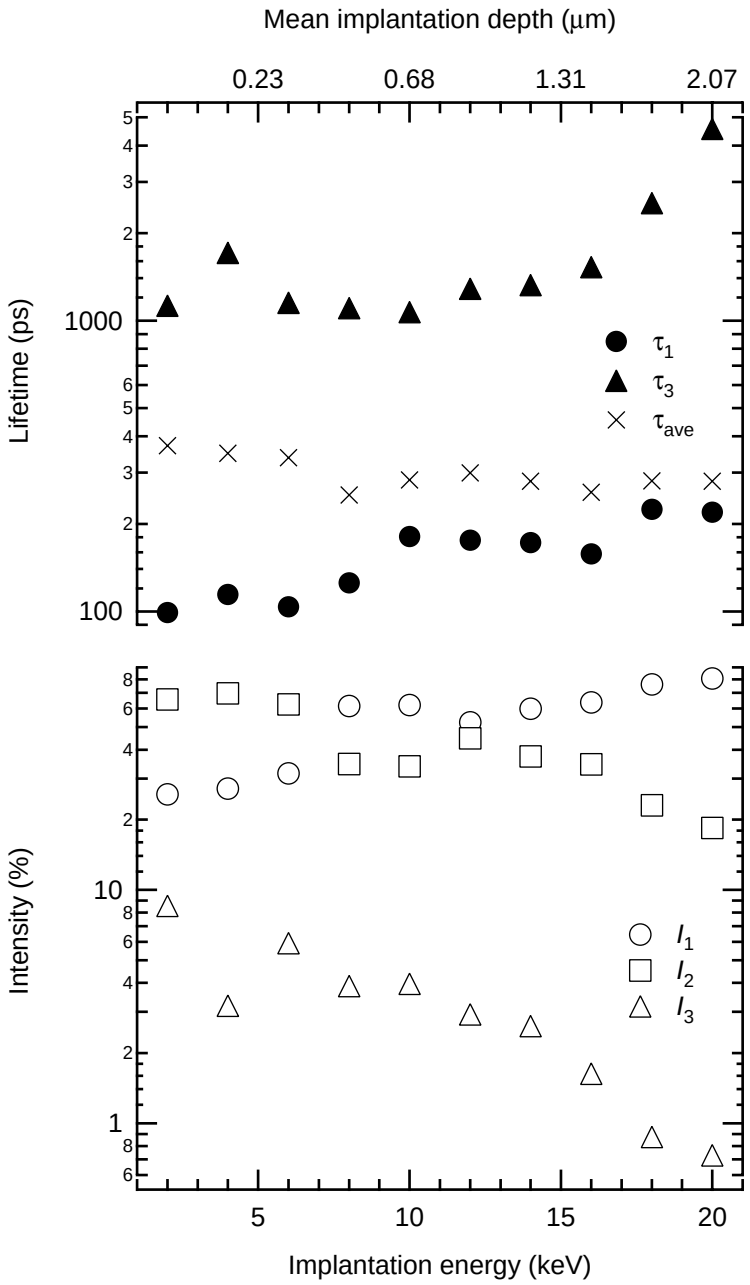

Figure 29. Results of the three-component decomposition keeping τ_2 fixed at 380 ps.

Finally, although the sum-of-Gaussians model for the resolution function is demonstrated to produce statistically good fits to lifetime data, it is in actuality quite poor for reproducing the pulse shape (Figure 20). It was observed that three or even four Gaussians is insufficient to obtain good fits to the pulse shape. The goodness of the lifetime fits above owes partly to the large total number of free parameters, and partly to the "smoothing out" of the resolution function in the convolution. It should be noted that with a single-Gaussian resolution function, as in fast-positron spectrometers, the "slopes" (on a semilogarithmic scale) of a spectrum of the form of Eq. (9) do not

change, but in general, this does not hold for a more complex resolution function. Also, the number of free parameters is by no means smaller than with Eq. (34); while the first Gaussian component is defined by its standard deviation alone, additional components introduce three more parameters each, namely standard deviation, relative intensity (weight), and offset/shift. Thereby, the use of three Gaussian components already introduces more parameters (seven) than when using Eq. (34).

3.6 Concluding remarks

The relative complexity of the HV design is rewarded by ease in sample manipulation, since the sample is not floated during measurements. For example sample motion, biasing, heating, and cooling are greatly facilitated. A future task is to include sample illumination, which could additionally be time-synchronised with the beam to enable transient studies.

Because of the asymmetry of the beam chopper, the chopper time-window is slightly different (not shown) between the two zero-crossings of the waveform. This is a minor disadvantage of the chopper design, although its effect on data analysis is buried by statistical uncertainties. A more severe problem is the leakage, which induces the satellite pulses 6 ns away from the main pulse. The background from the chopper is also non-constant, causing further complications in data analysis. Although the pulse shape can be somewhat improved by increasing the chopping amplitude, the benefit is counterbalanced by increased collection time and worsened statistics.

Regarding bunching efficiency, it is under consideration to replace the present two-harmonic prebuncher waveform synthesiser with an arbitrary waveform generator. The present limit of roughly 20 mCi minimum source activity could also easily be reduced with an improved moderator, which would additionally benefit the data collection time. The count rate could safely be increased by at least one order of magnitude before detector pile-up effects begin to require attention. However, despite several attempts to improve the efficiency using several W foils and heat-treatments, the efficiency is more than an order of magnitude less than values reported in the literature, see, e.g., Refs. [30, 100, 103, 178]. A promising candidate for improving the efficiency is the semiconductor field-assisted moderator [86].

It should be mentioned that shielding the scintillator from background would not improve the counting statistics in significant amounts. Simply due to geometric constraints even the theoretical maximum solid angle spanned by the shield could only be 2π, so the reduction in background would be limited to at most a factor of two. Even then, significant changes would need to be made to the design.

As a final note, in conclusion to all the issues discussed related to the analysis of measurement data, it should be stressed that data analysis with a slow-positron lifetime beam is hardly straightforward. This is partly due to the complex and limited resolution of the instrument, and partly to the larger variety of positron-related phenomena that occur in layered materials compared to bulk. On the contrary, data analysis requires sophistication, experience and often much insight from the user. Otherwise, there is a risk of false interpretations.

4 Vacancy-defect studies in indium nitride

4.1 Background

Indium nitride has gained attention in semiconductor science with much potential in optoelectronic, high-power and high-speed electronics, and photovoltaic applications [52, 55, 57]. The (direct) band gap, now estimated around 0.7 eV, is in the infrared region [42, 44, 46, 49, 50, 54, 59, 60]. Together with the other III–nitrides, GaN (3.4 eV [179]) and AlN (6.2 eV [180]), the III–N ternary alloys cover the solar spectrum from near-infrared to deep ultraviolet. Bulk InN is not yet available, but high quality films can be grown by molecular beam epitaxy (MBE) [181–185] and metal-organic chemical vapour deposition (MOCVD) [186–188].

The electrical and optical properties of the material are under intense research. The effective electron-mass in InN is very small [53, 59], and high electron mobilities and peak velocities have been achieved [43, 45, 51, 56, 58]. The material has also displayed high resistance to radiation damage, having prospects in space applications [61]. So far, InN has suffered from a strong propensity for *n*-type conductivity, however, *p*-type films have recently been reported [47]. Although much progress has been made in growth, one problem is the lack of well-suited substrates. The lattice mismatch between the commonly used sapphire (Al_2O_3) is large, necessitating the use of buffer layers such as GaN [189].

The crystal quality has been found to depend on the film thickness strongly in the sub-micron region [1, 190–193]. On the other hand, growth stoichiometry has been observed to have little effect on indium vacancy (V_{In}) formation in MOCVD-grown films [194]. In Sec. 4.2 and Publs. III & IV, the role of growth conditions, such as stoichiometry, temperature, substrate, polarity, and dislocation density on V_{In} formation in InN grown by plasma-assisted molecular beam epitaxy (PAMBE), investigated using slow-positron Doppler broadening, is discussed.

According to the amphoteric defect model (ADM) [195], the reason for the strong tendency for *n*-type conductivity of unintentionally doped InN lies in the position of the conduction band minimum relative to a Fermi stabilisation energy, E_{FS}. In the ADM, the Fermi stabilisation level is an intrinsic property of the material, i.e., it is insensitive to the band edges and thus also to the doping level, that originates from the localised nature of intrinsic point defects. Native defects can behave amphoterically, in that they can act as donors or acceptors. The nature (donor or acceptor) is determined by the Fermi level E_F with respect to E_{FS}. When E_F is below (above) E_{FS}, the defects tend to be *n*(*p*)-type, pulling the Fermi level up (down), until it pins to E_{FS}. In InN, the Fermi stabilisation level lies high in the conduction band (0.9 eV above the conduction band

minimum [61, 196]), so that in undoped material, intrinsic defects act predominantly as donors. [57]

Nevertheless, the dominant donors in unintentionally doped InN remain unidentified. Candidates so far include native nitrogen vacancies, interstitials, and antisites [197, 198], indium-related defects [199, 200], and unintentional impurities such as oxygen, silicon, and hydrogen [181, 201–206]. Threading dislocations have also been suggested, although their role is disputed—however, there is much evidence supporting the view that threading dislocations are the dominant scattering centres limiting the electron mobility in undoped InN [205, 207–212].

It has previously been found that high-energy particle irradiation provides a controllable way to increase the free-electron concentration in undoped InN by introducing donor defects [196, 213, 214]. The electron mobility drops in the irradiation, but was discovered to be nearly fully restored by subsequent rapid thermal annealing (RTA), while the carrier concentrations remained nearly unaltered [215]. This was ascribed to the partial recovery and spatial reordering of triply charged defects in the annealing.

The effects of He irradiation and subsequent rapid thermal annealing on point defects in MBE-grown InN are presented in Sec. 4.3 and Publs. V & VI. For this purpose, slow-positron lifetime was utilised using the PLEPS setup, since at the time, the Aalto University pulsed positron beam was still under construction. Results on Doppler-broadening experiments performed on the as-irradiated samples have been published in Ref. [216]. It was found that V_{In} were produced in the irradiation at a much lower rate (100 cm^{-1}) than V_{Ga} (3600 cm^{-1}) in similarly irradiated GaN grown by MOCVD. Also, the V_{In} concentration was seen to saturate in the mid-10^{17} cm^{-3} range when the irradiation fluence exceeded $\phi = 2\times10^{15}$ cm^{-2}. On the other hand, also intrinsic negative-ion type defects were observed to be produced in the InN films, at a much higher rate of 2000 cm^{-1}. These were tentatively ascribed to N interstitials, which possibly act as important compensating centres ultimately limiting the *n*-type conductivity in the films.

4.2 Effects of growth conditions on indium-vacancy formation in InN grown by plasma-assisted molecular beam epitaxy

Slow-positron Doppler-broadening was applied to study vacancy formation in a set of different InN layers grown by PAMBE. The In-polar layers were grown either directly on a semi-insulating GaN template or using a MBE-GaN buffer layer. The growth temperatures were between 430°C to 470°C. The N polar layers, in turn, were grown at 550°C on MBE-GaN grown on *c*-face SiC or N-polar freestanding GaN. The electron concentrations in the samples varied from low-10^{17} cm^{-3} to low-10^{18} cm^{-3}, and the carrier mobility ranged from 2000 to 800 cm^2/Vs, as determined by single-field Hall measurements. The samples are labelled In(x) or N(x) for In- and N-polar growth,

respectively, with x giving the growth regime In (In-droplets), s (stoichiometric) or N (N-rich), and are described in Table 1. More details on the growth procedures and electrical characterisation can be found in Refs. [181, 182].

Table 1. Description of the PAMBE-InN samples and V_{In} concentrations determined in this work.

Sample	Growth temp. (°C)	Thickness (nm)	Template	$[V_{In}]$ (10^{16} cm^{-3})
In(In)-1	430	980	MBE-GaN	2
In(In)-2	450	250	MOCVD-GaN	6
In(In)-3	450	750	MOCVD-GaN	3
In(In)-4	470	1000	MBE-GaN	2
In(N)-1	430	830	MBE-GaN	< 1
In(N)-2	450	300	MOCVD-GaN	5
In(N)-3	450	1400	MOCVD-GaN	5
N(In)	550	1000	GaN / free-st. GaN	5
N(s)-1	550	500	GaN / SiC	3
N(s)-2	550	2000	GaN / SiC	4
N(N)	550	1000	GaN / SiC	7

Figure 30 shows the *S* parameter measured as a function of positron implantation energy in selected InN layers. When positrons are implanted close to the sample surface, in the energy range of 0–1 keV, an *S* parameter of $S = 0.490–0.495$ is recorded in all the samples. These values characterise the defects and chemical nature of the near-surface region of the samples (~0–5 nm). The region where *S* is constant can be taken as characteristic of the InN layer, illustrated by the dotted line in Figure 30. The plateau of constant *S* varies from sample to sample due to the different thicknesses of the layers, and extends from a few keV to 7 keV in the 250-nm-thick sample and up to 20 keV in the thicker samples. The decrease of the *S* parameter at higher implantation energies in

the In-polar samples is due to the increasing fraction of positrons annihilating in the GaN template/buffer layer, for which the characteristic S parameter is roughly $S = 0.46$, while the increase at high energies in the N-polar sample is due to the slightly higher S parameter of SiC ($S = 0.485$).

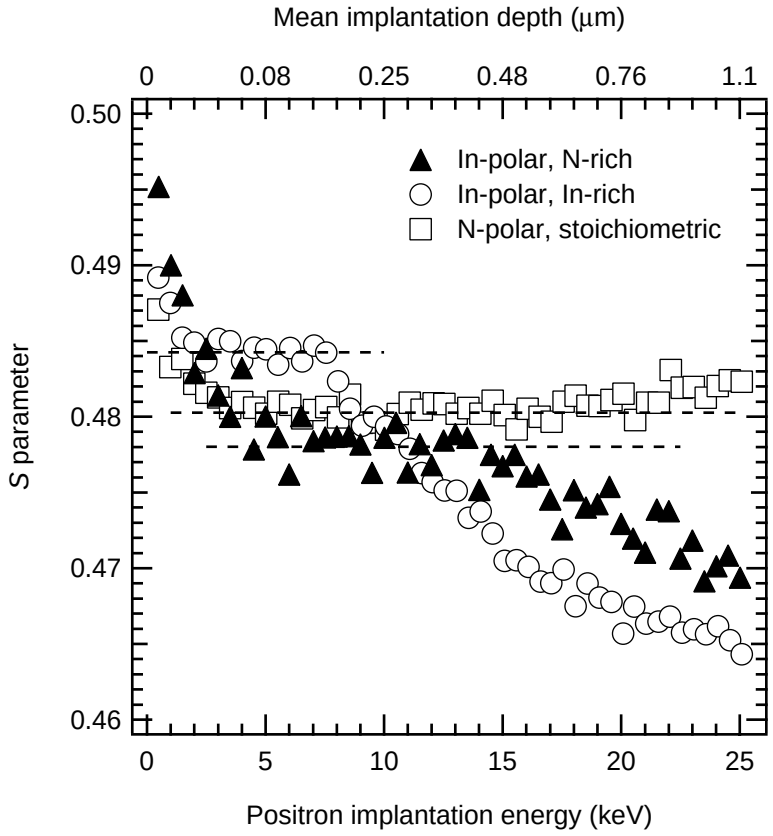

Figure 30. Doppler-broadening lineshape S parameter as a function of positron implantation energy (depth) in selected PAMBE-InN samples.

An increased (decreased) S (W) value in the InN layer indicates that the electron momentum-distribution is narrower than in the perfect InN lattice, and is a clear sign of the presence of vacancy defects. To identify the vacancies, the layer-average (S,W) values, i.e., averaged over the energy ranges corresponding to the InN layers, are shown in Figure 31. In nearly all the samples, the points fall on the line between the two states previously identified as the delocalised state in the InN lattice and the trapped state in V_{In} (cf. Eq. (13)), by combining Doppler-broadening and lifetime data [193, 216]. Since the (S,W) values of the sample In(N)-1 coincide with the InN lattice values (S_B,W_B), these values were additionally confirmed to indeed correspond to the delocalised InN-lattice-state by lifetime measurements in the sample, which showed practically only a single lifetime component of around 184 ps, equal to the calculated lifetime in the InN lattice [193, 200]. The V_{In} concentrations can be estimated from the data with the positron trapping model assuming a trapping coefficient for V_{In} of 3×10^{15} s^{-1}. The

concentrations ranged from below the room-temperature detection limit of about 1×10^{16} cm^{-3} to 7×10^{16} cm^{-3}, as shown in Figure 31 and Table 1.

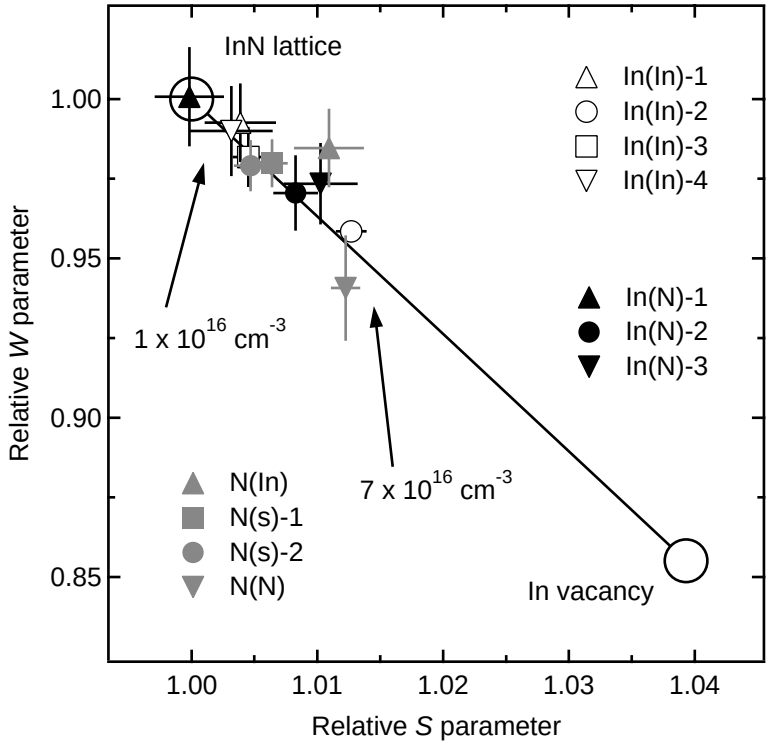

Figure 31. (S, W) plot of the average values in the InN layers (scaled to the InN lattice values (S_B, W_B)).

It can be seen that the growth temperature clearly does not have an effect on the vacancy concentration. Also, in the In-polar samples, the growth stoichiometry does not seem to play a role either. Instead, the use of an MBE-GaN buffer layer in the In-polar growth appears to result in smaller V_{In} concentrations compared to growth on MOCVD-GaN. Another correlation that can be observed in the In-rich In-polar samples is that the vacancy concentration decreases with increasing layer thickness, similar to what has been observed in InN grown by MBE on sapphire [193]. On the other hand, in the N-polar films, the sample grown under N-rich conditions has a clearly higher vacancy concentration than those grown in stoichiometric conditions. The (S,W) point corresponding to the In-rich grown N-polar sample appears off the line connecting the InN lattice and In vacancy in Figure 31. This has been observed also in MOCVD-InN grown in the In-droplet regime, where the effect was attributed to vacancy clustering [194].

The difference between the above observations in In-polar MBE-InN compared to Ga-polar MBE-GaN [217] is substantial—the more N-rich the growth, the more Ga vacancies are formed, while no such effect on In vacancy formation is seen in InN. A similar difference has also been observed in the case of MOCVD growth [194, 218]. A

plausible explanation for the differences in cation-polar material can be found in the vacancy formation energies and the growth temperatures. In *n*-type material, the calculated formation energy of Ga vacancies is about 1 eV, while it is almost 3 eV for the In vacancy [206, 219]. On the other hand, the growth temperature of GaN is 200–300ºC higher than that of InN in MBE growth, and up to 500ºC higher in MOCVD growth. As the concentrations of the Ga and In vacancies are similar in samples in near-stoichiometric conditions, the formation of the In vacancies must be dictated by other factors related to the structural quality of the material rather than thermal formation (and subsequent stabilisation by, e.g., impurities). On the other hand, the observed Ga vacancy concentrations in samples with low dislocation densities are of the same order of magnitude that could be expected from the growth temperature and the calculated formation, given that the vacancies (which are mobile already at relatively low temperatures) are stabilised by impurities (such as O) or other defects relatively close to the growth temperature [95, 216, 220, 221]. Hence, it may be understood why the stoichiometric conditions affect the final In vacancy concentration in InN less than the Ga vacancy concentration in GaN.

Additionally, as mentioned, the In vacancy concentration is lower in the samples where a MBE-GaN buffer layer has been used instead of growing directly on a MOCVD-GaN template. This is in good agreement with results of optimising the MBE-GaN buffer for InN growth [181], further supporting the view that even in state-of-the-art InN, the structural quality of the material dictates the In vacancy formation. Interestingly, even if the higher temperature in N-polar growth does not lead to higher In vacancy concentrations compared to In-polar growth, the growth stoichiometry seems to have some effect. This can be understood by the thermodynamical formation of vacancies becoming more important owing to the higher temperature, even if the structural effects are still dominant.

Another difference between MBE InN and GaN can be found when comparing N-polar and In/Ga-polar growth. In the case of InN, the vacancy concentrations are similar for both polarities, while in GaN, very high vacancy concentrations are observed in N-rich N-polar layers [217]. Interestingly, in Ga-rich N-polar MBE-GaN, on the other hand, efficient clustering of vacancies was observed in Ref. [217], and a similar (although very small) effect is seen in the present data on In-rich N-polar MBE-InN. A possible explanation could be that the formation of N vacancies is strongly enhanced in Ga/In-rich N-polar growth, where a larger number of N sites are available to be left empty at the growth surface, but as the formation of In vacancies is much less probable than that of Ga vacancies, clustering is less efficient in InN.

Finally, although in earlier work a connection between V_{In} and carrier mobility has been proposed [193], here we find no apparent correlation between V_{In} concentration and mobility. Instead, this is supportive to the view that extended defects are the dominant scattering centres in as-grown, nominally undoped InN [207].

4.3 Vacancy defects in InN after He irradiation and rapid thermal annealing

Doppler-broadening studies were performed on a set of MBE-grown, nominally undoped wurtzite InN films that were irradiated with 2-MeV $^4He^+$ ions at different fluences in the range $\phi = 5.6\times10^{14}$–1.8×10^{16} cm^{-2}. The films were grown on *c*-sapphire with an AlN and/or GaN buffer layer, and their thickness was 0.6 μm, except for the one irradiated at 2.2×10^{15} cm^{-2}, which was 2.7 μm thick. The penetration depth of the He ions is about 7 μm, so the irradiation damage was roughly uniform throughout the films. After irradiation, the films were rapid-thermal-annealed at temperatures between 425–475°C for 5 to 10 minutes. More information on the samples can be found in Refs. [213, 215]. In addition to the Doppler-broadening technique, positron lifetime measurements were also performed using a pulsed slow-positron beam. For comparison, similarly treated GaN films grown by MOCVD were also studied.

Figure 32 shows the Doppler-broadening parameters in selected InN samples as a function of energy, measured at room temperature. The data from an as-grown film are also shown as a reference. The pre-RTA data are from Ref. [216]. The increased (decreased) *S* (*W*) parameter in the irradiated InN layers is due to the presence of V_{In}. The heat treatment is clearly seen to change the behaviour of the *S* parameter, indicating a depth profile in the vacancy distribution. The *W* parameter, on the other hand, shifts in the annealing more evenly throughout the layer back towards the value of the as-grown sample. It should be noted that in the sample irradiated with the highest fluence, the *S* parameter exhibits a slightly similar profile already before the RTA.

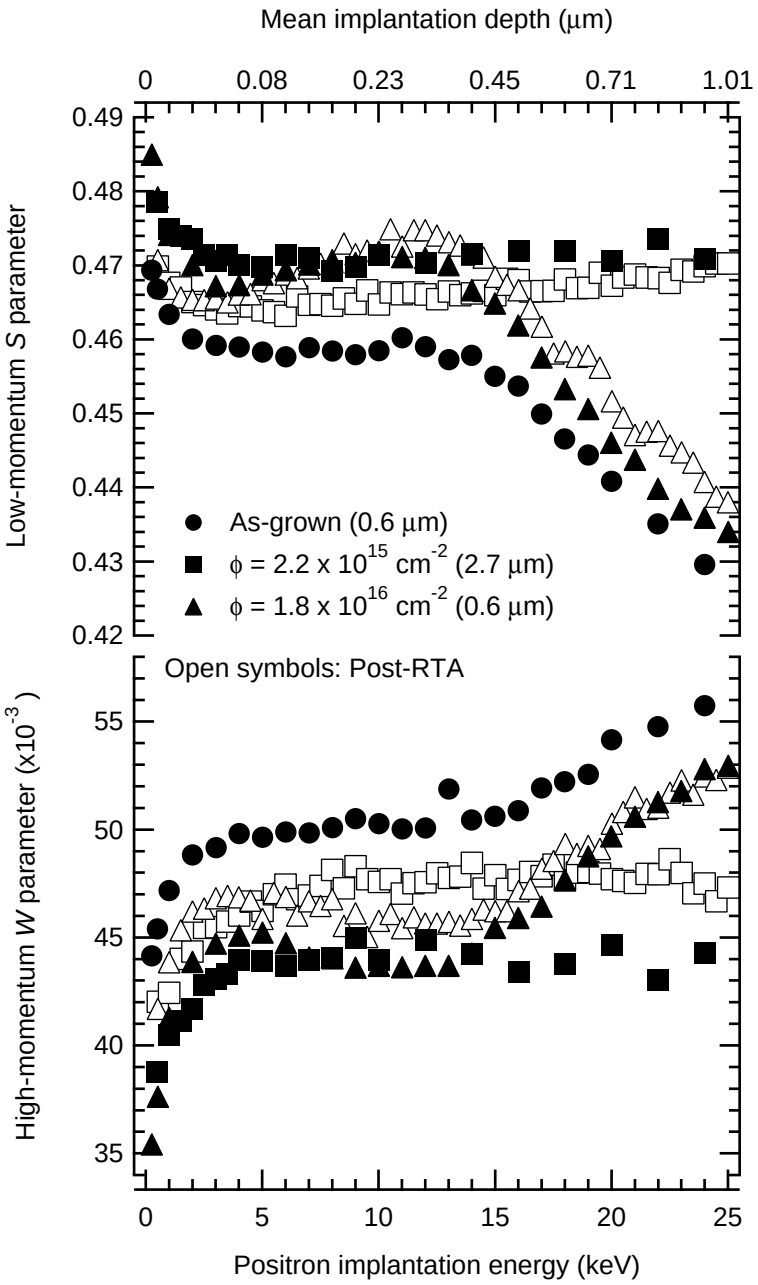

Figure 32. Doppler-broadening parameters S and W as a function of positron implantation energy in selected He-irradiated InN samples, before and after thermal annealing. The low-energy range roughly below 4 keV is dominated by annihilations from surface states, while in the thinnest films, the substrate is reached at energies above 12 keV. The RTA treatment introduces a clear depth profile in the InN-layer S parameter, indicating a redistribution of the irradiation-induced In vacancies.

The room-temperature Doppler-broadening (S,W) plots are shown in Figure 33. The data from the annealed samples has been separated into two regions, one corresponding to the InN layer away from the film–substrate interface, where the *S* parameter is

smallest, and another corresponding to the region close to the interface. In the layer region, the points fall on the same line connecting the InN bulk state and V_{In} as before the RTA, indicating that V_{In} are still present [193, 216]. Their concentration, however, is clearly lower than before the RTA process, since the points lie closer to the bulk value. Near the interface, on the other hand, a different type of In vacancy appears to be present, since the points lie on a different line with a gentler slope. A similar effect has been observed in studies of Si-doped InN [222] and in MOCVD films grown with low V/III ratios [194], where the possibility of vacancy cluster formation was proposed. Since the sample irradiated at $\phi = 1.8\times10^{16}$ cm^{-2} exhibited a mild depth profile already prior to the RTA, the values corresponding to the as-irradiated sample were taken from the near-interface region. However, we see that they clearly fall on the bulk-InN–V_{In} line, indicating that in the as-irradiated sample, the defect profile is due to a slight accumulation of the V_{In} towards the interface.

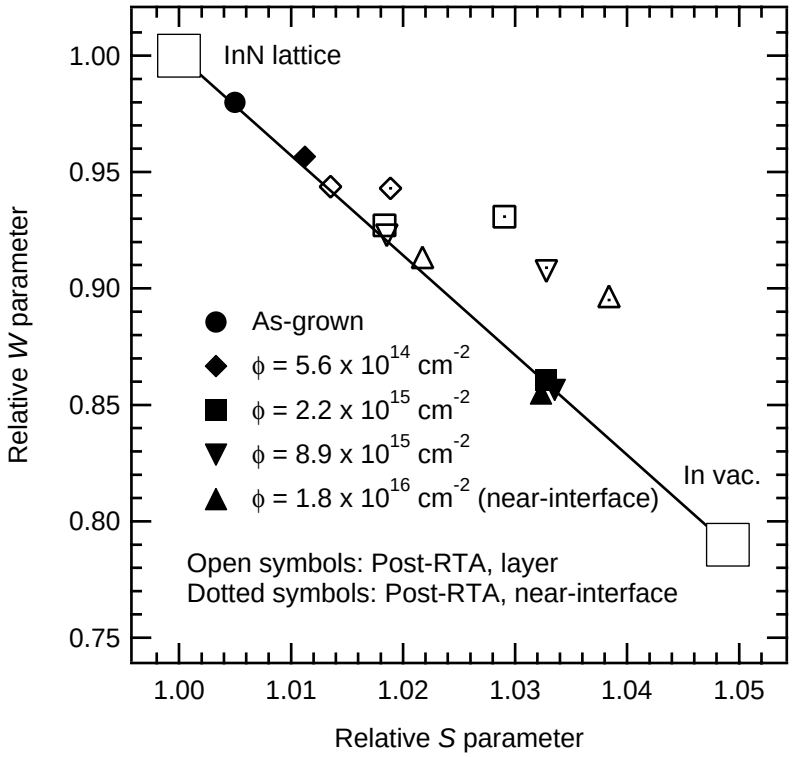

Figure 33. (S, W) plot of the InN samples. In the layer region, the points are closer to the bulk value after the heat treatment, indicating that the irradiation-induced V_{In} are partially removed in the RTA. Near the interface, however, the points no longer fall on the line connecting the InN bulk state and the trapped state in V_{In}, which suggests that a different In-vacancy defect is present.

In the GaN films, on the other hand, the Doppler-broadening data showed simply a partial recovery of the irradiation-induced V_{Ga} in the RTA. This is in agreement with earlier studies on electron-irradiated GaN [223]. Especially, no depth profiles were observed in the defect distribution in the GaN films.

For further investigating the unidentified In vacancies, lifetime measurements were performed on the most heavily irradiated InN film. The lifetime spectra were decomposed with a conventional sum-of-exponentials fit (Eq. (9)), and the best fit was obtained with three lifetime components. The results of the decompositions are shown in Figure 34. Throughout the InN layer, the second component τ_2 is very close to the previously determined lifetime in V_{In} of 260 ps [193, 200]. Also, its intensity as a function of depth follows a similar trend as the S parameter. This indicates that the vacancies near the interface have an open volume close to the In monovacancy. The third component has values typical to larger vacancy clusters. However, due to its very small intensity, it may also be an instrument or fitting artefact.

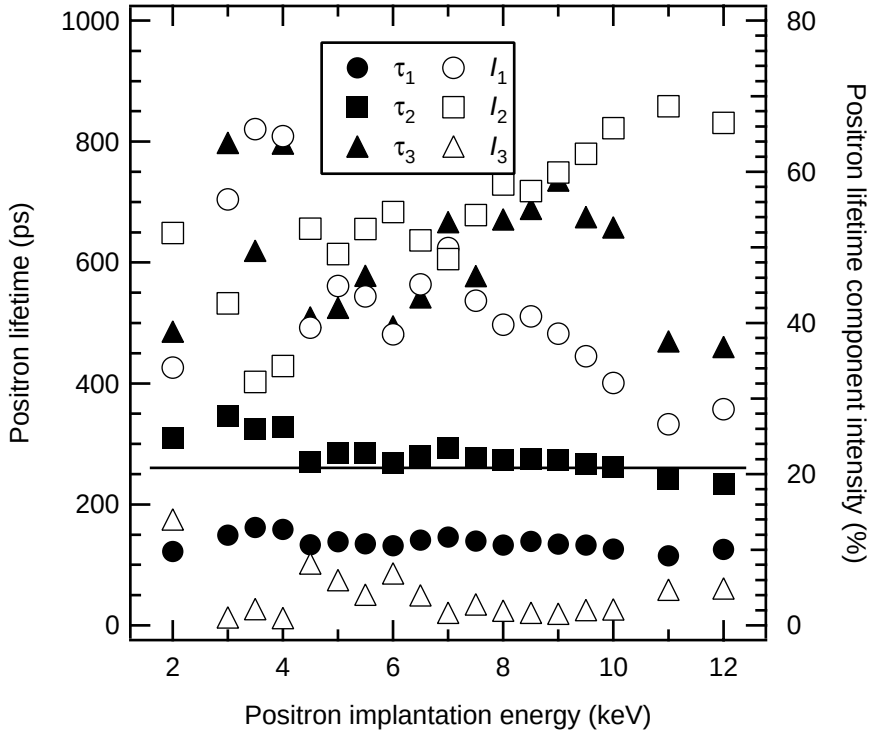

Figure 34. Slow-positron lifetime data from the most heavily irradiated InN film after thermal annealing. The solid line represents the lifetime in V_{In}, which is seen to coincide well with the second lifetime component throughout the InN layer. Its intensity increases from about 50% to 70% towards the interface. The magnitude of the third lifetime component is typical of larger open-volume defects such as vacancy clusters, but its intensity is too small for reliably determining its origin.

Since negative-ion type defects were observed in the irradiated samples by variable-temperature Doppler broadening [216], the temperature-dependence measurements were repeated in the annealed films. Figure 35 shows the S parameter in the one of the samples as a function of temperature in the range 30–300 K. The behaviour is typical of when negative ions, i.e., shallow traps, are present. The shallow traps begin to compete with vacancies in trapping at low temperatures (see Sec. 2.1.1). Since they produce the

characteristic lineshape of the lattice, the *S* (and *W*, not shown) parameter converges towards the bulk value as the temperature decreases.

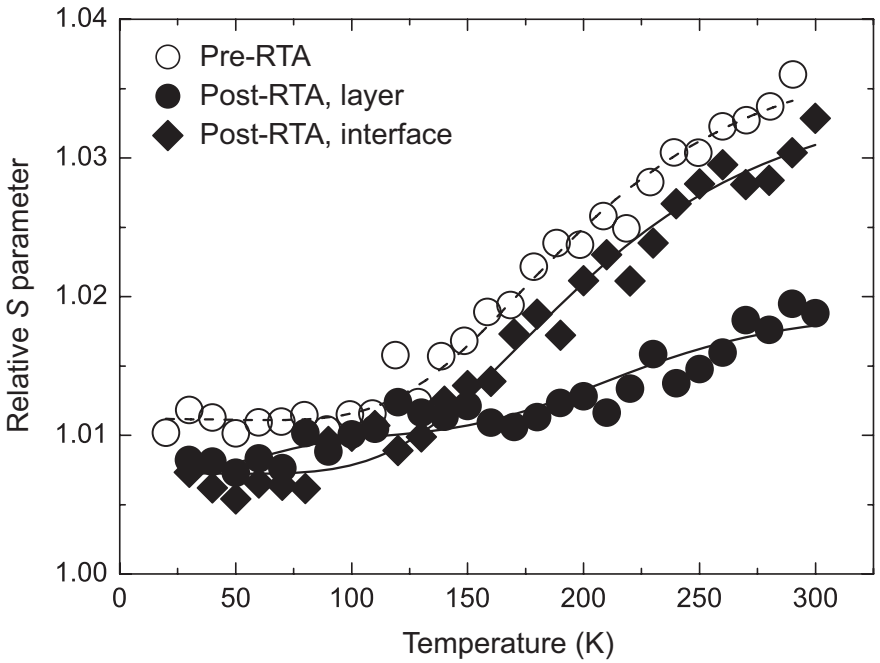

Figure 35. The S parameter as a function of temperature in the InN film irradiated at $\phi = 8.9\times10^{15}$ cm^{-2}. In both regions of the annealed film, the behaviour is similar as before the RTA, indicating that negative ions are still present.

The layer-region V_{In} concentrations were estimated from the temperature-dependent data using the positron trapping model [224]. A room-temperature trapping coefficient of 3×10^{15} s^{-1} was used for both V_{In} and the shallow traps. Figure 36 shows the calculated defect concentrations, including the concentrations before the RTA. The V_{In} concentrations were also determined from the room-temperature data and were found to be in consistence. The negative-ion concentrations are seen to decrease in the annealing process by roughly half an order of magnitude, while the In-vacancy concentration drops slightly less.

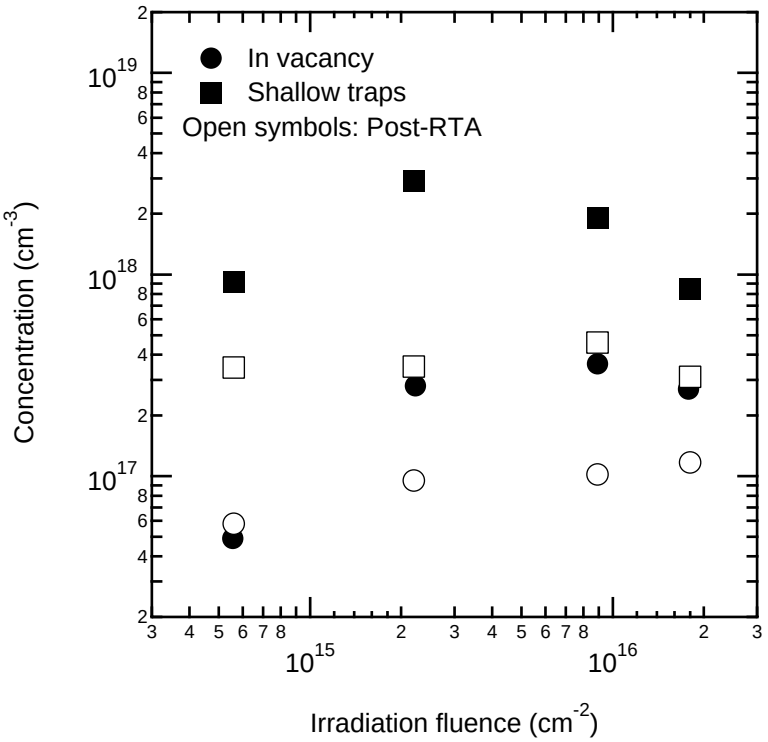

Figure 36. Indium vacancy and shallow trap concentrations in the layer region of the irradiated InN films.

In conclusion, we observe a reorganization of point defects in the rapid-thermal-annealing of the InN films. The heat-treated InN layers are found to contain decreased concentrations of irradiation-induced V_{In} and negative ion defects, while on the other hand, different In vacancy defects not observed in the as-irradiated samples are observed near the growth interface. In transmission electron microscopy, on the other hand, the RTA has been observed to cause structural changes in the irradiated InN films [225]. The as-grown layers were found to contain elevated dislocation densities near the growth interface, while small dislocation loops were found after the irradiation. After the thermal treatment, increased densities of dislocation loops were observed, possibly resulting from the agglomeration of irradiation-induced vacancy defects, and large voids were found at the interface with the GaN buffer layer.

We observe a decrease of roughly half to one order of magnitude in the irradiation-induced V_{In} and negative ion concentrations in the RTA (Figure 36). However, as proposed in Ref. [216], because the irradiated films are heavily *n*-type, the negative ion concentrations might be underestimated due to electron screening. Since the RTA has little effect on the carrier concentration (Sec. 4.1), the screening effect in the annealed films should be similar to the as-irradiated samples. It is hence plausible that these defects could ultimately limit the electron mobility in the irradiated films.

The behavior of the InN layers is quite different compared to the GaN films. As discussed previously, the formation of In vacancies in InN is considered to be dominated by the structural properties of the material, such as extended defects that form especially near the growth interface [193, 194, 226], rather than growth kinetics. It is therefore interesting that the growth interface seems to play an important role in the behavior of the irradiation-induced point defects during the RTA, suggesting that their behavior is influenced by the local material structure. The unidentified near-interface vacancies might hence be associated with extended lattice defects such as dislocations [207]. Further work is underway to better identify these defects.

5 Summary

In this work, a new laboratory-scale pulsed slow-positron beam for positron lifetime experiments in thin material layers is presented. Using a combination of two RF beam bunchers and a chopper, the initial low-energy DC positron beam is time-compressed into short (~200 ps FWHM) bunches and accelerated to an implantation energy adjustable between 2–25 keV. The repetition period of the pulsing system is 30 ns, making it suitable especially for lifetime studies in semiconductor materials. The target sample is held at ground potential during measurements, which facilitates sample manipulation. The lifetime is measured using a high-speed digitiser, which has several benefits over the traditional analogue electronics chain. The technical design and performance characteristics of the instrument are presented. Also, the analysis of experimental data is discussed.

Also in this work, positron annihilation techniques are applied to study vacancy defects in indium nitride. InN shows much potential as a semiconductor material for optoelectronic, photovoltaic, and high-speed electronic applications. Here, the role of indium vacancies in different InN films is studied. Effects of growth conditions on V_{In} formation in PAMBE-grown films are investigated. The results suggest that, contrary to what is observed in the more thoroughly studied III–nitride, GaN, the formation of In vacancies in InN is—at the present level in material synthesis—less dependent on the growth conditions than on the crystal quality. In addition, He irradiated and rapid thermal annealed MBE-grown InN is studied in this work. The positron annihilation results show a reorganisation of the irradiation-induced defects in the thermal annealing. The V_{In} and negative ions present in the irradiated films are partially recovered in the heat treatment, while near the growth interface, the data shows a change in the chemical environment of the In vacancies. The observed restructuring is suspected to be connected with extended defects at the growth interface, and might be responsible for the improved carrier mobility in the post-irradiation annealed InN films.

References

[1] Antti Laakso. *Construction of a Pulsing System for Low-Energy Positrons*. PhD thesis, Department of Engineering Physics, Helsinki University of Technology, Finland, 2005.

[2] W. Brandt and A. Dupasquier, editors. *Positron Solid-State Physics*. North-Holland, Amsterdam, 1983.

[3] W. Brandt and A. Dupasquier, editors. *Positrons in Solids*, volume Course LXXXIII of *Proceedings of the International School of Physics "E. Fermi"*. IOS Press, Amsterdam, 1983.

[4] Paul Coleman, editor. *Positron Beams and their applications*. World Scientific, 2000.

[5] L. Dorikens-Vanpraet, M. Dorikens, and D. Segers, editors. *Positron annihilation*. World Scientific, Singapore, 1989.

[6] P. Hautojärvi, editor. *Positrons in Solids*, volume 12 of *Topics in Current Physics*. Springer, Berlin, 1979.

[7] P. C. Jain, R. M. Singru, and K. P. Gopinathan, editors. *Positron annihilation*. World Scientific, Singapore, 1985.

[8] Reinhard Krause-Rehberg and Hartmut Leipner. *Positron Annihilation in Semiconductors: Defect Studies*, volume 127 of *Springer Series in Solid-State Sciences*. Springer, 1 edition, 1999.

[9] A. P. Mills, Jr., W. S. Crane, and K. F. Cantor, editors. *Positron Studies of Solids, Surfaces and Atoms*. World Scientific, Singapore, 1986.

[10] K. Saarinen, P. Hautojärvi, and C. Corbel. *Identification of Defects in Semiconductors*, volume 51A of *Semiconductors and Semimetals*, chapter 5. Academic Press, New York, 1998.

[11] K. F. Canter, A. P. Mills, and S. Berko. Efficient positronium formation by slow positrons incident on solid targets. *Physical Review Letters*, 33(1):7–10, July 1974.

[12] A. P. Mills, Jr. *Positron Solid-State Physics*, pages 432–509. North-Holland, Amsterdam, 1983.

[13] Peter J. Schultz and K. G. Lynn. Interaction of positron beams with surfaces, thin films, and interfaces. *Reviews of Modern Physics*, 60(3):701–779, July 1988.

[14] W. Triftshäuser and G. Kögel. Defect structures below the surface in metals investigated by monoenergetic positrons. *Physical Review Letters*, 48(25):1741–1744, June 1982.

[15] A. Vehanen. Defect profiling with slow positrons. In L. Dorikens-Vanpraet, M. Dorikens, and D. Segers, editors, *Positron Annihilation*, pages 39–51. World Scientific, Singapore, 1989.

[16] D. G. Costello, D. E. Groce, D. F. Herring, and J. Wm. McGowan. Evidence for the negative work function associated with positrons in gold. *Physical Review B*, 5(4):1433–1436, February 1972.

[17] N. Alberola, T. Anthonioz, A. Badertscher, C. Bas, A. S. Belov, P. Crivelli, S. N. Gninenko, N. A. Golubev, M. M. Kirsanov, A. Rubbia, and D. Sillou. Development of a high-efficiency pulsed slow positron beam for measurements with orthopositronium in vacuum. *Nuclear Instruments and Methods in Physics Research Section A: Accelerators, Spectrometers, Detectors and Associated Equipment*, 560(2):224–232, May 2006.

[18] W. S. Crane and A. P. Mills, Jr. Subnanosecond bunching of a positron beam. *Review of Scientific Instruments*, 56(9):1723–1726, September 1985.

[19] J. De Baerdemaeker and C. Dauwe. Development and application of the Ghent pulsed positron beam. *Applied Surface Science*, 194(1–4):52–55, June 2002.

[20] E. Hamada, N. Oshima, T. Suzuki, H. Kobayashi, K. Kondo, I. Kanazawa, and Y. Ito. New system for a pulsed slow-positron beam using a radioisotope. *Radiation Physics and Chemistry*, 58(5–6):771–775, June 2000.

[21] Eisaku Hamada, Nagayasu Oshima, Takenori Suzuki, Hitoshi Kobayashi, Kenjiro Kondo, Ikuzo Kanazawa, and Yasuo Ito. Development of a pulsed slow-positron beam using time-varying pulsing-bias. *Applied Surface Science*, 149(1–4):40–43, August 1999.

[22] Chunqing He, Eisaku Hamada, Takenori Suzuki, Takashi Kumaki, Hitoshi Kobayashi, Kenjiro Kondo, and Yasuo Ito. Pulsed slow-positron beam for polymer films. *Applied Surface Science*, 221(1–4):444–449, January 2004.

[23] Masafumi Hirose, Terunobu Nakajyo, and Masakazu Washio. A compact cyclotron based slow positron beam and a new positron pulsing system. *Applied Surface Science*, 116:63–67, May 1997.

[24] P. Y. Kwan, C. K. Cheung, C. D. Beling, and S. Fung. Preliminary studies on a variable energy positron annihilation lifetime spectroscopy system. *Applied Surface Science*, 252(9):3138–3142, February 2006.

[25] K. G. Lynn, W. E. Frieze, and Peter J. Schultz. Measurement of the positron surface-state lifetime for Al. *Physical Review Letters*, 52(13):1137–1140, March 1984.

[26] J. P. Merrison, M. Charlton, P. Aggerholm, H. Knudsen, D. P. van der Werf, J. Clarke, and M. R. Poulsen. Development and applications of time-bunched and velocity-selected positron beams. *Review of Scientific Instruments*, 74(7):3284–3292, July 2003.

[27] L. Mileshina and A. Nordlund. Design and performance of the pulsed positron beam at Chalmers University of Technology. *Nuclear Instruments and Methods in Physics Research Section B: Beam Interactions with Materials and Atoms*, 267(17):2934–2937, September 2009.

[28] Terunobu Nakajyo and Masafumi Hirose. The SHI slow positron beam pulsing system using an induction cavity. *Applied Surface Science*, 149(1–4):34–39, August 1999.

[29] Nagayasu Oshima, Takenori Suzuki, Ikuzo Kanazawa, and Yasuo Ito. Design of a high-efficiency short-pulsed positron beam system. *Applied Surface Science*, 116:82–86, May 1997.

[30] D. Schödlbauer, P. Sperr, G. Kögel, and W. Triftshäuser. A pulsing system for low energy positrons. *Nuclear Instruments and Methods in Physics Research Section B: Beam Interactions with Materials and Atoms*, 34(2):258–268, August 1988.

[31] R. Suzuki, Y. Kobayashi, T. Mikado, H. Ohgaki, M. Chiwaki, T. Yamazaki, and T. Tomimasu. Slow positron pulsing system for variable energy positron lifetime spectroscopy. *Japanese Journal of Applied Physics*, 30(3B):L532–L534, March 1991.

[32] Stanislaw Szpala, Mihail P. Petkov, and Kelvin G. Lynn. A simple positron lifetime spectrometer for a magnetically guided low-energy beam. *Review of Scientific Instruments*, 73(1):147–155, January 2002.

[33] M. Tashiro, Y. Honda, T. Yamaguchi, P. K. Pujari, N. Kimura, T. Kozawa, G. Isoyama, and S. Tagawa. Development of a short-pulsed slow positron beam for application to polymer films. *Radiation Physics and Chemistry*, 60(4–5):529–533, 2001.

[34] G. Kögel. Lifetime spectroscopy in sub-surface defect studies. In L. Dorikens-Vanpraet, M. Dorikens, and D. Segers, editors, *Positron Annihilation*, pages 52–55. World Scientific, Singapore, 1989.

[35] A. Mills. Time bunching of slow positrons for annihilation lifetime and pulsed laser photon absorption experiments. *Applied Physics A: Materials Science & Processing*, 22(3):273–276, July 1980.

[36] D. Schödlbauer, G. Kögel, P. Sperr, and W. Triftshäuser. Lifetime measurements with a pulsed slow positron beam. *physica status solidi (a)*, 102(2):549–554, 1987.

[37] D. Schödlbauer, P. Sperr, G. Kögel, and W. Triftshauser. A pulsed positron beam for lifetime studies. In P. C. Jain, R. M. Singru, and K. P. Gopinathan, editors, *Positron annihilation*, pages 957–959. World Scientific, Singapore, 1985.

[38] R. Suzuki, Y. Kobayashi, T. Mikado, H. Ohgaki, M. Chiwaki, T. Yamazaki, A. Uedono, S. Tanigawa, and H. Funamoto. Characterization of diamond films by means of a pulsed positron beam. *Japanese Journal of Applied Physics*, 31(7):2237–2240, July 1992.

[39] K. Fallström and T. Laine. Construction of the Helsinki University of Technology (HUT) pulsed positron beam. *Applied Surface Science*, 149(1–4):44–48, August 1999.

[40] A. Laakso, K. Saarinen, and P. Hautojärvi. Positron lifetime beam for defect studies in thin epitaxial semiconductor structures. *Physica B: Condensed Matter*, 308–310:1157–1160, December 2001.

[41] Antti Pelli. Pulssitetun positronisuihkun rakentaminen ja testaus (Construction and testing of a pulsed positron beam). Master's thesis, Department of Engineering Physics, Helsinki University of Technology, Finland, January 2002.

[42] F. Bechstedt and J. Furthmüller. Do we know the fundamental energy gap of InN? *Journal of Crystal Growth*, 246(3–4):315–319, December 2002.

[43] Enrico Bellotti, Bhautik K. Doshi, Kevin F. Brennan, John D. Albrecht, and P. Paul Ruden. Ensemble Monte Carlo study of electron transport in wurtzite InN. *Journal of Applied Physics*, 85(2):916–923, January 1999.

[44] V. Yu. Davydov, A. A. Klochikhin, R. P. Seisyan, V. V. Emtsev, S. V. Ivanov, F. Bechstedt, J. Furthmüller, H. Harima, A. V. Mudryi, J. Aderhold, O. Semchinova, and J. Graul. Absorption and emission of hexagonal InN. Evidence of narrow fundamental band gap. *physica status solidi (b)*, 229(3):r1–r3, 2002.

[45] Brian E. Foutz, Stephen K. O'Leary, Michael S. Shur, and Lester F. Eastman. Transient electron transport in wurtzite GaN, InN, and AlN. *Journal of Applied Physics*, 85(11):7727–7734, June 1999.

[46] T. Inushima, V. V. Mamutin, V. A. Vekshin, S. V. Ivanov, T. Sakon, M. Motokawa, and S. Ohoya. Physical properties of InN with the band gap energy of 1.1 eV. *Journal of Crystal Growth*, 227–228:481–485, July 2001.

[47] R. E. Jones, K. M. Yu, S. X. Li, W. Walukiewicz, J. W. Ager, E. E. Haller, H. Lu, and W. J. Schaff. Evidence for p-type doping of InN. *Physical Review Letters*, 96(12):125505–4, March 2006.

[48] T. Matsuoka, H. Okamoto, H. Takahata, T. Mitate, S. Mizuno, Y. Uchiyama, and T. Makimoto. MOVPE growth and photoluminescence of wurtzite InN. *Journal of Crystal Growth*, 269(1):139–144, August 2004.

[49] Takashi Matsuoka, Hiroshi Okamoto, Masashi Nakao, Hiroshi Harima, and Eiji Kurimoto. Optical bandgap energy of wurtzite InN. *Applied Physics Letters*, 81(7):1246–1248, August 2002.

[50] Yasushi Nanishi, Yoshiki Saito, and Tomohiro Yamaguchi. RF-molecular beam epitaxy growth and properties of InN and related alloys. *Japanese Journal of Applied Physics*, 42(5A):2549–2559, 2003.

[51] Stephen K. O'Leary, Brian E. Foutz, Michael S. Shur, and Lester F. Eastman. Steady-state and transient electron transport within bulk wurtzite indium nitride: An updated semiclassical three-valley Monte Carlo simulation analysis. *Applied Physics Letters*, 87(22):222103–3, November 2005.

[52] Stephen K. O'Leary, Brian E. Foutz, Michael S. Shur, and Lester F. Eastman. Potential performance of indium-nitride-based devices. *Applied Physics Letters*, 88(15):152113–3, April 2006.

[53] B. Rezaei, A. Asgari, and M. Kalafi. Electronic band structure pseudopotential calculation of wurtzite III-nitride materials. *Physica B: Condensed Matter*, 371(1):107–111, January 2006.

[54] Y. Saito, H. Harima, E. Kurimoto, T. Yamaguchi, N. Teraguchi, A. Suzuki, T. Araki, and Y. Nanishi. Growth temperature dependence of indium nitride crystalline quality grown by RF-MBE. *physica status solidi (b)*, 234(3):796–800, 2002.

[55] S. Strite and H. Morkoc. GaN, AlN, and InN: A review. *Journal of Vacuum Science and Technology B*, 10(4):1237–1266, July 1992.

[56] K. T. Tsen, C. Poweleit, D. K. Ferry, Hai Lu, and William J. Schaff. Observation of large electron drift velocities in InN by ultrafast Raman spectroscopy. *Applied Physics Letters*, 86(22):222103–3, May 2005.

[57] W. Walukiewicz, J. W. Ager III, K. M. Yu, Z. Liliental-Weber, J. Wu, S. X. Li, R. E. Jones, and J. D. Denlinger. Structure and electronic properties of InN and In-rich group III-nitride alloys. *Journal of Physics D: Applied Physics*, 39(5):R83–R99, 2006.

[58] W. Walukiewicz, R. E. Jones, S. X. Li, K. M. Yu, J. W. Ager III, E. E. Haller, H. Lu, and W. J. Schaff. Dopants and defects in InN and InGaN alloys. *Journal of Crystal Growth*, 288(2):278–282, March 2006.

[59] W. Walukiewicz, S. X. Li, J. Wu, K. M. Yu, J. W. Ager, E. E. Haller, Hai Lu, and William J. Schaff. Optical properties and electronic structure of InN and In-rich group III-nitride alloys. *Journal of Crystal Growth*, 269(1):119–127, August 2004.

[60] J. Wu, W. Walukiewicz, K. M. Yu, J. W. Ager III, E. E. Haller, Hai Lu, William J. Schaff, Yoshiki Saito, and Yasushi Nanishi. Unusual properties of the fundamental band gap of InN. *Applied Physics Letters*, 80(21):3967–3969, May 2002.

[61] J. Wu, W. Walukiewicz, K. M. Yu, W. Shan, J. W. Ager III, E. E. Haller, Hai Lu, William J. Schaff, W. K. Metzger, and Sarah Kurtz. Superior radiation resistance of $In_{1-x}Ga_xN$ alloys: Full-solar-spectrum photovoltaic material system. *Journal of Applied Physics*, 94(10):6477–6482, November 2003.

[62] P. Hautojärvi and C. Corbel. Positron spectroscopy of defects in metals and semiconductors. In A. Dupasquier and A. P. Mills, Jr., editors, *Positron Spectroscopy of Solids*, pages 491–532. IOS Press, Amsterdam, 1993.

[63] M. J. Puska and R. M. Nieminen. Theory of positrons in solids and on solid surfaces. *Review of Modern Physics*, 66(3):841–897, July 1994.

[64] A. Perkins and J. P. Carbotte. Effect of the positron-phonon interaction on positron motion. *Physical Review B*, 1(1):101–107, January 1970.

[65] K. O. Jensen and A. B. Walker. Positron thermalization and non-thermal trapping in metals. *Journal of Physics: Condensed Matter*, 2(49):9757–9775, 1990.

[66] R. M. Nieminen and J. Oliva. Theory of positronium formation and positron emission at metal surfaces. *Physical Review B*, 22(5):2226–2247, September 1980.

[67] B. Bergersen, E. Pajanne, P. Kubica, M. J. Stott, and C. H. Hodges. Positron diffusion in metals. *Solid State Communications*, 15(8):1377–1380, October 1974.

[68] O. V. Boev, M. J. Puska, and R. M. Nieminen. Electron and positron energy levels in solids. *Physical Review B*, 36(15):7786–7794, November 1987.

[69] E. Soininen, H. Huomo, P. A. Huttunen, J. Mäkinen, A. Vehanen, and P. Hautojärvi. Temperature dependence of positron diffusion in cubic metals. *Physical Review B*, 41(10):6227–6233, April 1990.

[70] E. Soininen, J. Mäkinen, D. Beyer, and P. Hautojärvi. High-temperature positron diffusion in Si, GaAs, and Ge. *Physical Review B*, 46(20):13104–13118, November 1992.

[71] M. J. Puska, C. Corbel, and R. M. Nieminen. Positron trapping in semiconductors. *Physical Review B*, 41(14):9980–9993, May 1990.

[72] M. Alatalo, B. Barbiellini, M. Hakala, H. Kauppinen, T. Korhonen, M. J. Puska, K. Saarinen, P. Hautojärvi, and R. M. Nieminen. Theoretical and experimental study of positron annihilation with core electrons in solids. *Physical Review B*, 54(4):2397–2409, July 1996.

[73] B. Barbiellini, M. J. Puska, T. Korhonen, A. Harju, T. Torsti, and R. M. Nieminen. Calculation of positron states and annihilation in solids: A density-gradient-correction scheme. *Physical Review B*, 53(24):16201–16213, June 1996.

[74] B. Barbiellini, M. J. Puska, T. Torsti, and R. M. Nieminen. Gradient correction for positron states in solids. *Physical Review B*, 51(11):7341–7344, March 1995.

[75] E. Boronski and R. M. Nieminen. Electron-positron density-functional theory. *Physical Review B*, 34(6):3820–3831, September 1986.

[76] A. Dupasquier and A. P. Mills, Jr., editors. *Positron Spectroscopy of Solids*. IOS Press, Amsterdam, 1995.

[77] A. Mills and C. Murray. Diffusion of positrons to surfaces. *Applied Physics A: Materials Science & Processing*, 21(4):323–325, April 1980.

[78] M. Bertolaccini, A. Bisi, G. Gambarini, and L. Zappa. Positron states in ionic media. *Journal of Physics C: Solid State Physics*, 4(6):734–745, 1971.

[79] Werner Brandt. Positron dynamics in solids. *Applied Physics A: Materials Science & Processing*, 5(1):1–23, October 1974.

[80] G. Kögel. Positron diffusion in solids and the reconstruction of inhomogeneous defect distributions from lifetime measurements. *Applied Physics A: Materials Science & Processing*, 63(3):227–235, September 1996.

[81] Esa Korhonen. Pulssitetun positronisuihkun data-analyysi ja ohjausjärjestelmän kehitys (Data analysis and development of the control system for a pulsed positron beam). Master's thesis, Department of Applied Physics, Helsinki University of Technology, Finland, 2009.

[82] G. R. Massoumi, W. N. Lennard, Peter J. Schultz, A. B. Walker, and Kjeld O. Jensen. Experimental and Monte-Carlo studies of electron and positron backscattering. In *AIP Conference Proceedings*, volume 303, pages 564–570, Jackson Hole, Wyoming (USA), June 1994. AIP.

[83] J. Mäkinen, S. Palko, J. Martikainen, and P. Hautojärvi. Positron backscattering probabilities from solid surfaces at 2-30 keV. *Journal of Physics: Condensed Matter*, 4(36):L503–L508, 1992.

[84] S. Valkealahti and R. M. Nieminen. Monte Carlo calculations of keV electron and positron slowing down in solids. II. *Applied Physics A: Materials Science & Processing*, 35(1):51–59, September 1984.

[85] A. H. Weiss and P. G. Coleman. *Positron Beams and their applications*, chapter 5, pages 129–189. World Scientific, Singapore, 2000.

[86] P. G. Coleman. *Positron Beams and their applications*, chapter 2, pages 11–40. World Scientific, Singapore, 2000.

[87] Allen P. Mills. Positronium formation at surfaces. *Physical Review Letters*, 41(26):1828–1831, December 1978.

[88] K. MacKenzie. Experimental methods of annihilation time and energy spectrometry. In W. Brandt and A. Dupasquier, editors, *Positron Solid-State Physics*, pages 196–264. North-Holland, Amsterdam, 1983.

[89] A. Vehanen and K. Rytsölä. Positron lifetime techniques as a tool for defect spectroscopy. In W. Brandt and A. Dupasquier, editors, *Positron Solid-State Physics*, pages 659–678, 1983.

[90] Reino Aavikko. Hyvin lyhyiden aikaerojen digitaalinen mittaaminen (Digital measurement of extremely short time intervals). Master's thesis, Department of Engineering Physics, Helsinki University of Technology, Finland, 2001.

[91] Reino Aavikko. *Positron Lifetime Spectroscopy: Digital Spectrometer and experiments in SiC*. PhD thesis, Department of Engineering Physics, Helsinki University of Technology, Finland, 2005.

[92] Reino Aavikko, Klaus Rytsölä, Jaani Nissilä, and Kimmo Saarinen. Stability and performance characteristics of a digital positron lifetime spectrometer. *Acta Physica Polonica A*, 107(4):592–597, April 2004.

[93] J. Nissilä, K. Rytsölä, R. Aavikko, A. Laakso, K. Saarinen, and P. Hautojärvi. Performance analysis of a digital positron lifetime spectrometer. *Nuclear Instruments and Methods in Physics Research Section A: Accelerators, Spectrometers, Detectors and Associated Equipment*, 538(1–3):778–789, February 2005.

[94] K. Rytsölä, J. Nissilä, J. Kokkonen, A. Laakso, R. Aavikko, and K. Saarinen. Digital measurement of positron lifetime. *Applied Surface Science*, 194(1–4):260–263, June 2002.

[95] F. Tuomisto, T. Suski, H. Teisseyre, M. Krysko, M. Leszczynski, B. Lucznik, I. Grzegory, S. Porowski, D. Wasik, A. Witowski, W. Gebicki, P. Hageman, and K. Saarinen. Polarity dependent properties of GaN layers grown by hydride vapor phase epitaxy on GaN bulk crystals. *physica status solidi (b)*, 240(2):289–292, 2003.

[96] R. Paulin. Implantation of fast positrons in solids. In W. Brandt and A. Dupasquier, editors, *Positron Solid-State Physics*, pages 565–580. North-Holland, Amsterdam, 1983.

[97] D. M. Chen, K. G. Lynn, R. Pareja, and Bent Nielsen. Measurement of positron reemission from thin single-crystal W(100) films. *Physical Review B*, 31(7):4123–4130, April 1985.

[98] D. A. Fischer, K. G. Lynn, and D. W. Gidley. High-resolution angle-resolved positron reemission spectra from metal surfaces. *Physical Review B*, 33(7):4479–4492, April 1986.

[99] A. Goodyear, A. P. Knights, and P. G. Coleman. Energy spectroscopy of positrons re-emitted from polycrystalline tungsten. *Journal of Physics: Condensed Matter*, 6(45):9601–9611, 1994.

[100] E. Gramsch, J. Throwe, and K. G. Lynn. Development of transmission positron moderators. *Applied Physics Letters*, 51(22):1862–1864, November 1987.

[101] C. Hugenschmidt, B. Straßer, and K. Schreckenbach. Investigation of positron work function and moderation efficiency of Ni, Ta, Pt and W(1 0 0). *Applied Surface Science*, 194(1–4):283–286, June 2002.

[102] Mohammed Jibaly, Alex Weiss, A. R. Koymen, D. Mehl, L. Stiborek, and C. Lei. Measurement of the positron work functions of polycrystalline Fe, Mo, Ni, Pt, Ti, and V. *Physical Review B*, 44(22):12166–12171, December 1991.

[103] K. G. Lynn, B. Nielsen, and J. H. Quateman. Development and use of a thin-film transmission positron moderator. *Applied Physics Letters*, 47(3):239–240, August 1985.

[104] Allen P. Mills, Jr. Efficient generation of low-energy positrons. *Applied Physics Letters*, 35(5):427–429, September 1979.

[105] Osamu Sueoka, Casten Makochekanwa, and Satoshi Miyamoto. Reemission intensity and energy spectrum measurements of slow positron beams for various moderators. *Japanese Journal of Applied Physics*, 42(9A):5799–5806, 2003.

[106] Ryoichi Suzuki, Toshiyuki Ohdaira, Akira Uedono, Yang Koo Cho, Sadafumi Yoshida, Yuuki Ishida, Takeshi Ohshima, Hisayoshi Itoh, Mitsukuni Chiwaki, Tomohisa Mikado, Tetsuo Yamazaki, and Shoichiro Tanigawa. Investigation of positron moderator materials for electron-linac-based slow positron beamlines. *Japanese Journal of Applied Physics*, 37(8):4636–4643, 1998.

[107] A. Vehanen, K. G. Lynn, Peter J. Schultz, and M. Eldrup. Improved slow-positron yield using a single crystal tungsten moderator. *Applied Physics A: Materials Science & Processing*, 32(3):163–167, November 1983.

[108] H. M. Weng, C. C. Ling, C. D. Beling, S. Fung, C. K. Cheung, P. Y. Kwan, and I. P. Hui. Tungsten mesh as positron transmission moderator in a monoenergetic positron beam. *Nuclear Instruments and Methods in Physics Research Section B: Beam Interactions with Materials and Atoms*, 225(3):397–401, September 2004.

[109] A. Vehanen and J. Mäkinen. Thin films for slow positron generation. *Applied Physics A: Solids and Surfaces*, 36:97–101, 1985.

[110] L. Liszkay, Zs. Kajcsos, M. F. Barthe, L. Henry, G. Duplâtre, and A. Nagy. Improved tungsten moderator structures for slow positron beams. *Applied Surface Science*, 194(1–4):16–19, June 2002.

[111] Yasuyuki Nagashima, Toshikazu Kurihara, Fuminori Saito, Yoshiko Itoh, Akira Goto, and Toshio Hyodo. Stable, high-efficiency moderator with tungsten mesh. *Japanese Journal of Applied Physics*, 39(9A):5356–5357, 2000.

[112] Fuminori Saito, Yasuyuki Nagashima, Long Wei, Yoshiko Itoh, Akira Goto, and Toshio Hyodo. A high-efficiency positron moderator using electro-polished tungsten meshes. *Applied Surface Science*, 194(1–4):13–15, June 2002.

[113] J. Lahtinen, A. Vehanen, H. Huomo, J. Mäkinen, P. Huttunen, K. Rytsölä, M. Bentzon, and P. Hautojärvi. High-intensity variable-energy positron beam for surface and near-surface studies. *Nuclear Instruments and Methods in Physics*

Research Section B: Beam Interactions with Materials and Atoms, 17(1):73–80, August 1986.

[114] K. G. Lynn and H. Lutz. Slow-positron apparatus for surface studies. *Review of Scientific Instruments*, 51(7):977–982, July 1980.

[115] Peter J. Schultz. A variable-energy positron beam for low to medium energy research. *Nuclear Instruments and Methods in Physics Research Section B: Beam Interactions with Materials and Atoms*, 30(1):94–104, February 1988.

[116] M. Charlton. Review of positron beams. *Nuclear Instruments and Methods in Physics Research Section B: Beam Interactions with Materials and Atoms*, 143(1–2):11–20, August 1998.

[117] C. D. Beling, R. I. Simpson, M. Charlton, F. M. Jacobsen, T. C. Griffith, P. Moriarty, and S. Fung. A field-assisted moderator for low-energy positron beams. *Applied Physics A: Materials Science & Processing*, 42(2):111–116, January 1987.

[118] S. J. Gilbert, C. Kurz, R. G. Greaves, and C. M. Surko. Creation of a monoenergetic pulsed positron beam. *Applied Physics Letters*, 70(15):1944–1946, April 1997.

[119] E. M. Gullikson and A. P. Mills. Positron dynamics in rare-gas solids. *Physical Review Letters*, 57(3):376–379, July 1986.

[120] J. Jääskeläinen, T. Laine, K. Fallström, K. Saarinen, and P. Hautojärvi. Optimized growth conditions for solid Ar and Kr moderators in slow positron beam. *Applied Surface Science*, 116:73–77, May 1997.

[121] K. Lynn and B. McKee. Some investigations of moderators for slow positron beams. *Applied Physics A: Materials Science & Processing*, 19(3):247–255, July 1979.

[122] G. R. Massoumi, N. Hozhabri, W. N. Lennard, P. J. Schultz, S. F. Baert, H. H. Jorch, and A. H. Weiss. Rare gas moderated electrostatic positron beam. *Review of Scientific Instruments*, 62(6):1460–1463, June 1991.

[123] A. P. Mills, Jr. and E. M. Gullikson. Solid neon moderator for producing slow positrons. *Applied Physics Letters*, 49(17):1121–1123, October 1986.

[124] A. P. Mills, Jr., S. S. Voris, Jr., and Tamara S. Andrew. Solid Kr moderator for producing slow positrons. *Journal of Applied Physics*, 76(4):2556–2558, August 1994.

[125] D. Vasumathi, G. Amarendra, K. F. Canter, and A. P. Mills. Installation of a Kr moderator in the high-brightness beam at Brandeis. *Applied Surface Science*, 85:154–157, January 1995.

[126] R. G. Greaves and C. M. Surko. Inward transport and compression of a positron plasma by a rotating electric field. *Physical Review Letters*, 85(9):1883–1886, August 2000.

[127] R. G. Greaves, M. D. Tinkle, and C. M. Surko. Creation and uses of positron plasmas. *Physics of Plasmas*, 1(5):1439–1446, May 1994.

[128] D. B. Cassidy, S. H. M. Deng, R. G. Greaves, and A. P. Mills, Jr. Accumulator for the production of intense positron pulses. *Review of Scientific Instruments*, 77(7):073106–8, July 2006.

[129] D. B. Cassidy and A. P. Mills. The production of molecular positronium. *Nature*, 449(7159):195–197, September 2007.

[130] C. M. Surko and R. G. Greaves. Emerging science and technology of antimatter plasmas and trap-based beams. In *Physics of Plasmas*, volume 11, pages 2333–2348, Albuquerque, New Mexico (USA), May 2004. American Institute of Physics.

[131] D. Passbach. Konstruktion und Aufbau Eines 50-MHz Bunchers für PLEPS III. Master's thesis, Universität der Bundeswehr München, Germany, 1997.

[132] D. Schödlbauer. *Aufbau und Inbetriebnahme einer Gepulsten Positronenquelle für Lebensdauermessungen*. PhD thesis, Universität der Bundeswehr München, Germany, 1987.

[133] Royochi Suzuki. *New Positron Annihilation Experiments in Solids*. PhD thesis, Electrotechnical Laboratory, Japan, 1991.

[134] D. T. Britton. Time-dependent diffusion and annihilation of positrons implanted in a semi-infinite medium. *Journal of Physics: Condensed Matter*, 3(6):681–692, 1991.

[135] D. T. Britton and J. Störmer. Application of time-dependent diffusion models to the study of real solids. *Applied Surface Science*, 85:1–7, January 1995.

[136] W. E. Frieze, K. G. Lynn, and D. O. Welch. Positron trapping model including spatial diffusion of the positron. *Physical Review B*, 31(1):15–19, January 1985.

[137] R. M. Nieminen, J. Laakkonen, P. Hautojärvi, and A. Vehanen. Temperature dependence of positron trapping at voids in metals. *Physical Review B*, 19(3):1397–1402, February 1979.

[138] A. van Veen, H. Schut, M. Clement, J. M. M. de Nijs, A. Kruseman, and M. R. IJpma. VEPFIT applied to depth profiling problems. *Applied Surface Science*, 85:216–224, January 1995.

[139] A. van Veen, H. Schut, J. de Vries, R. A. Hakvoort, and M. R. Ijpma. Analysis of positron profiling data by means of "VEPFIT". In *AIP Conference Proceedings*, volume 218, pages 171–198, Ontario (Canada), February 1991. AIP.

[140] G. C. Aers. Positron stopping profiles in multilayered systems. *Journal of Applied Physics*, 76(3):1622–1632, August 1994.

[141] R. Krause-Rehberg, N. van der Walt, L. Büttner, and F. Börner. A ^{22}Na positron source for use in UHV. *Nuclear Instruments and Methods in Physics Research Section B: Beam Interactions with Materials and Atoms*, 221:165–167, July 2004.

[142] Antti Pelli. *Implementation and Testing of High Voltage System for Pulsed Low-Energy Positron Beam and Conventional Positron Beam Studies in InN*. PhD thesis, Department of Engineering Physics, Helsinki University of Technology, Finland, 2007.

[143] A. Laakso, A. Pelli, K. Rytsölä, K. Saarinen, and P. Hautojärvi. Determination of the timing properties of a pulsed positron lifetime beam by the application of an electron gun and a fast microchannel plate. *Applied Surface Science*, 252(9):3148–3153, February 2006.

[144] A. Pelli, A. Laakso, K. Rytsölä, and K. Saarinen. The design of the main accelerator for a pulsed positron beam. *Applied Surface Science*, 252(9):3143–3147, February 2006.

[145] Antti Pelli, Antti Laakso, Klaus Rytsölä, Reino Aavikko, Mikko Rummukainen, and Kimmo Saarinen. HV design of a pulsed lifetime beam with a grounded sample. *Materials Science Forum*, 445–446:504–506, 2004.

[146] Reino Aavikko. Pulssitetun positronisuihkun suunnittelu, testaus ja dokumentointi OSA 2. Special assignment, Helsinki University of Technology, Finland, November 2001.

[147] Filip Tuomisto. Pulssitetun positronisuihkun rakenteiden suunnittelu, testaus ja dokumentointi – osa I. Special assignment, Helsinki University of Technology, Finland, October 2000.

[148] Esa Korhonen. Control software for a pulsed positron beam. Special assignment, Helsinki University of Technology, Finland, October 2008.

[149] Olli-Pekka Hiironen. Energiavalitsimen suunnittelu pulssitettuun positronisuihkuun (Planning of a energy selector to the pulsed positron beam). Special assignment, Helsinki University of Technology, Finland, March 1996.

[150] Matti Aksela. Pulssitetun positronisuihkun lähdealueen magneettikenttien linjaus sekä esikimputtimen testaus. Special assignment, Helsinki University of Technology, Finland, July 1998.

[151] F. J. Lynch, R. N. Lewis, L. M. Bollinger, W. Henning, and O. D. Despe. Beam buncher for heavy ions. *Nuclear Instruments and Methods*, 159(2–3):245–263, February 1979.

[152] U. Ratzinger, R. Geier, W. Schollmeier, S. Gustavsson, and E. Nolte. The three-harmonics double-drift buncher at the munich heavy ion postaccelerator. *Nuclear Instruments and Methods in Physics Research*, 205(3):381–386, February 1983.

[153] D. Schödlbauer, K. Rudolph, U. Lenz, and S. J. Skorka. A simple subnanosecond high energy buncher for the Munich MP-tandem. *Nuclear Instruments and Methods in Physics Research Section A: Accelerators, Spectrometers, Detectors and Associated Equipment*, 244(1–2):180–182, February 1986.

[154] R. Zierl, W. Czech, P. Kienle, H. J. Körner, K. E. Rehm, P. Sperr, and W. Wagner. A picosecond bunching system at the Munich MP-tandem accelerator. *Nuclear Instruments and Methods*, 164(2):219–224, August 1979.

[155] S. A. Wender, C. E. Floyd, T. B. Clegg, and W. R. Wylie. A high efficiency bunching system for polarized beams. *Nuclear Instruments and Methods*, 174(3):341–347, August 1980.

[156] P. Willutzki, P. Sperr, D. T. Britton, G. Kögel, R. Steindl, and W. Triftshäuser. A new concept for a pulsed positron source. *Materials Science Forum*, 105–110:2009–2016, 1992.

[157] P. Willutzki, J. Störmer, G. Kögel, P. Sperr, D. T. Britton, R. Steindl, and W. Triftshäuser. An improved pulsed low-energy positron system. *Measurement Science and Technology*, 5(5):548–554, 1994.

[158] Sami Kivistö. Pulssitetun positronisuihkun ajastuskomponenttien ohjauselektroniikan suunnittelu ja toteutus, osa III. Study report, Department of Applied Physics, Helsinki University of Technology, Finland, June 2008.

[159] Antti Laakso, Mikko Hakala, Antti Pelli, Klaus Rytsölä, Kimmo Saarinen, and Pekka J. Hautojärvi. Scattering effects in a positron lifetime beam line. *Materials Science Forum*, 445–446:489–491, 2004.

[160] C. Goldstein and A. Laisne. Third harmonic simulated buncher. *Nuclear Instruments and Methods*, 61(2):221–225, May 1968.

[161] W. T. Milner. Double-drift beam bunching systems. *IEEE Transactions on Nuclear Science*, 26(1):1445–1449, 1979.

[162] Juha Oila. Kiihdytinrakenteen suunnittelu pulssitettua positronisuihkua varten. Special assignment, Helsinki University of Technology, Finland, March 1997.

[163] Panu Kantola. Pulssitetun positronisuihkun radiotaajuusohjauselektroniikan testaaminen ja kehittäminen. Special assignment, Helsinki University of Technology, Finland, November 2004.

[164] Sami Kivistö. Pulssitetun positronisuihkun ajastuskomponenttien ohjauselektroniikan suunnittelu ja toteutus, osa II (Control electronics for the timing system of the pulsed positron beam, part II). Special assignment, Helsinki University of Technology, Finland, April 2007.

[165] Antti Pelli. Pulssitetun positronisuihkun ajastuskomponenttien ohjauselektroniikan suunnittelu ja toteutus. Special assignment, Helsinki University of Technology, Finland, August 2001.

[166] Glenn F. Knoll. *Radiation Detection and Measurement*. John Wiley & Sons, 3 edition, 2000.

[167] Olli-Pekka Hiironen. Bariumfluoridi-tuikekiteiden toiminnan tutkiminen positronin elinaikalaitteistossa (Testing of barium fluoride scintillators). Special assignment, Helsinki University of Technology, Finland, February 1997.

[168] Pekka Pursula. Bariumfluoridi-tuikeilmaisimen aikaresoluution ja efektiivisyyden tutkimus (Investigation of the time resolution and efficiency of barium fluoride scintillation detector). Special assignment, Helsinki University of Technology, Finland, January 2001.

[169] P. Sperr. Timing measurements with barium flouride scintillators. *Nuclear Instruments and Methods in Physics Research Section A: Accelerators, Spectrometers, Detectors and Associated Equipment*, 254(3):635–636, March 1987.

[170] Pasi Valminen. BaF_2-tuikekide positronin elinaikalaitteistossa. Special assignment, Helsinki University of Technology, Finland, June 2003.

[171] Philips Components. *Philips PC04 Photomultipliers Data Handbook*, 1990.

[172] Floris Reurings. Pulssitetun positronisuihkun säteilyilmaisimen testaus sekä ilmaisimen magneettisuojan suunnittelu (Design and testing of pulsed positron

beam detector and magnetic shielding). Special assignment, Helsinki University of Technology, Finland, May 2004.

[173] Floris Reurings. Unpublished, 2005.

[174] Mikko Rummukainen. Näytteenpitimen suunnittelu pulssitettuun positronisuihkuun (Design of sample holders and manipulators for pulsed positron lifetime beam). Special assignment, Helsinki University of Technology, Finland, 2002.

[175] D. Bochert. Optimierte Analyse von Lebenszeitspektren aus Positronenstrahlsystemen. Master's thesis, Institut für Angewandte Physik und Messtechnik, Universität der Bundeswehr München, Germany, 2004.

[176] Werner Egger. Private communication, June 2009.

[177] Bent Nielsen, K. G. Lynn, A. Vehanen, and Peter J. Schultz. Positron diffusion in Si. *Physical Review B*, 32(4):2296–2301, August 1985.

[178] R. S. Brusa, M. Duarte Naia, E. Galvanetto, P. Scardi, and A. Zecca. Tungsten singlecrystal and polycrystalline foils used as first transmission moderator. *Materials Science Forum*, 105–110:1849–1852, 1992.

[179] H. P. Maruska and J. J. Tietjen. The preparation and properties of vapor-deposited single-crystal-line GaN. *Applied Physics Letters*, 15(10):327–329, November 1969.

[180] W. M. Yim, E. J. Stofko, P. J. Zanzucchi, J. I. Pankove, M. Ettenberg, and S. L. Gilbert. Epitaxially grown AlN and its optical band gap. *Journal of Applied Physics*, 44(1):292–296, January 1973.

[181] Chad S. Gallinat, Gregor Koblmuller, Jay S. Brown, Sarah Bernardis, James S. Speck, Grace D. Chern, Eric D. Readinger, Hongen Shen, and Michael Wraback. In-polar InN grown by plasma-assisted molecular beam epitaxy. *Applied Physics Letters*, 89(3):032109–3, July 2006.

[182] G. Koblmuller, C. S. Gallinat, S. Bernardis, J. S. Speck, G. D. Chern, E. D. Readinger, H. Shen, and M. Wraback. Optimization of the surface and structural quality of N-face InN grown by molecular beam epitaxy. *Applied Physics Letters*, 89(7):071902–3, August 2006.

[183] Hai Lu, William J. Schaff, Jeonghyun Hwang, Hong Wu, Wesley Yeo, Amit Pharkya, and Lester F. Eastman. Improvement on epitaxial grown of InN by migration enhanced epitaxy. *Applied Physics Letters*, 77(16):2548–2550, October 2000.

[184] Yoshiki Saito, Nobuaki Teraguchi, Akira Suzuki, Tsutomu Araki, and Yasushi Nanishi. Growth of high-electron-mobility InN by RF molecular beam epitaxy. *Japanese Journal of Applied Physics*, 40(2A):L91–L93, 2001.

[185] K. M. Yu, Z. Liliental-Weber, W. Walukiewicz, W. Shan, J. W. Ager, III, S. X. Li, R. E. Jones, E. E. Haller, Hai Lu, and William J. Schaff. On the crystalline structure, stoichiometry and band gap of InN thin films. *Applied Physics Letters*, 86(7):071910–3, February 2005.

[186] O. Briot, B. Maleyre, and S. Ruffenach. Indium nitride quantum dots grown by metalorganic vapor phase epitaxy. *Applied Physics Letters*, 83(14):2919–2921, October 2003.

[187] Bénédicte Maleyre, Olivier Briot, and Sandra Ruffenach. MOVPE growth of InN films and quantum dots. *Journal of Crystal Growth*, 269(1):15–21, August 2004.

[188] S. Suihkonen, J. Sormunen, V. T. Rangel-Kuoppa, H. Koskenvaara, and M. Sopanen. Growth of InN by vertical flow MOVPE. *Journal of Crystal Growth*, 291(1):8–11, May 2006.

[189] C. J. Lu, L. A. Bendersky, Hai Lu, and William J. Schaff. Threading dislocations in epitaxial InN thin films grown on (0001) sapphire with a GaN buffer layer. *Applied Physics Letters*, 83(14):2817–2819, October 2003.

[190] R. S. Qhalid Fareed, R. Jain, R. Gaska, M. S. Shur, J. Wu, W. Walukiewicz, and M. Asif Khan. High quality InN/GaN heterostructures grown by migration enhanced metalorganic chemical vapor deposition. *Applied Physics Letters*, 84(11):1892–1894, March 2004.

[191] C. S. Gallinat, G. Koblmuller, Feng Wu, and J. S. Speck. Evaluation of threading dislocation densities in In- and N-face InN. *Journal of Applied Physics*, 107(5):053517–7, March 2010.

[192] V. Lebedev, V. Cimalla, J. Pezoldt, M. Himmerlich, S. Krischok, J. A. Schaefer, O. Ambacher, F. M. Morales, J. G. Lozano, and D. Gonzalez. Effect of dislocations on electrical and electron transport properties of InN thin films. I. Strain relief and formation of a dislocation network. *Journal of Applied Physics*, 100(9):094902–13, November 2006.

[193] J. Oila, A. Kemppinen, A. Laakso, K. Saarinen, W. Egger, L. Liszkay, P. Sperr, H. Lu, and W. J. Schaff. Influence of layer thickness on the formation of In vacancies in InN grown by molecular beam epitaxy. *Applied Physics Letters*, 84(9):1486–1488, March 2004.

[194] A. Pelli, K. Saarinen, F. Tuomisto, S. Ruffenach, and O. Briot. Influence of V/III molar ratio on the formation of In vacancies in InN grown by metal-organic vapor-phase epitaxy. *Applied Physics Letters*, 89(1):011911–3, July 2006.

[195] W. Walukiewicz. Intrinsic limitations to the doping of wide-gap semiconductors. *Physica B: Condensed Matter*, 302–303:123–134, 2001.

[196] S. X. Li, K. M. Yu, J. Wu, R. E. Jones, W. Walukiewicz, J. W. Ager, W. Shan, E. E. Haller, Hai Lu, and William J. Schaff. Fermi-level stabilization energy in group III nitrides. *Physical Review B*, 71(16):161201–4, April 2005.

[197] K. S. A. Butcher, A. J. Fernandes, P. P.-T. Chen, M. Wintrebert-Fouquet, H. Timmers, S. K. Shrestha, H. Hirshy, R. M. Perks, and Brian F. Usher. The nature of nitrogen related point defects in common forms of InN. *Journal of Applied Physics*, 101(12):123702–11, June 2007.

[198] K. S. A. Butcher, M. Wintrebert-Fouquet, P. P.-T. Chen, T. L. Tansley, H. Dou, S. K. Shrestha, H. Timmers, M. Kuball, K. E. Prince, and J. E. Bradby. Nitrogen-rich indium nitride. *Journal of Applied Physics*, 95(11):6124–6128, June 2004.

[199] J. C. Ho, P. Specht, Q. Yang, X. Xu, D. Hao, and E. R. Weber. Effects of stoichiometry on electrical, optical, and structural properties of indium nitride. *Journal of Applied Physics*, 98(9):093712–5, November 2005.

[200] A. Laakso, J. Oila, A. Kemppinen, K. Saarinen, W. Egger, L. Liszkay, P. Sperr, H. Lu, and W. J. Schaff. Vacancy defects in epitaxial InN: identification and electrical properties. *Journal of Crystal Growth*, 269(1):41–49, August 2004.

[201] E. A. Davis, S. F. J. Cox, R. L. Lichti, and C. G. Van de Walle. Shallow donor state of hydrogen in indium nitride. *Applied Physics Letters*, 82(4):592–594, January 2003.

[202] X. M. Duan and C. Stampfl. Defect complexes and cluster doping of InN: First-principles investigations. *Physical Review B*, 79(3):035207–16, January 2009.

[203] Anderson Janotti and Chris G. Van de Walle. Sources of unintentional conductivity in InN. *Applied Physics Letters*, 92(3):032104–3, January 2008.

[204] S. Limpijumnong and C. G. Van de Walle. Passivation and doping due to hydrogen in III-nitrides. *physica status solidi (b)*, 228(1):303–307, 2001.

[205] D. C. Look, H. Lu, W. J. Schaff, J. Jasinski, and Z. Liliental-Weber. Donor and acceptor concentrations in degenerate InN. *Applied Physics Letters*, 80(2):258–260, January 2002.

[206] C. Stampfl, C. G. Van de Walle, D. Vogel, P. Krüger, and J. Pollmann. Native defects and impurities in InN: First-principles studies using the local-density approximation and self-interaction and relaxation-corrected pseudopotentials. *Physical Review B*, 61(12):R7846–R7849, March 2000.

[207] Chad S. Gallinat, Gregor Koblmuller, and James S. Speck. The role of threading dislocations and unintentionally incorporated impurities on the bulk electron conductivity of In-face InN. *Applied Physics Letters*, 95(2):022103–3, July 2009.

[208] V. Lebedev, V. Cimalla, T. Baumann, O. Ambacher, F. M. Morales, J. G. Lozano, and D. Gonzalez. Effect of dislocations on electrical and electron transport properties of InN thin films. II. Density and mobility of the carriers. *Journal of Applied Physics*, 100(9):094903–8, November 2006.

[209] L. F. J. Piper, T. D. Veal, C. F. McConville, Hai Lu, and W. J. Schaff. Origin of the *n*-type conductivity of InN: The role of positively charged dislocations. *Applied Physics Letters*, 88(25):252109–3, June 2006.

[210] J. S. Thakur, R. Naik, V. M. Naik, D. Haddad, G. W. Auner, H. Lu, and W. J. Schaff. Temperature dependence of mobility and carrier density in InN films. *Journal of Applied Physics*, 99(2):023504–5, January 2006.

[211] Kejia (Albert) Wang, Yu Cao, John Simon, Jing Zhang, Alexander Mintairov, James Merz, Douglas Hall, Thomas Kosel, and Debdeep Jena. Effect of dislocation scattering on the transport properties of InN grown on GaN substrates by molecular beam epitaxy. *Applied Physics Letters*, 89(16):162110–3, October 2006.

[212] Xinqiang Wang, Song-Bek Che, Yoshihiro Ishitani, and Akihiko Yoshikawa. Threading dislocations in In-polar InN films and their effects on surface morphology and electrical properties. *Applied Physics Letters*, 90(15):151901–3, April 2007.

[213] R. E. Jones, S. X. Li, L. Hsu, K. M. Yu, W. Walukiewicz, Z. Liliental-Weber, J. W. Ager III, E. E. Haller, H. Lu, and W. J. Schaff. Native-defect-controlled n-type conductivity in InN. *Physica B: Condensed Matter*, 376–377:436–439, April 2006.

[214] S. X. Li, R. E. Jones, E. E. Haller, K. M. Yu, W. Walukiewicz, J. W. Ager, III, Z. Liliental-Weber, Hai Lu, and William J. Schaff. Photoluminescence of energetic particle-irradiated $In_xGa_{1-x}N$ alloys. *Applied Physics Letters*, 88(15):151101–3, April 2006.

[215] R. E. Jones, S. X. Li, E. E. Haller, H. C. M. van Genuchten, K. M. Yu, J. W. Ager, III, Z. Liliental-Weber, W. Walukiewicz, H. Lu, and W. J. Schaff. High electron mobility InN. *Applied Physics Letters*, 90(16):162103–3, April 2007.

[216] F. Tuomisto, A. Pelli, K. M. Yu, W. Walukiewicz, and W. J. Schaff. Compensating point defects in $^{4}He^{+}$-irradiated InN. *Physical Review B*, 75(19):193201–4, May 2007.

[217] M. Rummukainen, J. Oila, A. Laakso, K. Saarinen, A. J. Ptak, and T. H. Myers. Vacancy defects in O-doped GaN grown by molecular-beam epitaxy: The role of growth polarity and stoichiometry. *Applied Physics Letters*, 84(24):4887–4889, June 2004.

[218] K. Saarinen, P. Seppala, J. Oila, P. Hautojarvi, C. Corbel, O. Briot, and R. L. Aulombard. Gallium vacancies and the growth stoichiometry of GaN studied by positron annihilation spectroscopy. *Applied Physics Letters*, 73(22):3253–3255, November 1998.

[219] T. Mattila and R. M. Nieminen. Point-defect complexes and broadband luminescence in GaN and AlN. *Physical Review B*, 55(15):9571–9576, April 1997.

[220] F. Tuomisto, K. Saarinen, B. Lucznik, I. Grzegory, H. Teisseyre, T. Suski, S. Porowski, P. R. Hageman, and J. Likonen. Effect of growth polarity on vacancy defect and impurity incorporation in dislocation-free GaN. *Applied Physics Letters*, 86(3):031915–3, January 2005.

[221] F. Tuomisto, K. Saarinen, T. Paskova, B. Monemar, M. Bockowski, and T. Suski. Thermal stability of in-grown vacancy defects in GaN grown by hydride vapor phase epitaxy. *Journal of Applied Physics*, 99(6):066105–3, March 2006.

[222] C. Rauch, F. Reurings, F. Tuomisto, T. D. Veal, C. F. McConville, H. Lu, W. J. Schaff, C. S. Gallinat, G. Koblmüller, J. S. Speck, W. Egger, B. Löwe, L. Ravelli, and S. Sojak. In-vacancies in Si-doped InN. *physica status solidi (a)*, 207(5):1083–1086, 2010.

[223] F. Tuomisto, V. Ranki, D. C. Look, and G. C. Farlow. Introduction and recovery of Ga and N sublattice defects in electron-irradiated GaN. *Physical Review B*, 76(16):165207–10, October 2007.

[224] C. Rauch et al. Unpublished.

[225] Z. Liliental-Weber, R. E. Jones, H. C. M. van Genuchten, K. M. Yu, W. Walukiewicz, J. W. Ager III, E. E. Haller, H. Lu, and W. J. Schaff. TEM

studies of as-grown, irradiated and annealed InN films. *Physica B: Condensed Matter*, 401–402:646–649, December 2007.

[226] Floris Reurings, Filip Tuomisto, Chad S. Gallinat, Gregor Koblmüller, and James S. Speck. Vacancy defects probed with positron annihilation spectroscopy in In-polar InN grown by plasma-assisted molecular beam epitaxy: Effects of growth conditions. *physica status solidi (c)*, 6(S2):S401–S404, 2009.

ISBN 978-952-60-3438-6
ISBN 978-952-60-3439-3 (PDF)
ISSN 1795-2239
ISSN 1795-4584 (PDF)